

Origin of Fermi-level pinning at GaAs/oxide interfaces through the hybrid functional study of defects

THÈSE N° 6898 (2015)

PRÉSENTÉE LE 17 DÉCEMBRE 2015
À LA FACULTÉ DES SCIENCES DE BASE
CHAIRE DE SIMULATION À L'ÉCHELLE ATOMIQUE
PROGRAMME DOCTORAL EN PHYSIQUE

ÉCOLE POLYTECHNIQUE FÉDÉRALE DE LAUSANNE

POUR L'OBTENTION DU GRADE DE DOCTEUR ÈS SCIENCES

PAR

Davide COLLEONI

acceptée sur proposition du jury:

Prof. V. Savona, président du jury
Prof. A. Pasquarello, directeur de thèse
Prof. J. Neugebauer, rapporteur
Prof. J. Robertson, rapporteur
Prof. O. Yazyev, rapporteur



ÉCOLE POLYTECHNIQUE
FÉDÉRALE DE LAUSANNE

Suisse
2015

Abstract

Gallium arsenide is currently under scrutiny for replacing silicon in microelectronic devices due to its high carrier mobilities. However, the widespread use of this semiconductor is hampered by the intrinsic difficulty of producing high-quality interfaces with oxides. Indeed, proper device operation is generally prevented by a high density of interface defect states which lead to Fermi-level pinning in the band gap. The pinning of the Fermi-level is also found to occur in bulk GaAs and at GaAs surfaces upon submonolayer deposition of oxygen and other metals. Despite intensive efforts which have spanned more than three decades, the defects and the mechanisms underlying this behavior are not fully understood, thereby preventing further progress.

Through the hybrid functional study of defects, we assign the origin of Fermi-level pinning at GaAs/oxide interfaces to the bistability between the As–As dimer and two As dangling bonds, which transform into each other upon charge trapping (As–As dimer/DB). Using electron-counting arguments, we infer that the identified defect occurs in opposite charge states conferring to the defect the amphoteric nature responsible for the Fermi-level pinning. In our study, we consider intrinsic defects in bulk GaAs finding a complex defect which undergoes a charge trapping mechanism similar to that of the As–As dimer/DB defect and which accounts for the observed Fermi-level pinning in radiation-damaged GaAs. Moreover, we consider oxygen defects in GaAs. Among the defects considered, we identify the one responsible for the observed Fermi-level pinning in O-doped GaAs. The computed defect properties such as the defect structure, the defect charge states, the charge transition level, and the optical transition energies show excellent agreement with the extensive experimental characterization available for this defect. These results clearly assign the origin of the measured Fermi-level pinning and optical transitions in O-doped GaAs to this O defect. In addition, we note that this O defect also shows a bistable behavior similar to that of the As–As dimer/DB defect. We find confirmation of the general occurrence of the As–As dimer/DB defect in GaAs by considering the GaAs(110) surface and suboxide model structures representing of the interfacial transition layer. Indeed, we find that both these systems show the formation of this defect, thus connecting the GaAs oxidation process to the defect formation. In particular, for the case of the suboxide models we calculate a charge transition level falling in the midgap region of the GaAs band gap in accord with the measured interfacial density of states. Finally, we address the GaAs/Al₂O₃ interface. We obtain band offsets in excellent agreement with X-ray photoemission experiments and assess that the prevalent chemical bonding at the interface consists of Ga–O bonds. Then, we study structural and electronic properties of a set of defects occurring on the GaAs side of

the interface. We find that the bistable As–As dimer/DB defect can occur either as an isolated defect or within defect complexes. The calculated charge transition level and donor/acceptor character are in agreement with the experimental characterization of the interfacial density of states. This result corroborates the dominant role of the As–As dimer/DB defect in the determination of the Fermi-level pinning at GaAs/oxide interfaces.

Key words: GaAs/oxide interfaces, Fermi-level pinning, Amphoteric defects, Hybrid functional

Sommario

L'alta mobilità dei portatori di carica nell'arseniuro di gallio rendono questo semiconduttore una valida alternativa al silicio nello sviluppo di dispositivi microelettronici. Tuttavia la difficoltà nell'ottenere interfacce di alta qualità tra GaAs e un ossido ne limita la diffusione. Infatti, l'alta densità di stati dovuta a difetti all'interfaccia impedisce il corretto funzionamento del dispositivo, causando il *pinning* del livello di Fermi. Questo fenomeno è osservato anche in *bulk* GaAs e alla sua superficie in seguito alla deposizione di ossigeno o metalli in quantità pari a frazioni di *monolayer*. Nonostante gli intensi sforzi della comunità scientifica negli ultimi trent'anni, il meccanismo e i difetti all'origine di questi fenomeni non sono ancora stati completamente compresi.

In questo lavoro di tesi è stato condotto uno studio di difetti attraverso la teoria del funzionale di densità con approssimazione di funzionali ibridi. L'origine del *pinning* del livello di Fermi all'interfaccia GaAs/ossido è attribuito alla bistabilità del dimero As–As che si trasforma in due *dangling bonds* in seguito alla cattura di due elettroni (As–As dimero/DB). Utilizzando l'*electron-counting rule* è possibile associare stati di carica di segno opposto alle due configurazioni del difetto, conferendogli il carattere anfotero responsabile del *pinning* del livello di Fermi. Inizialmente, si sono considerati dei difetti intrinseci presenti nel *bulk*, tra i quali si è identificato un complesso che mostra proprietà simili a quelle del difetto As–As dimero/DB e che spiega il *pinning* del livello di Fermi osservato in campioni danneggiati da radiazione. È stata presa poi in considerazione l'impurezza di ossigeno nel GaAs. Tra i difetti considerati, è stato identificato quello responsabile del *pinning* del livello di Fermi nel GaAs drogato O. Le proprietà strutturali, lo stato di difetto, le energie delle transizioni ottiche, gli stati di carica calcolati sono tutti in ottimo accordo con la caratterizzazione sperimentale di questo difetto disponibile in letteratura. Da notare come il carattere anfotero di questo difetto sia simile a quello osservato per il difetto As–As dimero/DB. La presenza diffusa del difetto As–As dimero/DB nel GaAs è confermata attraverso lo studio della superficie GaAs(110) e di modelli amorfi di subossido rappresentativi dello stato di transizione presente all'interfaccia tra GaAs e ossido. In entrambi questi sistemi si osserva la formazione spontanea del difetto As–As dimero/DB, riconducibile al processo di ossidazione. In particolare, nel caso dei modelli amorfi di subossido, il livello di difetto calcolato è in accordo con il picco al centro del *band gap* del GaAs, presente nella densità di stati misurata all'interfaccia. Infine, si è presa direttamente in considerazione l'interfaccia GaAs/Al₂O₃. I *band offsets* calcolati sono in ottimo accordo con gli esperimenti di *X-ray photoemission* e mostrano che il legame chimico prevalente all'interfaccia è Ga–O. In seguito sono state considerate le proprietà strutturali ed elettriche dei

difetti del GaAs all'interfaccia. Il difetto As–As dimero/DB può essere presente come difetto isolato o legato ad altri difetti. Il livello di difetto calcolato separa il carattere donore da quello accettore del difetto, in accordo con le evidenze sperimentali. Questi risultati confermano il ruolo dominante che il difetto As–As dimero/DB ricopre nel fenomeno del *pinning* del livello di Fermi all'interfaccia GaAs/ossido.

Parole chiave: Interfaccia GaAs/ossido, *Pinning* del livello di Fermi, Difetti anfoteri, Funzionali ibridi

Contents

Abstract (English/Italiano)	i
1 Introduction	1
1.1 Complementary metal-oxide-semiconductor (CMOS): Si and III-V semiconductors	1
1.2 GaAs: the prototypical material	2
1.3 Fermi-level pinning	9
1.4 Motivation	11
1.5 Outline of the thesis	11
2 Computational Methods and Theoretical Background	15
2.1 Hybrid density functional theory applied to the study of defects	15
2.2 Computational methods and details	17
2.3 Electron counting rule	20
2.4 Defect study	21
2.5 Finite-size corrections	22
3 Intrinsic defects in bulk GaAs	27
4 Oxygen defects in bulk GaAs	39
5 Intermediately oxidized GaAs	61
5.1 Oxygen deposition on the GaAs(110) surface	61
5.2 Ga As suboxide: an interfacial transition layer	63

Contents

6 GaAs/oxide interface	71
6.1 Band alignment and chemical bonding at the GaAs/Al ₂ O ₃ interface	71
6.2 Defects at the GaAs/Al ₂ O ₃ interface	77
6.2.1 Bulk-like defects	83
6.2.2 Interfacial defects	88
6.3 The role of In	97
7 Conclusion	101
Bibliography	119
List of Acronyms	121
Acknowledgements	123
Curriculum Vitae	125

1 Introduction

In this Chapter we introduce the main experimental observations on the occurrence of defects in GaAs. In Section 1.1, we trace an historical presentation of the semiconductor industry with particular care to the motivations underling the study of III-V semiconductors. In Section 1.2, we focus on GaAs. We consider the most studied defects which affect the bulk electronic properties, its surfaces and the early stages of oxygen and metal deposition, and its interfaces with oxides including its structural and electrical properties. In Section 1.3, we discuss the Fermi-level pinning phenomenon as it can occur in the bulk and at interfaces. Finally, we present the outline of the present thesis work in Section 1.5. Parts of this Chapter can be found in peer-reviewed articles [1, 2, 3].

1.1 Complementary metal-oxide-semiconductor (CMOS): Si and III-V semiconductors

The Semiconductor Industry Association, representing the United States leadership in semiconductor manufacturing and design, recently announced the new global semiconductor industry record sales amounting to \$335.8 billion for the year 2014 [4]. The size of the semiconductor industry market can be better understood if compared with that, for example, of the worldwide automobile production which, in 2014, amounted to \$79.3 million [5]. Almost the totality of the semiconductor technology production relies on silicon metal-oxide-semiconductor field-effect-transistor (MOSFET), leaving no space to non-silicon MOSFETs. The reasons for the dominant role of Si over other semiconductors do not originate from its electronic and photonic behaviors, which are, for instance, inferior to those of GaAs. Silicon is cheap and forms highly controllable interfaces with its natural oxide (SiO_2), which shows advantageous electrical properties for its integration in MOSFET devices.

Between the 1960s and 1970s the silicon based MOSFET technology has gone through an intense development period which has led to its rapid progress. On the contrary, the development of non-silicon transistors through the use of III-V and II-VI semiconductors was essentially unsuccessful. The main obstacle to the realization of a non-silicon MOSFET is the presence of interfacial states with energy that lie at the band edges or within the band gap of the semiconductor. The technological impact of these interfacial states on the device operation can be detrimental. Fermi-level pinning reduces the concentration of carriers limiting or

disabling performances of light emitting diodes, lasers, photo-detectors, bipolar transistors, and solar cells. For the first time in 1986, an unpinned (100) GaAs surface was achieved upon removal of the arsenic component from the native GaAs oxide through a surface cleaning procedure [6]. However, due to the high reactivity of these surfaces it was shown that subsequent exposure to air led to the regeneration of the arsenic component and to the pinning of the Fermi-level. This work did not represent a breakthrough for the non-silicon MOSFET technology but indicated a direction for the successive efforts aimed at the development of this technology.

In the last decades, the microelectronic industry has intensified its efforts in the development of non-silicon MOSFETs. This is due to the approaching of the physical limit of the Si-based technology resulting from the continuous shrinking of the transistor size according to Moore's Law. In particular, the increase in drive currents for faster switching speeds at lower supply voltages is typically at the expense of an exponentially growing leakage current, which leads to a large standby dissipation. III-V semiconductors show lower effective masses than Si leading to higher injection velocities that make them suitable for application as channel materials [7, 8, 9]. However, some of them also show a smaller band gap than that of Si leading to unwanted band-to-band tunneling leakage currents, which may ultimately limit the device scalability. Among the III-V semiconductor compounds, the $\text{In}_x\text{Ga}_{1-x}\text{As}$ family is a promising candidate for future MOSFET transistors as it combines the excellent transport properties of InAs and the large band gap of GaAs [8, 10, 11]. The main advantages of using these materials with respect to silicon are expected to be a reduced leakage current, an 80% enhanced drive current, and a 50% reduction of the working power allowing further device scalability [12].

1.2 GaAs: the prototypical material

The prototypical III-V material is GaAs [13]. The extensive study of the GaAs reconstructed surfaces, native oxides, and interfaces with technologically relevant oxides has been essential for the understanding of the structural and electrical properties of other III-V semiconductors. Because of its central role in the III-V semiconductor research, we mainly focus in this work on the study of GaAs. The crystal structure of GaAs is zinc blende¹ with a unit cell of 5.65 Å and a Ga–As bond distance of 2.45 Å [14]. It is a direct band gap semiconductor with a 1.53 eV forbidden energy zone [14]. The valence band maximum (VBM) and the conduction band minimum (CBM) fall at the Γ point. Other minima of the conduction band fall at the L and X points leading to indirect band gaps of 1.82 and 1.98 eV [15].

Bulk: SI-GaAs

Following the indication that defects are responsible for the Fermi-level pinning observed at the interface, a preliminary study of the semi-insulating (SI) properties in bulk GaAs can identify the dominant electrical active defects occurring in GaAs.

¹The zinc blende structure is composed of two face-centered cubic (FCC) lattices shifted to each other by half the diagonal of the FCC cube. In GaAs and in all III-V compounds, one FCC sublattice is composed of group III atoms while the other by group V atoms.

The SI behavior arises under particular doping conditions of GaAs which enforce ambipolar conductivity (due to electrons and holes) by pinning the Fermi-level at mid-gap. This material is called semi-insulating gallium arsenide (SI-GaAs) since it shows electrical resistivity (between 10^7 and $10^9 \Omega \text{ cm}$ at room temperature) and carriers concentration ($n_i(300^\circ \text{K}) = 2.25 \cdot 10^6 \text{ cm}^{-3}$) close to that of perfect GaAs crystals [15]. The high electrical resistivity value is responsible for the name given to these GaAs samples. From the technological point of view, this material has been considered relevant due to its interesting electrical properties which made it suitable for application in integrated circuits and optoelectronic devices [16]. The typical growth conditions resulting in SI-GaAs are chromium and oxygen doping and the use of As-rich conditions yielding the formation of the EL2 defect [17, 18, 19].

The effect of Cr incorporation in GaAs is well established [16]. Chromium atoms occupy Ga sites and are found to act as electron donors and electron acceptors depending on the position of the Fermi-energy. The coexistence of negative and positive defect charge states is referred to as amphoteric behavior (vide infra). In particular, the defect levels fall at 0.3 and 0.8 eV above the VBM [16]. When GaAs/oxide interfaces are grown, no Cr impurities are incorporated and their further investigation is therefore unnecessary for the purposes of the present thesis.

Undoped GaAs shows SI behavior when the sample growth is carried out above a critical As concentration (the optimized stoichiometry range is between $0.48 \leq [\text{As}]/([\text{As}]+[\text{Ga}]) \leq 0.53$) [16]. The observed SI behavior has been associated to the occurrence of As defects and in particular, to the so called EL2 defect as it is present in high concentrations [19]. Extensive experimental investigations have focused on the study of the EL2 defect properties [16, 19, 20, 21, 22, 23, 24, 25, 26, 27, 28]. This defect acts as a double donor defect with defect levels falling at 0.54 and 0.75 eV above the VBM [21]. An interesting property of the EL2 defect is that it can be bleached at low temperatures (T below 140 K) by illumination with photon energies in the range from 1.0 to 1.3 eV [23]. This procedure leads the defect to occupy a metastable state which is electrically and optically inactive. The stable configuration is recovered either thermally (through a barrier of 0.3 eV) [23] or optically (through illumination with light of photon energy smaller than the band gap) [24]. Despite the efforts of the GaAs community in study of the EL2 defect, its atomic structure is the subject of a longstanding discussion in which two similar atomistic arrangements have been considered [20, 22, 25]. Through electron spin resonance (ESR), one observes a high concentration of As antisite defects (As_{Ga}), responsible for a characteristic four-line feature [26]. This defect acts as a double donor with defect levels at 0.5 and 0.75 eV above VBM [27] and shows metastability through the breaking of an As–As bond and the formation of an As interstitial and a Ga vacancy complex ($\text{As}_i\text{-V}_{\text{Ga}}$) [29]. Due to the similarity with the EL2 defect, the isolated As antisite is one of the structures proposed for the EL2 defect. Investigation of the As antisite defect through magnetic circular dichroism absorption (MCDA) combined with ESR measurements, reveals the existence of an As_{Ga} defect family [30]. In particular, one observes an asymmetry in the electron-nuclear double-resonance (ENDOR) lines of the As antisite, which compose the EL2 defect. The data distinguish the [111] direction as far as the surrounding of As_{Ga} defects are concerned, leading to a second proposed atomistic structure for the EL2 defect which corresponds to an As antisite with an As interstitial along the [111] direction [30]. Despite the controversy concerning the atomic structure of the EL2 defect, these studies reveal the crucial role of the As antisite defect in the determination of the electronic properties of SI-GaAs, whether it occurs as an isolated defect or bound to other intrinsic defects. For this reason, In

our investigation, we systematically consider the occurrence of the As antisite defect.

A further method to obtain SI-GaAs consists in oxygen doping. Oxygen is the most common unintentional impurity in GaAs and it is also used as a dopant. It can be present in concentrations ranging between $10^{14} - 10^{20} \text{ cm}^{-3}$ depending on the growth technique [31, 32]. The SI behavior is due to Fermi-level pinning at 0.43 eV below the CBM [31, 33, 34]. Local vibrational mode (LVM) absorption technique has been largely used to experimentally identify oxygen defects in GaAs. The absorption peak at 845 cm^{-1} is associated to an interstitial bridging oxygen atom binding a Ga and an As atom (O_b) [35]. This bridge configuration appears to be electrically inactive [36]. The LVM spectra show other three oxygen related absorption bands, located at 730.7 cm^{-1} , 714.9 cm^{-1} and 714.2 cm^{-1} and labeled *A*, *B*, and *B'* [35, 37, 38]. These absorption lines show a triplet fine structure due to the Ga isotopic concentration and have been associated to a Ga–O–Ga structure [35]. Interconversion between these three vibrational bands is obtained through photoexcitation experiments, suggesting that each band corresponds to a different charge state of a common defect [37, 38]. It was inferred that the charge states associated to the *A* and *B* bands are stable, while that associated to the *B'* band is metastable [36, 37, 38]. Later on, magnetic circular dichroism and electron spin resonance experiments showed that the metastable state is paramagnetic and corresponds to the neutral charge state [39, 40]. The other defect states correspond to the +1 and –1 charge states [34]. This defect has been identified to be responsible for the observed Fermi-level pinning [31, 33, 34].

The structural identification of stable oxygen defects strongly relies on density functional calculations. Most of the available calculations are based on semilocal density functionals. Early calculations supported a $\text{V}_{\text{As}}\text{-O}$ defect structure as candidate for the Ga–O–Ga defect [41, 42, 43], proposed in analogy to the VO center in silicon [35]. Later, Taguchi and Kageshima proposed an interstitial configuration in which the O atom binds to two Ga atoms [44]. However, none of these calculations could fully account for the stable charge states identified experimentally. Pesola *et al.* then proposed a defect complex, denoted $(\text{As}_{\text{Ga}})_2\text{-O}_{\text{As}}$ defect, in which the O_{As} defect shows two As_{Ga} antisites in its first neighboring shell [45]. This defect model shows good agreement with experiments as far as the vibrational frequencies and the involved charge states are concerned, but produces a charge transition level at mid-gap [45], which is inconsistent with the Fermi-level pinning position [31]. The case of the oxygen impurity in GaAs is highly relevant to the study of oxide deposition on GaAs. Indeed, the intimate contact of GaAs with oxygen atoms occurring at the interface can lead to the formation of oxygen-related defects. Moreover, as an O-defect is shown to control the electronic behavior of bulk GaAs when present in high concentration, it is interesting to study its occurrence at the interface. However, the atomic structure of the dominant O-defect in GaAs is still unknown, motivating the study of a large set of O-defects occurring in GaAs, as that presented in Chapter 3.

Surface and early stage of deposition

Prior to the formation of the interface with oxides, the creation of the substrate surface can be seen as the formation of a high concentration of defects. Due to the high directionality of semiconductor bonds, their clean surfaces are highly reactive and can either reconstruct

or absorb gaseous impurities in order to minimize their surface energy. In the former case, the bulk atomic arrangement undergoes distortions in order to minimize the number of unsaturated dangling bonds (DBs) through the formation of new superficial bonds. Typically, these new structures correspond to superficial dimers which are aligned forming rows leading to a surface periodic unit larger than the simple projection of the bulk unit cell on the surface plane. In GaAs several reconstructions are observed, extending from the Ga-rich (4×2) to the As-rich (2×4) terminations. Among these surface reconstructions, the As-rich ones are the most relevant for MOSFET applications, in particular the starting surface used in the epitaxial growth on GaAs layers is the $\beta 2(2\times 4)$ reconstruction obtained under "medium" temperature and As-flux conditions [13]. Thanks to reflection high energy electron diffraction (RHEED), low energy electron diffraction (LEED), and scanning tunneling microscopy (STM), it is widely accepted that the $2\times$ periodicity is due to the dimerization of surface As atoms while the $4\times$ periodicity results from surface vacancies [46, 47, 48, 49]. Concerning the realization of GaAs MOSFETs, it is very important to preserve the clean nature of the GaAs surface, preventing absorption of atmospheric gases on the surface which are indeed responsible for the formation of thick native oxides (vide infra). To this end, GaAs surfaces are typically protected through the deposition of an As capping layer which can be removed at a later stage by heating the substrate to $T > 400^\circ\text{C}$ under vacuum conditions. Upon this thermal procedure the ideal (2×4) reconstructed surface is restored [50]. It is worth to note that this surface-protection method implies the presence of excess As on the surface which can then be associated to the As-rich condition.

Concerning the effect of absorbed impurities on the electrical behavior of GaAs surfaces, the early stages of oxygen and metal deposition have been largely studied by Spicer and coworkers [51, 52, 53, 54, 55, 56, 57]. Firstly, the GaAs(110) surface has been considered [51]. This surface exposes Ga and As atoms and reconstructs through an outward relaxation of the surface As atoms and an inwards relaxation of the surface Ga atoms [51, 58]. This reconstruction pattern is associated with the rehybridization of the surface atoms that lead to the exposure of doubly occupied As DBs and empty Ga DBs [51, 58]. These superficial states are suggested to lie in the valence and in the conduction band of GaAs, respectively leading to the absence of surface states in the band gap [59, 60]. A fraction ($\sim 3\%$) of monolayer of oxygen or different metals is then deposited on the surface of undoped SI GaAs, n -type GaAs, or p -type GaAs. The evolution of the superficial Fermi energy is measured through photoemission in ultra high vacuum [53]. During the deposition, the Fermi energy shifts within the band gap until it is pinned, already at sub-monolayer coverages [52]. The energies at which the Fermi-level pinning occurs is not affected by the nature of the deposited species, suggesting that an intrinsic mechanism is operative. Indeed, the fitted evolution of the Fermi level as a function of coverage always yields the same parameters leading to the conclusion that deposition on the GaAs (110) surface leads to the creation of one type of defect [61]. However, the energies at which the Fermi level is pinned depend on the position of the Fermi energy prior to the deposition [52, 54]. When n -type and SI GaAs samples are considered the surface treatments lead to Fermi-level pinning at 0.75 eV above VBM, while the Fermi-level is pinned at 0.5 eV above VBM when p -type GaAs compounds are used [51, 52, 53, 54]. Through the "unified defect model", it was initially proposed that Ga and As antisite defects, induced by the deposition, underly these experimental observations and, in particular, that the As antisite would be responsible for the pinning at 0.75 eV above VBM, while the Ga antisite would induce the pinning at 0.5

eV above VBM [52, 54, 55]. Subsequently, a similarity between the As antisite defect levels and the energies at which the Fermi-level is pinned upon these superficial treatments was observed, and a second version of the defect model was proposed [56]. Following this rational, the As antisite defect is responsible for the observed Fermi-level pinning at the surface, but because of its double donor character the existence of a charge compensating spectator defect of unknown origin has to be assumed [56, 57]. However, whereas As enrichment at the surface is observed during the oxygen deposition and the high concentration of As antisite defects in GaAs is widely accepted [31, 32], no definite evidence for the existence of any spectator defects has been found. Lately, the same Fermi-level pinning behavior has also been reported for other GaAs(100) reconstructed surfaces, including the (4×6), (2×8), and (4×4) reconstructions, in which the superficial As content is progressively increased [56]. The absence of a reliable model for the understanding of these surface observations leaves space for further investigations. The early deposition of oxygen on the GaAs surfaces represent the early stage of the oxide deposition on the GaAs substrate and is thus highly relevant to the study of GaAs/oxide interfaces.

GaAs/oxide interfaces

The efforts of the III-V community to synthesize defect-free GaAs/oxide interfaces can be divided into two directions: the oxide deposition and the handling of the native oxide. Concerning the oxide deposition, many different techniques and a variety of oxides have been investigated [13], including pyrolytic deposition of silicon dioxide, silicon nitride, aluminum oxide, molecular beam epitaxy (MBE) of gallium oxide, and gadolinium oxide, and atomic layer deposition (ALD) of aluminum oxide, silicon oxide, hafnium oxide. These are only a few examples of the investigated methods [13].

The main deposition techniques are MBE and ALD. The MBE process is a refinement of the vacuum evaporation process in which neutral thermal atomic or molecular beams are deposited on a heated substrate under ultra-high vacuum conditions (pressure below 10^{-7} Pa). The MBE technique is primarily developed for the growth of III-V compounds as it ensures low concentration of contaminants and the achievement of very high quality electrical and optical properties. This growth quality is achieved through a very slow deposition rate (typically less than 3000 nm per hour) which allows an epitaxial growth. The substrate temperature is usually between 500-750°C and the growth is controlled by the group III element, as its flux is typically 3-5 times smaller than that of group V element. Source materials are usually elemental and for the case of GaAs, are solid Ga and tetraatomic As₄ molecules [62]. The deposition of the oxide is then usually achieved in the same chamber where the III-V substrate has been grown. In 1995, at Bells Labs, the deposition of a Ga₂O₃(Gd₂O₃) dielectric from a Ga₅Gd₃O₁₅ precursor on a GaAs substrate was shown to produce very low midgap density of interfacial defects (below 10^{10} eV⁻¹ cm⁻²) [63, 64, 65, 66]. It was proposed that the achievement of unpinned interfaces is due to the particular mechanism for the chemisorption of the deposited Ga₂O molecules, which restore the charge of superficial Ga and As atoms to their near-bulk value upon breaking the As dimer pairs [67].

The ALD is an ex-situ, robust, and manufacturable process that attracts the interest of industry

Table 1.1 – Stable GaAs native oxides and their Gibbs free energy (ΔG), taken from Ref. [69, 71].

oxide	ΔG (kcal/mol)
Ga ₂ O	–75.3
Ga ₂ O ₃	–238.6
GaAsO ₄	–212.8
As ₂ O ₃	–137.7
As ₂ O ₅	–187.0

since it allows fast growth rates and does not require advanced vacuum systems. Due to its ex-situ nature and due to the high reactivity of GaAs surfaces in air, the ALD process has to deal with a few layers of native oxides which cover the substrate surface. This deposition process consists of sequential alternating pulses of gaseous chemical precursors that react with the substrate. During each pulse, a precursor is pulsed into a chamber under vacuum condition (pressure below 133 Pa) for a given amount of time, during which the precursor reacts with the substrate through a self-limiting process leaving no more than one monolayer. Then, the chamber is purged with inert gas (N₂ or Ar) and subsequently the second precursor is pulsed in the chamber. Typically, the ALD process is conducted at a temperature around 300°C [68].

Motivated by the great success of thermally oxidized SiO₂ on Si, the study of the native oxide on GaAs as high- κ material has been considered and intensively studied [69, 70]. The main problem about the use of the GaAs native oxide as insulating layer is its low stability, showing low dielectric breakdown strength. Moreover, the resulting interface shows a high density of interfacial states, which pin the Fermi energy and are associated to a significant presence of As oxides and elemental As [13]. The composition of the GaAs native oxide is complicated by the co-existence of various oxidation states of As and Ga, which correspond to the formation of As₂O₃, As₂O₅, Ga₂O₃, and Ga₂O. The relative stability of these oxides is assessed through their bulk thermodynamic Gibbs free energies, given in Table 1.1.

The As-oxides are the less stable ones and are in fact easily removed or converted into Ga-oxides through annealing or post-etching procedures [72, 73, 74, 75, 76, 77]. The ALD deposition of a typical oxide such as Al₂O₃ has interesting effects on the GaAs native oxide [77]. In particular, as shown by medium energy ion scattering spectroscopy and X-ray photoelectron spectroscopy, the deposition of trimethylaluminum (TMA) is able to achieve a 65% reduction of the native oxide. This process is referred to as "self-cleaning". As proposed in Ref. [74], the resulting thin interfacial transition layer is a suboxide with an approximate composition of Ga₂As_{0.3}O₂. A detailed description of the structural and the electronic properties of this suboxide interfacial transition layer is lacking. More importantly, it is unclear whether this layer could contain electrically active defects responsible for the observed Fermi-level pinning. Computer simulation methods can contribute to the understanding of the impact of this transition layer on the electrical properties of the interface. Indeed, the generation of amorphous suboxide models for the study of the Ge/GeO₂ interface already demonstrated the usefulness of computational methods [78].

Among the oxides considered to be deposited through ALD on top of GaAs, Al_2O_3 is the industrially preferred one, as it shows a wide band gap, a high breakdown field, a high thermal stability, and it remains amorphous under typical device processing conditions [13]. Amorphous Al_2O_3 ($a\text{-Al}_2\text{O}_3$) exists with a density ranging between 3.05-3.65 g/cm³ showing a variety of local structures including AlO_4 , AlO_5 , and AlO_6 building blocks [79, 80, 81, 82]. The electronic band gap falls between 5.6 and 7.1 eV, depending on the experimental growth technique [83, 84, 85, 86, 87, 88, 89, 90]. An important feature characterizing the interface between GaAs and amorphous Al_2O_3 , here denoted as GaAs/ Al_2O_3 interface, is the band alignment. However there is some incertitude in the experimental value of the valence band offset at the GaAs/ Al_2O_3 interfaces. We can here also consider experimental valence band offset pertaining to InGaAs, as the valence bands of GaAs and InGaAs have experimentally been found to be aligned within 0.1 eV [88]. X-ray photoemission spectroscopy (XPS) leads to values around 3.8 eV for InGaAs/ Al_2O_3 interfaces [86, 89, 90], while internal photoemission data obtained for GaAs/ Al_2O_3 interfaces give a value around 2.7 eV [87, 88]. So far, theoretical approaches have not been able to dissipate this incertitude supporting either one or the other measured value [91, 92].

Moreover, the interest in Al_2O_3 is due to the realization of GaAs/ Al_2O_3 interfaces with a low density of interfacial traps, when particular GaAs surfaces (Ga-rich) and the self-cleaning process are combined [93]. However, GaAs/ Al_2O_3 interfaces have generally been shown to be rich of defect states, which prevent the proper operation of the device [77, 94, 95, 96, 97, 98, 99, 100, 101, 102]. The density of defects states at the interface (D_{it}) is experimentally measured through capacitance voltage experiments [103]. The typical D_{it} profile shows minor peaks in the vicinity of both the valence and the conduction band. These peaks have been shown to be responsive to sulfur passivation as obtained through the use of the $(\text{NH}_4)_2\text{S}$ precursor [103, 104, 105]. However, the major peak (corresponding to a density of $25 \cdot 10^{12} \text{ eV}^{-1} \text{ cm}^{-2}$) located at midgap (~ 0.7 eV above the valence band maximum) has eluded passivation and has thus been identified as the major obstacle for using GaAs in CMOS devices [100, 103, 104]. Density-of-states measurements indicate that the mid-gap peak separates donor-like from acceptor-like defect states [76]. Experimental observations, such as the reduction of the midgap peak when using Ga-rich surfaces prior to oxidation [104], suggest that the defect responsible for this peak is related to arsenic. In addition, XPS experiments reveal the presence of As-As linkages at the interface [96] and ESR measurements suggest the occurrence of As antisite defects [106].

Significant insight into the origin of specific defect states has recently been acquired through the use of density functional calculations [107, 108, 109, 110, 111, 112, 113, 114, 115, 116]. The small peaks in the density of defect states close to the valence and conduction band edges have thus been assigned to As and Ga DBs, respectively, through model bulk calculations [109, 115]. The antibonding state of the As-As dimer has also been proposed to give defect states close to the conduction-band minimum [111, 113, 115, 116]. As far as the mid-gap peak is concerned, there are bulk GaAs calculations which point to the As antisite defect [106, 117, 118], but a detailed identification based on precise peaks in the measured D_{it} is still lacking. In particular, a systematic study of the formation energies and charge transition levels of defects at the interface is missing, although such a study is expected to give insight into the defects that dominate at the interface. Indeed, the presence of a less rigid structure such as at the interface and the presence of the interface dipole could affect the stability of defect states, which may

differ from their bulk counterparts.

Considering the industrially preferred $\text{In}_{0.53}\text{Ga}_{0.47}\text{As}$ compound (here denoted InGaAs), its interfaces with typical oxides are also rich of defects. The InGaAs/oxide D_{it} shows its major peak in the vicinity of the valence band and a second smaller feature at mid-gap, responsive to passivation treatments [76, 119, 120]. However, a significant contribution to the defect density appearing at ~ 0.3 eV above the conduction band edge [76, 119] represents a major obstacle for proper device operation leading to Fermi-level pinning in the proximity of the conduction band [121]. The measured D_{it} is independent of the nature of the deposited oxide, suggesting that the defects underlying the poor quality of the interfaces relate to the semiconductor substrate [119, 122]. In this case, density functional calculations showed that isolated As dangling bonds give defect states close the valence band edge [109], and thus provide an interpretation for the major peak in the density of interface states. Similarly the peak at mid-gap is consistent with the calculated defect level of the As antisite in InGaAs [123]. However, the trap states which are resonant with the conduction band have not yet conclusively been identified, leaving space for further investigations. Possible candidates are In or Ga dangling bonds [109] and the antibonding state of the As–As dimer [113, 124].

1.3 Fermi-level pinning

In semiconductor compounds, the pinning of the electronic chemical potential (Fermi level) is a common phenomenon. It occurs upon a wide class of physical phenomena such as interface formation, incorporation of chemical impurities, and high-energy radiation damage [125]. Here, we briefly describe the Fermi-level pinning phenomenon in the bulk, at surfaces, and at interfaces.

In the bulk, it is possible to move the Fermi-level from VBM to CBM through doping. In general, the occurrence of electrical active defects affects the position of the Fermi level. The occurrence of defects can lead to Fermi-level pinning when the donor behavior of a defect counteracts the acceptor behavior of another defect. In fact, the former defects release electrons and shift the Fermi level higher in the band gap while the latter defects trap electrons and shift the Fermi level lower in the band gap. When the formation energies of a donor and of an acceptor defect are small and comparable, the Fermi level is pinned around the energy which ensures their coexistence [126]. In the case of highly radiation damaged semiconductors, it is shown that the irradiation of III-V semiconductors induces a Fermi-level shift towards an "ultimate" position, characteristic for each material, which is unaffected by further irradiation [127, 128]. This Fermi level position does not depend on the type of radiation which can consist in electron, neutron or γ -ray radiations [127, 128]. Moreover, this Fermi level position is also independent of the type and of the level of doping prior to the irradiation, suggesting that an intrinsic mechanism is operative [127, 128]. It is proposed that the irradiation process produces electrically active intrinsic defects which shift the Fermi level within the band gap and ultimately pin it. In the case of GaAs, this position corresponds to mid-gap, 0.6 eV above the VBM [127, 128]. Semilocal density functional calculations suggested the existence of bistable vacancies consisting, for example, in an acceptor-like Ga vacancy which transforms into a donor-like complex consisting of an As vacancy and an As antisite [129, 130, 131]. The relevance of such amphoteric defects relies on their ability of changing their electrical

character from acceptor-like to donor-like depending on the position of the Fermi energy in the band gap. Thanks to this mechanism, a high concentration of a single type of amphoteric defect can give Fermi-level pinning.

The formation of a clean surface introduces a discontinuity in the external potential that leads to the formation of surface states. From a mathematical point of view, one generally distinguishes between Shockley states and Tamm states, where the former are derived from the nearly free electron approximation and the latter from the application of the tight-binding model. These states can be formed in high concentration and cause Fermi-level pinning. This is the case, for example, at the Si(111) cleaved surface. The half-filled silicon DBs of this surface point directly to the vacuum and are responsible for a state in the Si band gap. Ensuing n -type doping, the Fermi-level is raised close to CBM, close to the bulk impurity level. Electrons flow from the impurity levels to the surface states in order to lower their energy, leading to the formation of a positively charged layer which extends for hundreds of Å into the bulk. The extent of this layer primarily depends on the different density of states per layer parallel to the surface between the bulk dopant ($\sim 10^8 - 10^{12}/\text{cm}^2$) and the surface dangling bonds ($\sim 10^{15}/\text{cm}^2$). This charge flow creates an electrostatic dipole which prevents the motion of other electrons from the bulk to the surface. Thus, the band edges are bent at the surface so that the Fermi level is close to CBM in the bulk region and at midgap close to the surface. The work function is then nearly independent of the position of the bulk Fermi level (the doping level) which is considered to be pinned [132].

The study of Fermi-level pinning at the interface is complicated by the variety of materials and experimental techniques used to grow interfaces. The barrier between a metal and a semiconductor is predicted by the Schottky-Mott rule to be proportional to the difference between the metal-vacuum work function and the semiconductor-vacuum electron affinity [133]. This condition applies when no charge transfer between the metal and the semiconductor occurs and the Fermi level is not pinned. This case is referred to as the Schottky limit. However, most metal-semiconductor interfaces do not follow this rule but show the formation of electronic states within the semiconductor band gap. These states contribute to charge transfer between the two materials and to the formation of an interfacial electrostatic dipole. In this case the Schottky barrier height is found to be independent of the metal work function and the Fermi-level is considered to be pinned. This case is referred to as the Bardeen limit. Concerning the origin of the states which lie in the semiconductor band gap, Bardeen and Heine suggested that they intrinsically originate from the interface. They can be seen as the interfacial analogues of Tamm states or as metal-induced gap states (MIGS) [134, 135]. However, extrinsic states can be formed during the growth of the interface through the formation of defects, such as vacancies and antisite [51, 52]. In the case of interfaces between semiconductors with different band gaps, Tersoff noted the existence of induced states equivalent to MIGS in the material with the larger band gap [136]. Indeed, if the larger band gap 'contains' the small band gap, as it is usually the case for semiconductor-oxide interfaces, the semiconductor induces states in the oxide band gap but not the contrary as there are no states of the oxide that fall within the semiconductor band gap. The presence of these induced states affect the charge transfer at the interface and the associated dipole, but cannot be responsible for Fermi-level pinning within the semiconductor band gap [137]. This leads to the conclusion that the states which pin the Fermi-level in the semiconductor band gap can only arise from defects.

1.4 Motivation

The current interest in realizing clean III-V/oxide interfaces to be used in the microelectronic industry makes the study of defects in GaAs of particular interest. Indeed, a high density of interfacial states underlies the pinning of the Fermi-level in the semiconductor band gap. In particular, the experimental characterization of the interface points to defects as the origin of this density of states. The identification of the responsible defect structures is instrumental for setting up efficient passivation routes and for further progress. Computational studies can give an important contribution in this defect search, but hitherto a satisfactory agreement with the experimental characterization is lacking. Due to the necessity of using demanding computational methods in order to obtain reliable results, preliminary studies on bulk GaAs, aimed at the identification of the dominant defects occurring in GaAs, can reduce the zoology of defects to be taken under consideration. In this respect, we study the effects of radiation-damage and oxygen doping in bulk GaAs, since these two topics still present unraveled defect structures which underlie the overall electrical properties of these materials. The study of defects at the interface includes the early stages of oxygen deposition on GaAs surfaces, the interfacial suboxide transition layer, and the properties of the GaAs/Al₂O₃ interface with particular focus on the occurrence of defects. The Fermi-level pinning occurring at the surface is not completely understood since the pinning models rely on the existence of unknown defects. The defects occurring in the interfacial suboxide transition layer have not been identified and their role in the Fermi-level pinning at the interface is not clear. Finally, the study of the interface allows us to shed light on the valence band offset incertitude coming from the experiments and to study the properties of relevant GaAs defects in the vicinity of the interface.

The preliminary study on O-defects in GaAs indicates that the properties of the (As_{Ga})₂-O_{As} defect agree well with the large experimental characterization available for the dominant O-defect in GaAs. In particular, this defect reveals the relevance of the amphoteric behavior as origin of Fermi-level pinning. An accurate analysis of this defect shows that its amphoteric property relies on the bistability of the As-As dimer which transforms into two As DBs upon capture of two electrons. For this reason, we reconsider the interfacial As-As dimer by analyzing its behavior upon the capture of two electrons. Indeed, the As-As dimer defect shows negative-*U* behavior with the singly negative As-As defect state being un-stable. The stability of the configuration with two As DBs leads to a charge transition level at midgap, in agreement with the electrical characterization of the interface. The validation of this picture is achieved through the study of the interfacial transition layer and of the GaAs surface, which corroborate the relevance of this mechanism. Finally, we note that the present As-As bistability is a common feature in GaAs which occurs in the EL2 defect and in other intrinsic defect complexes.

1.5 Outline of the thesis

This thesis work is organized as follows. In Chapter 2, we present our computational approach, pointing out the advantages of using hybrid rather than semilocal density functional theory in the study of defect properties. We discuss the formulation of defect charge transition levels and defect formation energies, and describe the adopted finite-size correction scheme.

In Chapter 3, we firstly study defect structures and electrical properties of intrinsic defect in GaAs. Isolated antisites, and bistable vacancies of both Ga and As are considered. In order to get better agreement with the Fermi-level pinning observed in radiation-damaged GaAs, we consider an As antisite bound to a Ga vacancy which is shown to possess bistable and amphoteric behavior consistent with the experimental Fermi-level pinning. The actual occurrence of the considered defect complexes is examined against two criteria. The first criterion concerns the stability against dissociation and can be evaluated from the calculated dissociation energies. The second criterion involves the defect formation at thermodynamic equilibrium and is inferred from the comparison between the formation energy of the oxygen defect and that of its dissociation products. We find that As_{Ga} and V_{Ga} defects are the most stable ones among those considered for bulk GaAs. The $\text{V}_{\text{Ga}}\text{-As}_{\text{Ga}}/\text{V}_{\text{As}}\text{-2As}_{\text{Ga}}$ defect complex shows low formation energies and amphoteric nature in agreement with the Fermi-level pinning observed in radiation damaged GaAs.

In Chapter 4, we study O-defects in GaAs. The set of considered defects comprises the bridging O atom in a As–O–Ga configuration, interstitial O atoms in tetrahedral sites, and O atoms substitutional to both Ga (O_{Ga}) and As atoms (O_{As}). Particular care has been taken in the study of the O_{As} as this defect has previously been suggested to correspond to the experimental Ga–O–Ga defect. This defect center shows amphoteric behavior which could lead to Fermi-level pinning, but the calculated charge transition levels only moderately agree with the experimental pinning level. Furthermore, the first-neighbor shell of the O atom and the absence of negative-U behavior clearly contrast with the experimental characterization, leading to the conclusion that this defect does not correspond to the Ga–O–Ga defect. In addition, we consider an As vacancy containing two O atoms, for which the most stable configurations are found through the use of molecular dynamics simulations, and defect complexes involving an O_{As} defect bound to either one or two As_{Ga} antisites, denoted $\text{As}_{\text{Ga}}\text{-O}_{\text{As}}$ and $(\text{As}_{\text{Ga}})_2\text{-O}_{\text{As}}$, respectively. We examine the actual occurrence of complex O-defect through the application of the above mentioned criteria. We find that the bridging O defect and the $\text{As}_{\text{Ga}}\text{-O}_{\text{As}}$ and $(\text{As}_{\text{Ga}})_2\text{-O}_{\text{As}}$ complexes are the most stable oxygen defects in GaAs and that they satisfy the above-mentioned criteria. Further analysis in cooled down conditions, leads us to dismiss the $\text{As}_{\text{Ga}}\text{-O}_{\text{As}}$ defect due to the preferred bonding of two rather than one As_{Ga} antisites. We conclude that only the bridging O defect and the $(\text{As}_{\text{Ga}})_2\text{-O}_{\text{As}}$ complex are expected to occur. The nearest neighbor environment, the Fermi-level pinning position, and the optical transition energies between charge states of the latter defect are in excellent agreement with experiment.

Partially oxidized GaAs structures are considered in Chapter 5. We simulate the oxidation of the GaAs(110) surface through molecular dynamics (MD) and nudged-elastic band (NEB) calculations. We observe the natural formation of a bistable defect occurring in the form of an As–As dimer or in the form of two opposite As dangling bonds (As–As dimer/DB defect). Finally, we investigate structural and electronic properties of the Ga-As suboxide, representative of the transition region at the GaAs/oxide interface. Two amorphous models generated by quenches from the melt are taken under consideration. The absence of As–O bonds indicates that the structure is a mixture of GaAs and Ga-oxide, in accord with photoemission experiments. The band edges of the models are found to be closely aligned to those of GaAs. The simulation of charging and discharging processes leads to the identification of the As–As dimer/DB defect which introduces a charge transition level at ~ 0.7 eV above the GaAs valence band maximum, in good agreement with the experimental density of interface states.

In Chapter 6, we study the electrical properties of abrupt GaAs/Al₂O₃ interfaces. Through a three step alignment procedure we calculate band offset between GaAs and an amorphous model of Al₂O₃ obtained via a quench from the melt through MD simulations. Our results support the XPS measurements indicating a valence band offset of 3.8 eV, and show that the band offsets are marginally affected by the occurrence of defects at the interface. Then, we study a set of candidate defects for the Fermi-level pinning at the GaAs/oxide interfaces. This set of defects comprises both bulk-like and interfacial defects, including As antisites, Ga and As dangling bonds, the As–As dimer/DB defect, and several defect complexes. The defects are generated within atomistic model structures representing the GaAs/Al₂O₃ interface. Formation energies of bulk-like defects located in the vicinity of the interface are obtained and compared with those of corresponding bulk defects, while interfacial defects, which do not have a bulk analogue, are studied through their relative defect energies. Defect levels are defined as thermodynamic transition levels between different charge states and are calculated for all considered defects. Through an alignment procedure based on hybrid functional calculations, the defect levels are then positioned within the calculated band gap of GaAs which reproduces the experimental one, thereby enabling direct comparisons with the experimental density of defect states. Our study shows that several As-related defects show a similar amphoteric bistability between an As–As dimer state and a configuration with two doubly occupied As dangling bonds. The associated charge transition levels generally lie in the mid-gap region, in accord with experimental observations. This mechanism is proposed as the origin of the observed Fermi-level pinning at GaAs/oxide interfaces. Finally, we extend the study of interface defects to the In_{0.53}Ga_{0.47}As/oxide interface, considering the occurrence of the bistable As–As defect. The defect charge transition level is found to be resonant with the bottom of the In_{0.53}Ga_{0.47}As conduction band and weakly sensitive to its local chemical environment. Hence, this defect is a possible candidate for the observed defect density in the conduction band of In_{0.53}Ga_{0.47}As.

2 Computational Methods and Theoretical Background

In Section 2.1, the semilocal and the hybrid approximations to density functional theory are discussed focusing on their use in study of defect. In Section 2.2, we discuss our computational schemes and the main techniques used in this work, while in Section 2.3 we discuss the electron counting rule. The methodology used for the calculation of defect formation energies and charge transition levels is presented in Section 2.4. Finally, in Section 2.5 we describe the adopted finite-size correction scheme. Parts of this Chapter can be found in peer-reviewed articles [1].

2.1 Hybrid density functional theory applied to the study of defects

Density functional theory (DFT) is the method of choice for computing material properties in chemistry and physics. This theory is based on the Hohenberg-Kohn theorem [138] and on the Kohn-Sham ansatz [139]. Density functional theory is exact but the functional form of the exchange-correlation (XC) functional is not known and thus approximated. The simplest approximation is the local density approximation (LDA) in which the exchange-correlation functional depends locally on the electronic density. This approximation is valuable for systems with slowly varying density. In the generalized gradient approximation (GGA), the XC functional also depends on the gradient of the electronic density. The functional proposed by Perdew, Burke, and Ernzerhof (PBE) is a GGA functional and is largely used owing to its simplicity and accuracy [140]. However, it suffers from the band gap underestimation problem as all local and semilocal functionals. A valid alternative is represented by hybrid functionals which are able to overcome this problem. These functionals combine the exchange of the GGA functional with a fraction of exact-exchange derived from the Hartree-Fock (HF) method. They represent the forefront of density functional methods but are computationally demanding in terms of storage and computational time.

PBE and HSE functionals

Local and semilocal functionals are suitable for the study of defects as they give good structural, magnetic and energetic properties of defects in solids. However, they are not equally successful in the determination of defect charge transition levels because of the well known band gap

underestimation problem [141, 142]. Generally, local and semilocal functionals underestimate the semiconductor band gap by 40% or more [143], and tend to delocalize electronic states (including defects states). One deficiency of such semilocal schemes is the self-interaction error [142, 143], which arises from the fact that the interaction of one electron with itself, which is included in the Hartree energy term, is not perfectly canceled in the exchange-correlation term. It is important to mention that in other methods, such as the Hartree-Fock, this spurious interaction is perfectly canceled by the Fock integrals. However, the disadvantages of this method overcome its advantages and make it inadequate for most applications. The lack of correlation effects and the tendency to overlocalize electronic states lead to insufficiently accurate results. For instance, the band gaps of semiconductors are generally overestimated [144]. Moreover, since the Hartree-Fock potential involves four-center integrals, this method results in a high computational cost [142].

Starting from the adiabatic connection formula and adopting a simple linear interpolation, Becke proposed the "half-and-half" hybrid functional which mixes half of the semilocal exchange and half of the Fock integral [145]. Actually, the weight of Fock integral to be included into the calculation of the exchange energy depends on the considered material but a general rational favors a fraction of 25% which is shown to give the smallest mean absolute error for atomization energy for a set of molecules [146]. The resulting exchange energy (E_x) of a hybrid functional is then written as:

$$E_x^{\text{hybrid}} = \alpha E_x^{\text{Fock}} + (1 - \alpha) E_x^{\text{GGA}}, \quad (2.1)$$

with $\alpha=0.25$. The hybrid functional proposed by Heyd, Scuseria, and Ernzerhof (HSE), introduces a range separation of the Fock integral by re-writing:

$$\frac{1}{r} = \underbrace{\frac{\text{erfc}(\omega r)}{r}}_{\text{SR}} + \underbrace{\frac{\text{erf}(\omega r)}{r}}_{\text{LR}}, \quad (2.2)$$

where r is the electron-electron distance, $\text{erfc}(\omega r) = 1 - \text{erf}(\omega r)$ and ω a second adjustable parameter. In this way, only the short-range of the Fock-integral is added to the semilocal exchange:

$$E_x^{\text{HSE}} = \alpha E_x^{\text{Fock,SR}}(\omega) + (1 - \alpha) E_x^{\text{GGA,SR}}(\omega) + E_x^{\text{GGA,LR}}(\omega), \quad (2.3)$$

with the parameter ω set to 0.11 bohr^{-1} allowing speed up and providing a good accuracy [147, 148]. As mentioned above, the parameter α is material dependent and can be tuned to reproduce some properties of the material. In this respect, hybrid functionals can reproduce the experimental band gap of semiconductors. In particular, a linear dependence exists between the calculated band gap and the parameter α [149].

Band gaps and defect charge transition levels calculated within the PBE and HSE functionals can be compared upon alignment with respect to a common reference [149, 150]. The alignment of band structures is done through considering a common reference, such as the vacuum level. This procedure requires the calculation of the surface of the compound and includes the effect of the surface dipole, which can depend on the functional. When comparing semilocal and hybrid calculations, the electrostatic line-ups in the two schemes do not differ by more

than some tenths of an electronvolt. This implies similar surface dipoles and therefore a similar alignment of the average electrostatic potential in the material with respect to the vacuum [151]. The latter is more easily computed since it requires only a bulk calculation. Under these assumptions, the electrostatic average potential is a good reference for aligning band structures of crystalline solids. Focusing on the calculated band gaps, the comparison between the PBE and HSE functionals leads to the determination of relative band-edges shifts in analogy to the band offsets originated from interface calculations [149, 150]. The use of hybrid functionals is responsible for a band gap opening with respect to the PBE result which affects both the position of the VBM and the CBM [149, 150]. In particular in semilocal calculation the VBM is typically too high in energy and the CBM too low [144, 149, 150]. Concerning calculated defect levels of well localized defect states, a correspondence between the two kind of functionals has been shown [150]. Indeed, upon alignment with respect to the electrostatic potential, the difference between calculated defect levels is generally smaller than ~ 0.2 eV.

For completeness, we also discuss an alternative alignment scheme which has often been used in the literature [42, 43, 45, 129]. The a posteriori application of a scissor operator consists in rigidly shifting the CBM calculated at the PBE level to a higher energy until the experimental band gap is recovered. This alignment scheme erroneously assumes that only the wrong position of the CBM in the semilocal calculation is at the origin the band gap underestimation problem. This results in a misalignment between the PBE and HSE defect levels. Moreover, the use of an a posteriori correction to the band gap leaves the band gap unaffected during the calculation, allowing the defect state to hybridize with the host bands. In these cases, the defect state is no longer well described, as it can completely delocalize [152].

2.2 Computational methods and details

To carry out a defect study, we use structural relaxation, molecular dynamics (MD), and nudged-elastic band (NEB) techniques. These methods allow atoms to move according to forces. Once the electronic density is computed, the total force acting on the atoms is calculated through the Hellmann-Feynman theorem [153]:

$$\mathbf{F}_i = -\frac{\partial \langle H \rangle}{\partial \mathbf{R}_i} = -\left\langle \frac{\partial H}{\partial \mathbf{R}_i} \right\rangle, \quad (2.4)$$

where \mathbf{R}_i represents the atomic position and H the Hamiltonian operator which describes the electronic problem. Structural relaxations are performed at zero temperature. The atoms are moved until the residual force is smaller than a threshold value.¹

Molecular Dynamics

In a molecular dynamics simulation, the temperature of the system has a finite value, and the motion of the atoms is governed by Newtonian laws. The numerical integration of the equation of motions can be achieved through different algorithms, we use the Velocity Verlet method as implemented in the Quantum-ESPRESSO suite of programs [154]. In a MD simulation, the

¹We adopt a threshold of $2.5 \cdot 10^{-3}$ eV/Å throughout this work.

temperature can be controlled through the use of thermostats which affect the velocity of the particles. Among the simplest thermostats, the velocity rescaling method ensures that the temperature remains within a defined temperature range by rescaling the atomic velocities. In this work, we adopt this method for exploring the configuration space of defects or for equilibrating amorphous models at a given temperature. In the Berendsen thermostat the system is coupled to an external thermal bath [155]. This thermostat acts by rescaling the atomic velocities so that the temperature of the system is corrected in order to exponentially match the temperature of the bath according to:

$$\frac{dT}{dt} = \frac{T_0 - T}{\tau}, \quad (2.5)$$

where τ is the exponential time constant. We use this thermostat for quenching the melt of our amorphous models.

Nudged-elastic band

The NEB method allows one to identify the minimum energy path (MEP) which connects two minima in configurational space [156, 157]. It is an evolution of the chain-of-states method in which a chain of images of the system is generated between the initial and the final states in order to trace out a path. All these images are optimized simultaneously in a concerted way in order to converge to the minimum energy path and eventually find the configuration of the transition state (TS). Consecutive images are connected through springs of zero natural length, so that the dynamics of each image on the potential energy surface is driven by a combination of the spring forces and of the potential energy curvature. This method suffers from corner cutting and sliding down problems [156]. These difficulties can be easily overcome through the nudging procedure implemented in the NEB method. It corresponds to a projection of the forces acting on a single image. Along the direction of the path, the method only considers the spring term while in the direction perpendicular to the path it takes into account the surface potential term. The force acting on image i can then be expressed as:

$$\mathbf{F}_i = -[\nabla V(\mathbf{R}_i) - \nabla V(\mathbf{R}_i) \cdot \hat{\tau}_{||} \hat{\tau}_{||}] + \mathbf{F}_i^s \cdot \hat{\tau}_{||} \hat{\tau}_{||}, \quad (2.6)$$

$\nabla \mathbf{a}$ where $\hat{\tau}_{||}$ indicates the direction parallel to the path and \mathbf{F}_i^s is the spring force acting on image i . The climbing-image extension allows one to identify the structure of the transition state at the saddle point [157]. The image with the highest energy does not feel the effect of the springs and is subject to a force component along the path acting with an opposite sign. In this way, this image (called climbing image) tries to maximize its energy along the path and to minimize it in the other directions, reaching in this way the transition state of the reaction.

Computational scheme

In the present work, all defect structures are obtained through full structural relaxation carried out within a density-functional-theory framework in which the exchange-correlation energy is described through the PBE approximation [140]. We use plane-wave basis sets defined by a kinetic energy cutoff of 50 Ry in molecular dynamics calculations and of 70 Ry in relaxations of the atomic and electronic structures. We use normconserving pseudopotentials as imple-

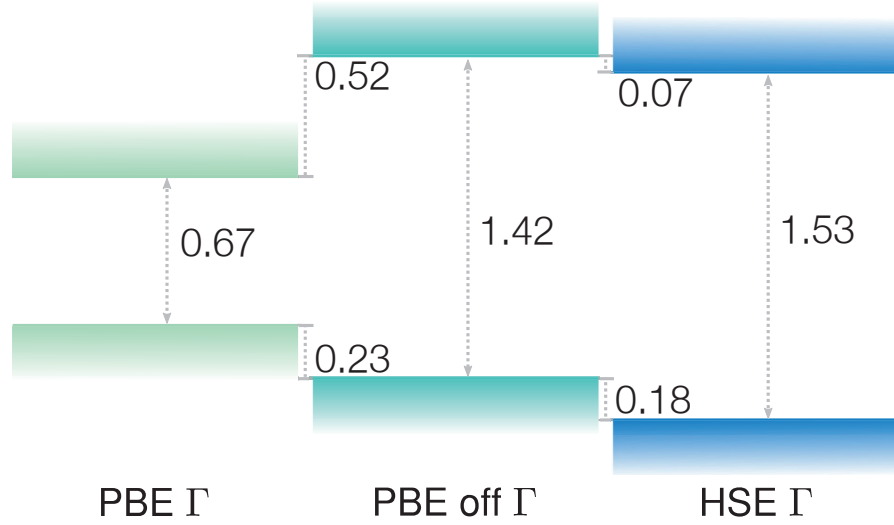


Figure 2.1 – Calculated band gaps of GaAs as obtained at the PBE (PBE Γ) and HSE levels (HSE Γ) with \mathbf{k} -point samplings including the Γ point. The middle panel corresponds to a PBE calculation with an off-center $2 \times 2 \times 2$ \mathbf{k} -point mesh (PBE off Γ). The band structures are aligned through the average electrostatic potential. [149, 150, 151] Band gaps and band offsets are in eV. The valence band in the HSE representation has been shifted upwards by 0.1 eV to account for spin-orbit effects, as suggested in Ref. [160].

mented in the Quantum-ESPRESSO suite of programs [154]. We model the GaAs compound using the experimental lattice parameter of 5.65 Å (Ref. [14]), which differs from the PBE equilibrium value by less than 1%. A detailed description of the supercell is reported at the beginning of each Chapter. For determining the band edges of GaAs, we perform hybrid functional calculations for bulk GaAs. We use the HSE hybrid functional implemented in the Quantum-ESPRESSO suite of programs as described in Ref. [158]. The nonlocal exchange potential is treated as described in Ref. [159]. We adopt the original range-separation parameter ($\mu = 0.11 \text{ bohr}^{-1}$, Ref. [148]) to preserve the overall accuracy of the functional [158]. However, we set the fraction of nonlocal Fock exchange to $\alpha = 0.35$ in order to reproduce the experimental band gap of GaAs ($E_g = 1.52 \text{ eV}$, Ref. [14]), following the scheme described in Ref. [160]. This value of α is significantly larger than used for other semiconductors such as Si ($\alpha=0.23$ [158]) and Ge ($\alpha=0.15$ [161]). A qualitative relation between the optimal α and the dielectric function is observed for many semiconductors and oxide compounds [149]. This relation inspired general formulas to predict the optimal α from the electronic density of the material [162]. However, it has been showed that this qualitative relation does not hold for materials with semicore 3d electrons such as Ge, GaAs, and ZnO [149]. Finally, we note that due to the range separation adopted in the HSE, the value of α required by this kind of functional is larger than that required for the PBE0 functional in which no range-separation occurs [158]. As far as the accuracy of hybrid functional calculations, we refer to a benchmark calculation involving the As_{Ga} antisite which shows that calculated charge transition levels can be expected to agree with their experimental counterparts within $\sim 0.2 \text{ eV}$ [160].

A comparison of the band gap of GaAs calculated through PBE and HSE functionals and aligned through the average electrostatic potential is shown in Fig. 2.1. We rely on a bulk

GaAs model containing 64 atoms and we use a $2 \times 2 \times 2$ \mathbf{k} -point mesh which ensures converged defect energies [123, 160]. The band gap of GaAs at the PBE level is particularly small (0.67 eV), favoring spurious hybridization effects between the localized defect states and the delocalized bands of the host [152]. The use of the HSE functional leads to conduction-band and valence-band shifts of +0.45 and -0.41 eV with respect to the PBE band edges, respectively. The hybrid VBM has been shifted upwards by 0.1 eV in order to account for the effect of spin orbit interactions following Ref. [160]. We note that the band gap achieved through the PBE functional with an off-center \mathbf{k} -point mesh spans almost the entirety of the HSE band gap giving access to defect states in a wide energy range. Indeed, the use of this mesh offers the advantage of opening the band gap in a similar way as the HSE functional. A small energy region in the vicinity of the valence band remains inaccessible through this approach, but an *a posteriori* check shows that only one of the defect levels obtained in this work is concerned. The use of a translated \mathbf{k} -point mesh allows us to reduce the computational cost of our calculations through the systematic use of the PBE functional for the calculation of the defect levels combined to the alignment to the HSE band-edges. Such a PBE scheme ensures a proper description of the charge localization during the structural relaxation, allowing us to avoid using hybrid functionals for structural relaxations which would imply a high computational cost and limit the number of considered defects. We note that a similar situation holds in our interface calculations, where a large band gap at the PBE level is achieved as a consequence of the quantum-confinement effect associated to GaAs slab calculation.

Therefore the present scheme does not yield relaxed model structures at the hybrid functional level. Nevertheless, such relaxations generally only yield minor structural changes. For instance, the present scheme yields charge transition levels of the As_{Ga} antisite at 0.46 and 0.94 eV above the valence band maximum, very close to respective levels at 0.51 and 0.92 eV obtained within a full HSE scheme in which also the relaxations are performed at the HSE level [160]. For particular defects, hybrid functionals may lead to asymmetric relaxations leading to more localized defect states, due to a better cancellation of the self-interaction [163, 164, 165, 166]. However, even in these cases, the defect energies are generally only marginally affected, as the asymmetric structure arises from a subtle competition between the delocalized and the localized state [165].

2.3 Electron counting rule

The electron counting rule is expected to govern the local electronic structure in III-V semiconductors [111]. In bulk GaAs, Ga and As atoms are tetrahedrally coordinated contributing to each bond with $3/4$ and $5/4$ electrons, respectively, as schematically shown in Fig. 2.2. This ensures that all bonds carry two electrons as required for closed shell systems. We apply this rule in the generation of interfacial models as it can be used to identify stable atomic arrangements. We also apply this rule to the study of new defect structures and in general we verify that all the defects we consider satisfy this rule. This rule also applies to defects involving a dopant atom such as oxygen. O atoms have six valence electrons and usually form two bonds contributing to each one with one electron. We then use this rule to assign fractional charge states to interfacial defects (*vide infra*), such as in the case of anion and cation DBs, and dimers.

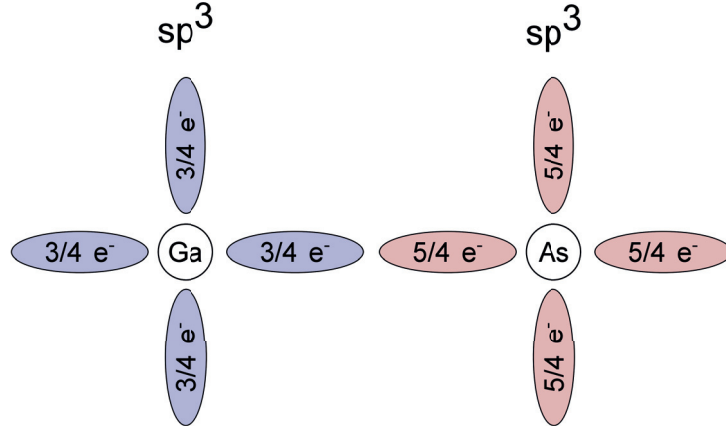


Figure 2.2 – Illustration of sp^3 hybridized Ga and As atom in GaAs, used as reference for the application of the electron counting rule.

2.4 Defect study

We calculate defect formation energies and thermodynamic charge transition levels. The formation energy of a charged defect $E_f(X^q)$ is a function of the Fermi energy (ϵ_F) given with respect to the valence band maximum (ϵ_v), according to Ref. [141]:

$$E_f(X^q) = E_{\text{tot}}[X^q] + E_{\text{corr}}^q - E_{\text{tot}}[\text{bulk}] - \sum_i n_i \mu_i + q(\epsilon_F + \epsilon_v + \Delta\nu_{0/b}), \quad (2.7)$$

where $E_{\text{tot}}[X^q]$ is the total energy of the supercell containing the charged defect X^q and $E_{\text{tot}}[\text{bulk}]$ the total energy of the pristine bulk supercell. For each species i , the chemical potential μ_i of the n_i added/removed atoms allows us to describe various experimental conditions. In this work, we adopt the As-rich condition which is the standard growth condition of GaAs for electronic applications [167, 168]. We obtain the As chemical potential μ_{As} from the tetrahedral As_4 molecule. μ_{Ga} is then derived from the equilibrium condition with GaAs, $\mu_{\text{Ga}} = \mu_{\text{GaAs}} - \mu_{\text{As}}$. The O chemical potential μ_{O} is taken to correspond to the isolated O_2 molecule or is derived from the equilibrium condition with $\beta\text{-Ga}_2\text{O}_3$,² as the occurrence of Ga oxides is observed during oxidation [101]. $\Delta\nu_{0/b}$ is a potential alignment term (PA) which accounts for the potential shift between the bulk and the neutral defect calculation [141, 152]. Finally, E_{corr}^q corrects for the finite-size error due to the long-range nature of the Coulomb interaction and the use of periodic boundary conditions. In the present work, we correct our results through the scheme proposed by Freysoldt, Neugebauer, and Van de Walle [170].

Defect charge transition levels correspond to Fermi energies at which the formation energies of competing charge states ($q1$ and $q2$) are equal:

$$\epsilon_{q1/q2} = \frac{E_{\text{tot}}[X^{q1}] + E_{\text{corr}}^{q1} - E_{\text{tot}}[X^{q2}] - E_{\text{corr}}^{q2}}{q2 - q1} - \epsilon_v - \Delta\nu_{0/b}. \quad (2.8)$$

²Lattice parameters of $\beta\text{-Ga}_2\text{O}_3$ calculated at the PBE level are $a = 12.26$, $b = 3.07$, and $c = 5.82$ Å, to be compared with experimental values of $a = 12.23$, $b = 3.04$, and $c = 5.80$ Å (Ref. [169]).

These levels can be directly compared to experimental defect levels identified through, for example, capacitance-voltage measurements.

2.5 Finite-size corrections

In the study of defects we generally aim at describing isolated defects. However, due to technical constraints the simulations are restricted to a limited number of atoms. To preserve periodicity at the border of the supercell, periodic boundary conditions are applied. This produces an infinite array of the simulated supercell and of the defect therein contained. Due to the long range nature of the Coulomb interaction, charged defects interact with their replicas affecting the calculated total energy. Indeed, the resulting total energy contains some spurious interactions which have to be removed. In particular, these energy terms correspond to the interaction within the infinite array of charges and to the interaction of the periodic potential with the background charge density. Indeed, a neutralizing charge density is added to the simulation cell in order to avoid the divergence of the electrostatic potential.

Bulk

To eliminate these energy contributions in bulk calculations, we apply the finite-size correction scheme proposed by Freysoldt, Neugebauer, and Van de Walle (FNV) [170], which is shown to be robust and meaningful for a large set of defects [152]. The main idea of this correction scheme is to calculate the above-mentioned spurious electrostatic interactions through a classical electrostatic model in which the defect charge distribution has a simple shape. Indeed, when the defect is well localized then a part of the spurious interactions are long-range and thus they do not depend on the shape of the charge density distribution (q_d). In practice, the electrostatic potential of such a localized defect state ($V_{q/0}$, obtained as difference of the total electrostatic potential of the charged and neutral defect) can be separated in a short-range and a long-range contribution:

$$V_{q/0} = V_q^{lr} + V_q^{sr}. \quad (2.9)$$

For the interaction which involves the short-range potential the method relies on the calculated DFT potentials considering an alignment term (vide infra). The periodic short-range potential (\tilde{V}_q^{sr}) is obtained from the superposition of the short-range potentials associated to the replica of the defect and, due to its short-range nature, can be simplified according to:

$$\tilde{V}_q^{sr} = \sum_{\mathbf{R}} V_q^{sr}(\mathbf{r} + \mathbf{R}) + C \approx V_q^{sr} + C, \quad (2.10)$$

for \mathbf{r} within the supercell. The constant C is required to reproduce the absolute position of the periodic potential. It is convenient to express the long range potential in the reciprocal space [$V_q^{lr}(\mathbf{G})$] using the Poisson equation:

$$V_q^{lr}(\mathbf{G}) = \frac{4\pi q(\mathbf{G})}{\epsilon|\mathbf{G}|^2}, \quad (2.11)$$

The periodic long-range potential (\tilde{V}_q^{lr}) corresponds to the Fourier series of this transformed potential:

$$\tilde{V}_q^{lr} = \frac{1}{\Omega} \sum_{\mathbf{G} \neq \mathbf{0}} V_q^{lr}(\mathbf{G}) \exp(i\mathbf{G} \cdot \mathbf{r}), \quad (2.12)$$

where Ω is the volume of the supercell and the first term $\mathbf{G} = \mathbf{0}$ is omitted to account for the compensating effect of the background. This long-range potential represents the Coulomb behavior of the defect potential and decays slowly with distance. It does not depend on the shape of the defect charge distribution and, within the correction scheme, it is calculated using a model charge, usually with a Gaussian distribution. The spurious interaction energy (E^{inter}) of the model charge and of the background charge distributions with the periodic long-range model potential ($\tilde{V}_q^{lr} - V_q^{lr}$) is given by:

$$E^{\text{inter}} = \frac{1}{2} \int_{\Omega} d^3\mathbf{r} [q_d(\mathbf{r}) + n] [\tilde{V}_q^{lr}(\mathbf{r}) - V_q^{lr}(\mathbf{r})] \quad (2.13)$$

where the prefactor $\frac{1}{2}$ accounts for the double counting and the integral is restricted to the supercell. A second spurious interaction energy (E^{intra}) comes from the interaction of the background charge with the defect inside the supercell and reads:

$$E^{\text{intra}} = \int_{\Omega} d^3\mathbf{r} n V_{q/0}(\mathbf{r}) = -q_d \left(\frac{1}{\Omega} \int_{\Omega} d^3\mathbf{r} V_{q/0}(\mathbf{r}) \right). \quad (2.14)$$

The opposite of the sum of these two energy contributions represent the finite-size correction energy applied to the defect formation energy. Using Eq. (2.9) and combining eqs. (2.13) and (2.14) the total correction energy (E_{corr}^q) is written in the form of $E_{\text{corr}}^q = E_{\text{isolated}} - E_{\text{periodic}} + q\Delta_{q/0}$, where:

$$E_{\text{isolated}} = \int_{\Omega} d^3\mathbf{r} \frac{1}{2} q_d(\mathbf{r}) V_q^{lr}(\mathbf{r}), \quad (2.15)$$

$$E_{\text{periodic}} = \int_{\Omega} d^3\mathbf{r} \frac{1}{2} (q_d(\mathbf{r}) + n) \tilde{V}_q^{lr}(\mathbf{r}), \quad (2.16)$$

and

$$\Delta_{q/0} = \frac{1}{\Omega} \int_{\Omega} d^3\mathbf{r} V_q^{sr}(\mathbf{r}) \quad (2.17)$$

with $V_q^{sr} = \tilde{V}_{q/0} - \tilde{V}_q^{lr} - C$ and the alignment constant C is chosen such that V_q^{sr} decays to zero in between the defects. The terms in eqs. (2.15) and (2.16) only depend on the long-range part of the potential and are then calculated through the model system. They respectively corresponds to the energy of an isolated Gaussian charge distribution and of a periodic array of charges with a neutralizing background. The term in Eq. (2.17) is an alignment term, has been demonstrated to correspond to the opposite of the constant C , and can be graphically determined.

Interfaces

A generalization to interfaces of this correction scheme has been developed in Ref. [171]. The presence of an interface introduces a discontinuity in the dielectric constant which affects the calculation of both E_{isolated} and E_{periodic} . The new E_{isolated} contribution to the correction energy can be calculated for a point charge near the interface through the method of the image charges. This method can be applied when the charge distribution is only found on one side of the interface. Considering the case in which the extra charge q is within the material with dielectric constant ϵ_1 and only one interface is present, the total potential on the side of the charge is:

$$V = \frac{1}{\epsilon_1} \left(\frac{q}{R_1} + \frac{q_{\text{image}}}{R_2} \right), \quad (2.18)$$

where R_1 and R_2 are the distances to the original charge q and to the image charge q_{image} , which corresponds to:

$$q_{\text{image}} = \frac{\epsilon_1 - \epsilon_2}{\epsilon_1 + \epsilon_2} q. \quad (2.19)$$

At $R_1 = 0$ the electrostatic energy of a point charge diverges. The self-energy is then calculated in analogy to the case of a bulk charge, relying a Gaussian model charge distribution. However, the point charge model gives the interaction with the image charge, corresponding to a contribution of:

$$E = \frac{q q_{\text{image}}}{4\epsilon_1 d}, \quad (2.20)$$

where d is the distance between q and q_{image} . The resulting E_{isolated} is then the sum of the bulk and this interfacial contribution. In the case in which two interfaces are present, multiple reflections must be taken under consideration. The resulting electrostatic energy is given by an infinite sum over images [171]. However, a more detailed treatment is required when the charge distribution is on both sides of the interface. The induced potential is calculated numerically by considering the charge distribution as a superposition of point charges. The integration of the potential suffers from the divergence of the potential at small distance from the charge. To overcome this problem, the Coulomb behavior $1/r$ is partitioned in long-range and short-range contributions:

$$\frac{1}{r} = \underbrace{\frac{\text{erf}(ar)}{r}}_{\text{LR}} + \underbrace{\frac{\text{erfc}(ar)}{r}}_{\text{SR}}, \quad (2.21)$$

where the range separation length a , is taken such that a^{-1} has the same order as the distance between two adjacent points in the real space mesh. In this way, the long-range term does not diverge anymore and the energy contribution of the short-range term can be analytically evaluated under the assumption that, within this range, the charge density is constant:

$$E = q(r) \int_{\Omega} \left[\frac{\text{erfc}(ar)}{r} \right] 4\pi r^2 dr = q(r) \frac{\pi}{4a^2}. \quad (2.22)$$

In the case of a charge localized on a surface, this approach has been shown to yield a result equivalent to that extrapolated from the scaling of E_{periodic} . As far as the E_{periodic} term is concerned, the variation of the dielectric function profile along the interface affects the periodic long-range potential [cf. Eq. (2.11)]. However, this discontinuity can be modeled through the use of an error-function:

$$\epsilon(z) = \frac{1}{2}(\epsilon_2 - \epsilon_1) \cdot \text{erf}[(z - z_0)/\beta] + \frac{1}{2}(\epsilon_1 + \epsilon_2), \quad (2.23)$$

where z_0 represents the position of the interface, ϵ_1 and ϵ_2 the dielectric constant on either side of the interface, and β the smoothness of the dielectric-constant profile [171]. With this form, the standard expression of the Poisson equation can be recovered and the periodic long-range potential evaluated. The finite-size correction is then written as $E_{\text{corr}}^q = E_{\text{isolated}} - E_{\text{periodic}} + q\Delta_{q/0}$, where the alignment term $\Delta_{q/0}$ is determined graphically in analogy to the bulk case.

3 Intrinsic defects in bulk GaAs

In this Chapter we present structural and electrical properties of intrinsic defects occurring in bulk GaAs. In particular, we focus on bistable defects which have been proposed to underlie the Fermi-level pinning in radiation-damaged GaAs. The irradiation of GaAs induces a Fermi-level shift towards the "ultimate" position at ~ 0.6 eV above VBM [127, 128]. It is proposed that the irradiation process produces electrically active intrinsic defects which shift the Fermi level within the band gap and ultimately pin it. Previous density functional calculations pointed out the role of bistable Ga and As vacancies, which are expected to be amphoteric [129, 130, 131].

Thus, here we study Ga and As antisites (Ga_{As} and As_{Ga}), Ga and As vacancies (V_{Ga} and V_{As}) including their bistable forms, and other complex defects involving vacancies and As_{Ga} . We neglect the occurrence of interstitial as previous calculations reveal their high formation energy [131]. Some of these results have been already discussed in peer-reviewed article [172].

Computational Details

The defects are studied in 64-atom supercells. For relax the atomic structures we use the PBE functional while the electronic structure is relaxed through the HSE functional setting the parameters to the values described in Chapter 2. We use a translated $2 \times 2 \times 2$ \mathbf{k} -mesh following Refs. [123, 160].

Criteria for the occurrence of defect complexes

In this study, we consider the occurrence of defect complexes ($D_1 D_2$) corresponding to the binding of defects D_1 and D_2 . In order to assess whether a specific defect complex occurs, we here adopt two criteria [141].

The first criterion concerns the relative stability between the defect complex and its dissociation products. We define the complex dissociation energy (E_{dissoc}) as a binding energy [141, 173]:

$$E_{\text{dissoc}} = -[E_{\text{f}}(D_1 D_2) - E_{\text{f}}(D_1) - E_{\text{f}}(D_2)], \quad (3.1)$$

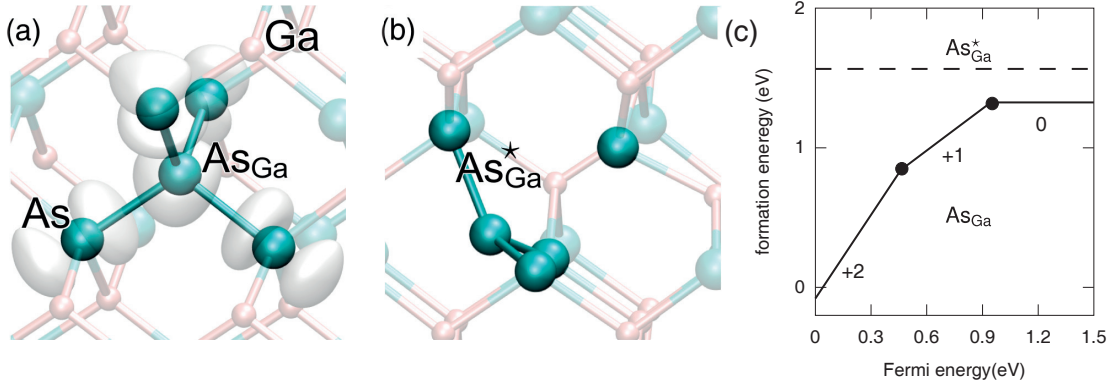


Figure 3.1 – As_{Ga} defect: relaxed structure in the neutral charge state (a) stable structure, (b) metastable structure. The charge density of the stable defect state is shown in transparency in panel (a). (c) Formation energies vs Fermi energy. The metastable configuration is indicated as As_{Ga}^* .

where the dissociation products are the isolated defect D_1 and D_2 . By this definition, E_{dissoc} is a function of Fermi energy. The sign of E_{dissoc} notifies whether the defect complex is stable upon dissociation. A positive value supports the stability of the defect complex, while a negative value indicates that the isolated dissociation products are favored and that the complex does not occur [141]. We note that E_{dissoc} does not depend on the references defining the chemical potentials. This stability criterion therefore holds irrespective of specific growth conditions.

Following Ref. [141], the second criterion depends on the defect equilibrium concentration which is derived from the defect formation energy through the following relation:

$$[X^q] = N_{\text{sites}} \cdot N_{\text{config}} \exp[-E_f(X^q)/kT], \quad (3.2)$$

where N_{sites} is the number of sites per unit volume in which the defect can be incorporated, N_{config} the number of equivalent defect configurations, k Boltzmann's constant, and T the temperature. The concentration of the defect complex dominates over that of its dissociation products when $E_f(D_1 D_2)$ is smaller than $E_f(D_1)$ and $E_f(D_2)$. This second criterion therefore informs us about the relevance of the defect complex concentration at thermal equilibrium. We note that, unlike the criterion based on the dissociation energy, the present one depends on the chemical potentials adopted in definition of the defect formation energy [141]. Indeed, this reflects the fact that the ratio between the concentrations of different defects depends on growth conditions.

As_{Ga}

The occurrence of the As_{Ga} defect in GaAs has been experimentally pointed out through the study of SI properties, suggesting that the As_{Ga} defect corresponds to the EL2 defect (cf. Section 1.2). To account for the experimental observation regarding the EL2 defect, it has been shown that the neutral state of the As_{Ga} defect can exist in a metastable structure

(As_{Ga}^{*}) [29]. In this configuration an As–As has been broken favoring the formation of As DBs on the resulting threefold coordinated As atoms, with the priorly As antisite atom displaced to a nearby interstitial position. The occurrence of the As_{Ga} defect at GaAs/oxide interfaces has also been suggested, to underlie the observed Fermi-level pinning behavior in both experimental and theoretical studies [106, 123].

In the stable neutral charge state the As antisite atom occupies the high symmetry T_d site forming four equivalent As–As bonds with bond length 2.58 Å [Fig. 3.1(a)]. The application of the electron counting rule reveals the presence of two extra electrons in one defect orbital. The charge density of the defect state is reported in transparency in Fig. 3.1(a) and shows that it is localized on the As antisite atom and its four nearest neighbors. In the charge state +1 and +2, the As–As bond length is reduced to 2.55 and 2.50 Å, respectively. We also consider the neutral metastable configuration in which the As antisite atom occupies a C_{3v} site as shown in Fig. 3.1(b). The As antisite atom binds three As atoms facing the Ga vacancy site (bond length 2.48 Å) and is distant 3.48 Å from the forth As atom facing the Ga vacancy.

The calculated formation energies of the As_{Ga} defect vs Fermi-energy are shown in Fig. 3.1(c) for As-rich conditions. Finite-size correction energies are 0.10 and 0.52 eV for charge states +1 and +2, respectively. The stable charge states confirm the double donor nature of this defect, in accord with experiments [27]. Calculated charge transition levels fall at 0.46 and 0.92 eV above the VBM, in agreement with previous hybrid functional results [160], and not far from the experimental values (0.5 and 0.75 eV) [27]. The formation energy in *p*-type conditions is –0.08 eV and 1.32 in *n*-type conditions. This shows that the formation of the As_{Ga} defect is favored when the Fermi energy lies close to the VBM. The formation of the metastable As_{Ga}^{*} costs 1.56 eV, being 0.21 eV higher than the stable neutral As_{Ga} configuration. We note that the As_{Ga} defect introduces two defect states at midgap in accord with the density of defect states measured at the interface. However, due to its donor nature, the As_{Ga} defect pushes the Fermi energy to the upper part of the GaAs band gap. Then, the occurrence of only the As_{Ga} does not lead to Fermi-level pinning as described in Section 1.3.

In Fig. 3.2, we assess the accuracy of our computational approach comparing the As_{Ga} charge transition levels as calculated through different schemes. We consider the defect atomic structures as relaxed within the semilocal PBE functional, and we optimize the electronic structure through the use of PBE (blue lines) and HSE (black lines) functionals. Finally, the defect formation energies are given with respect to the bulk GaAs band gap obtained through the HSE functional. The two approaches give very close charge transition levels. Within the PBE approach, the charge transition levels fall at 0.51 and 0.91 eV above the VBM, to be compared with the values obtained within the HSE approach (0.46 and 0.92 eV above VBM). Moreover, the agreement with a full-HSE approach is also very good. Indeed, upon HSE structural relaxation the As_{Ga} charge transition levels fall at 0.51 and 0.92 eV above the VBM [160].

Ga_{As}

The formation of the Ga_{As} defect together with the As_{Ga} defect, has been invoked by Spicer as responsible, for the Fermi-level pinning at the surface in his "unified defect model" [52, 54, 55].

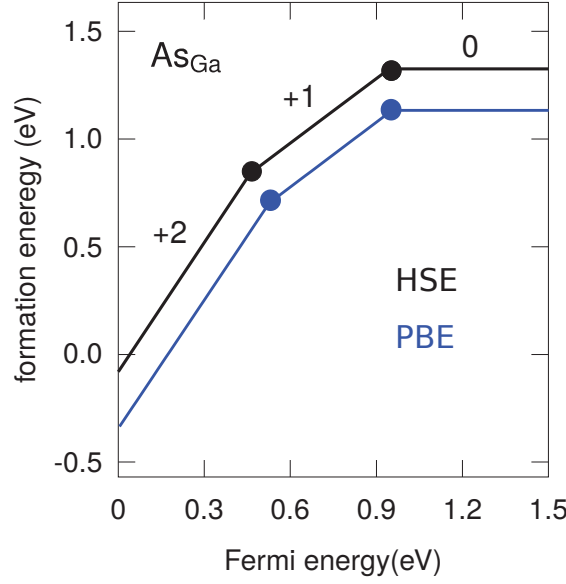


Figure 3.2 – Formation energies vs Fermi level for the As_{Ga} defect as calculated through two different computational schemes. PBE (blue lines) indicates PBE relaxed atomic and electronic structures aligned to the HSE bulk band gap, HSE (black lines) indicates PBE relaxed atomic structure and HSE relaxed electronic structure aligned to the HSE bulk band gap.

In the neutral charge state the Ga antisite atom occupies the tetrahedral site forming four equivalent bonds of length 2.41 Å [Fig. 3.3(a)]. The application of the electron counting rule reveals that the system lacks two electrons to doubly occupy all the bonds. In the charge states -1 and -2 , the Ga–Ga bond lengths are progressively reduced to 2.38 and 2.34 Å. Finally, in the charge state $+1$ the Ga–Ga bond lengths is 2.46 Å.

The formation energy of the Ga_{As} defect calculated in As-rich conditions ranges between 2.66 and 4.30 eV, as shown in Fig. 3.3(b). Calculated charge transition levels falls at 0.15, 0.42, and 0.94 eV above the VBM, in good agreement with previous calculations [123]. Applied finite size corrections are 0.16, 0.17, and 0.68 eV for charge states $+1$, -1 , and -2 , respectively. The high formation energy of the Ga_{As} defect disfavors its formation in bulk GaAs.

Finally, we note that the charge transition level between the $+1$ and the neutral charge states falls in the 0.18 eV right above VBM where the accuracy of our mixed HSE scheme is not guaranteed. In order to study the localized behavior of this defect state we analyse the screening charge density as suggested in Refs. [152, 174]. Indeed, the total screening charge density (ρ_{scr}) can conceptually be divided in localized and delocalized contributions according to:

$$\rho_{\text{scr}} = \rho_{\text{scr}}^{\text{loc}} + \rho_{\text{scr}}^{\text{deloc}}. \quad (3.3)$$

The localized defect charge distribution is screened by a localized charge distribution $\rho_{\text{scr}}^{\text{loc}}$ which corresponds to a charge of $-(1-1/\epsilon)q$ and is located close to the defect. Moreover, since the charge neutrality of the supercell is preserved, the localized screening charge comes from the supercell. This gives rise to a delocalized, quite uniform charge distribution, which is

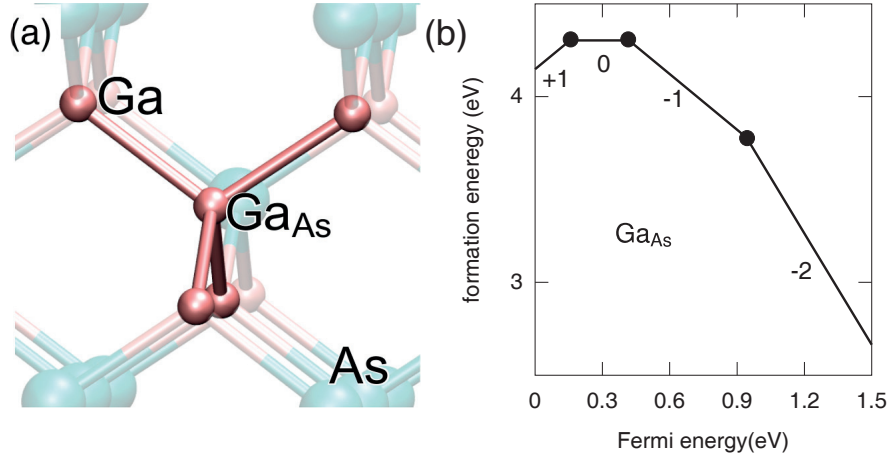


Figure 3.3 – Ga_{As} defect: (a) relaxed structure in the neutral charge state and (b) formation energies vs Fermi energy.

denoted $\rho_{\text{scr}}^{\text{deloc}}$ and has opposite sign with respect to $\rho_{\text{scr}}^{\text{loc}}$ [174]. The DFT screening charge obtained for the charge state +1 of the Ga_{As} defect located at the origin is shown in Fig. 3.4 (blue line). The analytic limit for the delocalized defect charge distribution is also shown (red dashed line). Far from the defect, the DFT charge density does not correspond to the analytic limit indicating that the localized charge is different from that expected. A measure of the defect charge localization can be obtained by fitting the DFT screening charge with a function of the form $(1-\eta/\epsilon)q$, where $0 \leq \eta \leq 1$ gives the fraction of the defect charge localization. The result of such a fit is shown in Fig. 3.4 (green dashed line) for charge densities obtained at the PBE level. The fitted value for η is 0.7, thus corresponding to a 70% localization of the unrelaxed defect. The defect delocalization is due to the inter-mixing of the defect state with the delocalized states of the host [152]. However, we expect that during the structural relaxation of the defect, the fraction of the defect state localization has increased. Further improvement of the result is possible though HSE structural relaxations, but given the overall high formation energy of the present defect, and the purposes of the present work we leave this study for future investigations.

V_{Ga}

Previous computational results suggested that Ga and As vacancies in GaAs underlie the Fermi-level pinning observed upon radiation damaging [127, 128, 129]. Indeed, these defects have been predicted to show bistability and amphoteric behavior [129].

In the case of V_{Ga} , the bistability consists in the diffusion of an As atom facing the V_{Ga} defect into the vacancy, leading to the formation of an As vacancy bound to an As antisite ($V_{\text{As}}\text{-As}_{\text{Ga}}$) according to:



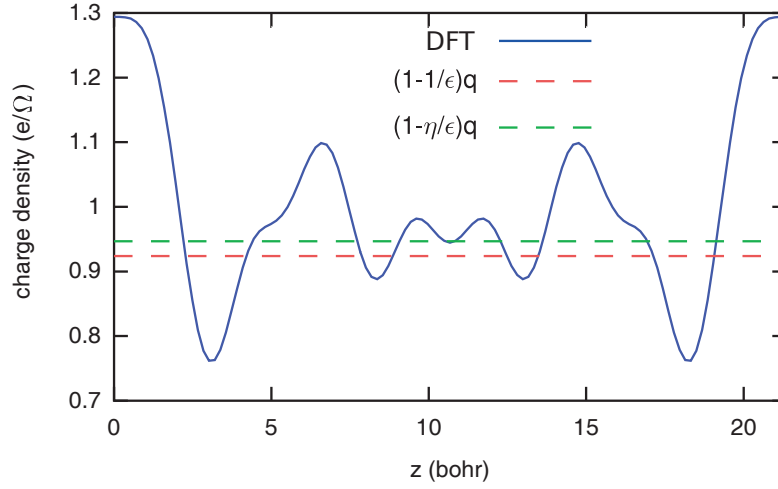


Figure 3.4 – Planar-averaged charge density difference across the supercell for the $\text{Ga}_{\text{As}}^{+1}$ defect as obtained at the PBE level. The difference is taken between the charge densities of the charged and neutral defect unrelaxed. The level corresponding to the homogeneously distributed screening charge $(1 - 1/\epsilon)q/\Omega$ is indicated (dashed, red). The dashed, green line is obtained through a fit and corresponds to $(1 - \eta/\epsilon)q/\Omega$ with $\eta = 0.7$. The charge density is broadened through a Gaussian function with a width of 0.44 bohr.

The application of the electron counting rule to the neutral V_{Ga} defect reveals the absence of 3 electrons to saturate all the bonds. We find stability for the -2 and -3 charge states which show similar defect structures. The four As atoms facing the Ga vacancy relax inwards by 0.35 Å as shown in Fig. 3.5(a) for the charge state -2 . The $\text{V}_{\text{As}}\text{-As}_{\text{Ga}}$ defect is found to be stable in the $+3$ charge state. The As_{Ga} atom forms three As–As bonds with length 2.51 Å (0.06 Å larger than the typical Ga–As bond length) and the Ga atoms facing the V_{As} relax outwards the vacancy by 0.42 Å as shown in Fig. 3.5(b). This defect state satisfies the electron counting rule.

Calculated formation energies of the bistable V_{Ga} defect are shown in Fig. 3.5(c) through black lines. Finite-size corrections applied to the $+3$, -2 , and $+3$ charge states amount to 0.74, 0.44, and 1.11 eV, respectively. The formation energy ranges between 2.93 eV (close to the VBM) and -0.38 eV (at the CBM). In p -type conditions, the formation of the $\text{V}_{\text{As}}\text{-As}_{\text{Ga}}$ defect amounts to 2.11 eV. In n -type conditions the formation of the V_{Ga} is preferred and the formation energy amounts to -0.38 eV. The calculated charge transition levels fall at 0.27 and 0.74 eV above the VBM. The stability of the $\text{V}_{\text{As}}\text{-As}_{\text{Ga}}$ defect state confers metastable behavior to the charge states 0 and -1 of V_{Ga} defect, previously identified [175]. Here, we have considered these charge states in their most stable spin configuration as described in Ref. [175], but the $+3$ charge state of the $\text{V}_{\text{As}}\text{-As}_{\text{Ga}}$ defect complex has shown a lower formation energy. The bistability nature of the $\text{V}_{\text{Ga}}/\text{V}_{\text{As}}\text{-As}_{\text{Ga}}$ defect confers amphoteric behavior, which can cause Fermi-level pinning at the $+3/-2$ charge transition level (0.27 eV above the VBM). This level disagrees with previous semilocal density functional calculations [129, 130] because of the use of a different alignment scheme. Furthermore, this calculated level is somewhat lower than the Fermi-level pinning at 0.6 eV above the VBM observed in radiation damaged GaAs samples [127, 128]. However, we note that the present findings agree with the observation of

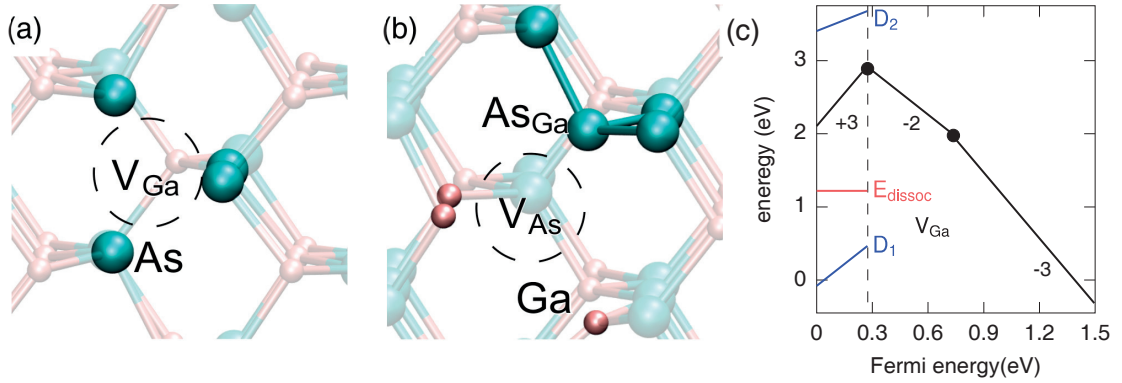


Figure 3.5 – V_{Ga}/V_{As} - As_{Ga} defect: stable relaxed structure in the charge states (a) -2 and (b) $+3$. In (b) the stable defect structure consists in an As vacancy and a neighboring As antisite, leading to the V_{As} - As_{Ga} defect complex. (c) formation energies vs Fermi energy (black lines) of the bistable V_{Ga}/V_{As} - As_{Ga} defect and binding energy of the V_{As} - As_{Ga} defect complex (red lines). In (c), the formation energies of the dissociation products, the As_{Ga} defect (D_1) and the V_{As} defect (D_2) are shown (blue lines).

an acceptor level at ~ 0.3 above VBM in low-temperature MBE grown GaAs samples [176]. This material usually contains As excess and is found to incorporate high concentrations of As_{Ga} and V_{Ga} defects [177].

The dissociation energy of the V_{As} - As_{Ga} defect complex is calculated in the Fermi energy range that admits the existence of the complex, considering the following dissociation reaction:



The formation energies of the dissociation products are also reported in Fig. 3.5(c), D_1 corresponds to the isolated As_{Ga} defect and D_2 to the isolated V_{As} defect. The dissociation energy is then obtained as the opposite of the difference between the formation energy of the complex and those of the dissociation products according to eq. (3.1). The dissociation energy is positive in the Fermi energy range of interest, ensuring the stability of the complex against dissociation. However, application of the second criterion concerning the occurrence of defect complexes, leads to the conclusion that the formation of As_{Ga} defect prevails over the formation of the V_{As} - As_{Ga} defect complex.

V_{As}

The structure of V_{As} is illustrated in Fig. 3.6(a) for the neutral charge state. The tetrahedral symmetry of the site is preserved upon relaxation, which consists in an inwards displacement of the As atoms facing the vacancy into the vacancy site by 0.36 \AA . In the $+1$ and -1 charge states this symmetric displacement amounts to 0.19 and 0.50 \AA , respectively. The -1 charge state allows saturation of all the Ga DBs, satisfying the electron counting rule. Charge states 0 and $+1$ lack electrons. For completeness, we consider the bistable form of the V_{Ga} , which

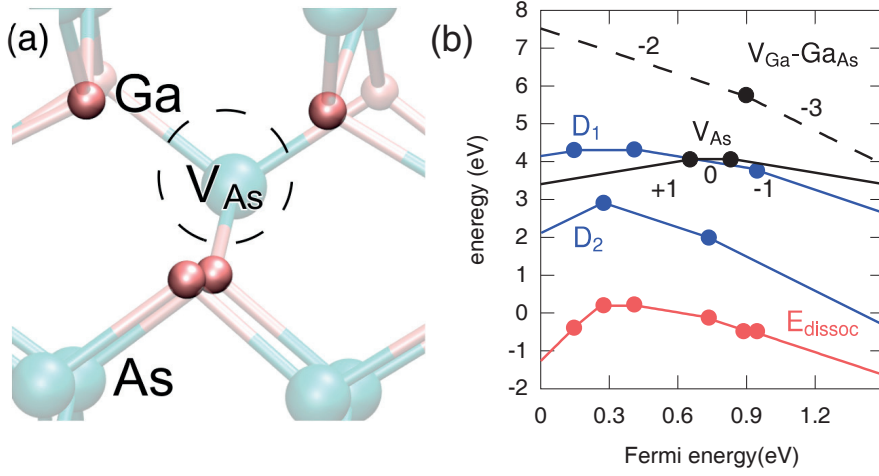


Figure 3.6 – V_{As} defect: (a) relaxed structure in the neutral charge state and (b) formation energies of the V_{As} defect (black continuous lines) and of its metastable $V_{Ga}-Ga_{As}$ form (black dashed lines).

consists in a Ga vacancy-antisite complex ($V_{Ga}-Ga_{As}$). In the charge state -3 , the relaxed structure shows the As atoms facing the Ga vacancy displaced towards the vacancy site by 0.38 \AA . The atom occupying the antisite moves towards the vacancy by 0.15 \AA , resulting in three equivalent Ga–Ga bonds of length 2.40 \AA . In the charge state -2 the structure further relaxes with the Ga_{As} atom displaced from the antisite site by 0.75 \AA .

Figure 3.6(b) shows the calculated formation energies of the V_{As} defect and of the $V_{Ga}-Ga_{As}$ defect complex as obtained for an As-rich environment (black lines). Applied finite-size corrections amount to 0.12 and 0.10 eV for the $+1$ and the -1 charge states, respectively. The As vacancy is stable in the charge states -1 , 0 , and $+1$, while the $V_{Ga}-Ga_{As}$ defect complex is found to occur in the charge states -2 and -3 . The formation energy of the isolated V_{As} defect falls between ~ 4 and $\sim 3 \text{ eV}$, while that of the $V_{Ga}-Ga_{As}$ defect complex ranges between ~ 8 and $\sim 4 \text{ eV}$. The V_{As} defect is more stable than the $V_{Ga}-Ga_{As}$ defect complex for all values of the Fermi energy, indicating that no bistability occurs in this case.

In order to investigate the stability of the $V_{Ga}-Ga_{As}$ defect complex, we consider the following dissociation reaction:



which gives isolated Ga_{As} (D_1) and V_{Ga} (D_2) as dissociation products. The dissociation energy is negative for most of the Fermi energies, revealing the unstable nature of the defect complex upon dissociation.

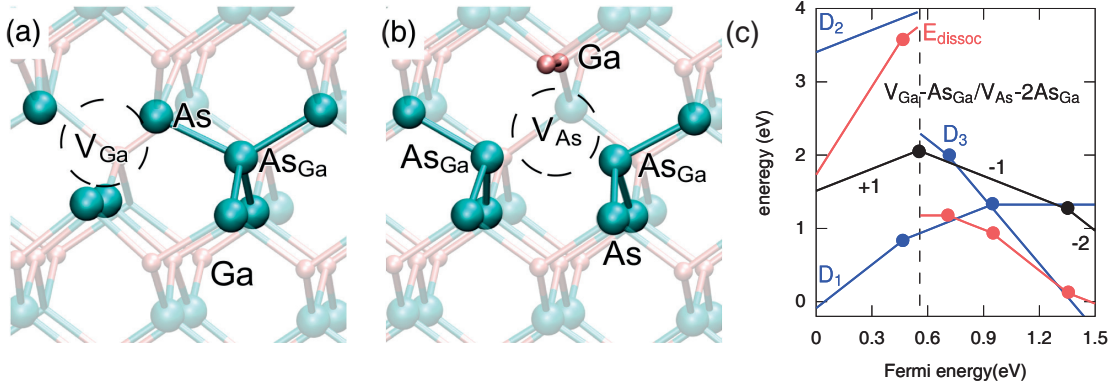


Figure 3.7 – $V_{Ga}-As_{Ga}/V_{As}-2As_{Ga}$ defect complex: relaxed structure in the charge states (a) -1 and (b) $+1$. (c) Formation (black lines) and binding (red lines) energies of the two defect complexes. In (c) the formation energies of the corresponding dissociation products (blue lines) are shown, As_{Ga} defect (D_1), V_{As} defect (D_2), and V_{Ga} defect (D_3).

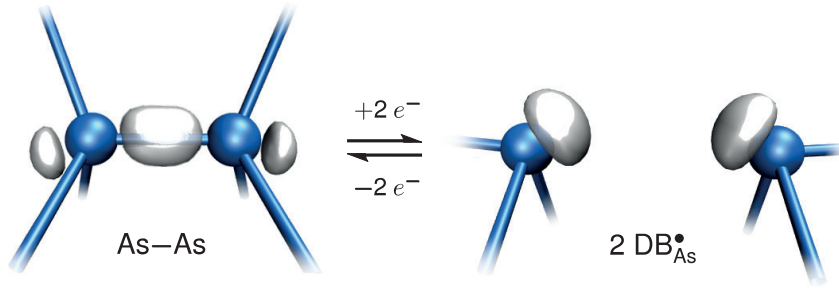


Figure 3.8 – Schematic representation of the forward and backward transformations between an As–As dimer (left) and two doubly occupied As dangling bonds ($2 DB_{As}^*$, right) upon the capture and release of two electrons ($2 e^-$).

$V_{Ga}-As_{Ga}/V_{As}-2As_{Ga}$ defect complex

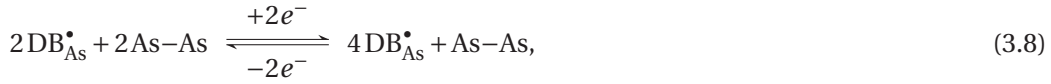
In search for a better agreement with the experiments involving radiation damage, we examine a defect not previously considered in the literature. We study a complex involving the two elemental defects with the lowest formation energies in an As-rich environment, namely V_{Ga} and As_{Ga} . This defect complex shows a bistability which is similar to that of V_{Ga} , but which involves an additional bound As_{Ga} defect on each side of the reaction:



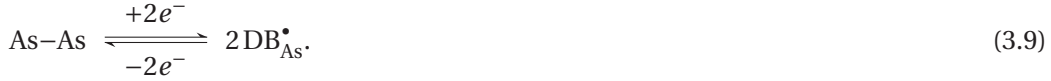
Upon O capture, the defect complex $V_{As}-2As_{Ga}$ transforms into a previously identified defect in GaAs:O [45] and can thus be seen as its precursor. Figures 3.7(a) and (b) illustrate the relaxed structures of the competing defect complexes in the charge states -1 and $+1$, respectively.

In the charge state -1 , the stable defect complex is the $V_{Ga}-As_{Ga}$. In the corresponding relaxed

structure, all the As atoms facing the Ga vacancy relax towards the vacancy as shown in Fig. 3.7(a). In particular, the As atom which bridges the Ga vacancy and the antisite As atom displaces by 0.34 Å, slightly more than the other As atoms, which move by 0.25 Å. The As_{Ga} gives rise to 4 As–As bonds with lengths of 2.48 ± 0.01 Å, the shortest of which involves the bridging As atom. The defect structure satisfy the electron counting rule. In the -2 charge state, the relaxed structure minimally differs from that observed in charge state -1 . The $\text{V}_{\text{As}}\text{-}2\text{As}_{\text{Ga}}$ defect structure is achieved by the hopping of the bridging As atom into the Ga vacancy thereby giving rise to the second As_{Ga} . In the charge state $+1$, the two Ga atoms facing the As vacancy reduce their distance from 4.00 Å in the bulk to 2.74 Å, stretching their Ga–As backbonds by 0.19 Å. The two antisite As atoms move toward the As vacancy by 0.24 Å and form As–As bonds with lengths of 2.51 Å. The structural transformation occurring with the capture of two electrons going from the $+1$ to the -1 charge state can be expressed according to:



which simplifies to give:



This reaction corresponds to the breaking of a homopolar As–As bond and to the formation of two As DBs, upon the capture of two electrons as shown in Fig. 3.8.

Figure 3.7(c) shows calculated formation energies of the defect complexes involved in this bistability (black lines). Finite-size corrections applied to the $+1$, -1 , and -2 defect charge states value 0.08, 0.16, and 0.59 eV, respectively. The calculated formation energies indicate that the defect is bistable. The vertical dashed-line in Fig. 3.7(c) indicates a Fermi-level position which separates the regime in which $\text{V}_{\text{As}}\text{-}2\text{As}_{\text{Ga}}$ is stable in positive charge states from the regime in which $\text{V}_{\text{Ga}}\text{-As}_{\text{Ga}}$ is stable in negative charge states. This amphoteric behavior leads to Fermi-level pinning around the $+1/-1$ charge transition level at 0.59 eV above the VBM, in excellent agreement with the experimental value measured for radiation damaged GaAs samples (0.6 eV) [127, 128]. We note that the charge state -2 shows an unpaired electron which is consistent with an As-antisite-related defect which has been detected in Ref. [31], and shows a paramagnetic level at less than 0.43 eV below the conduction band edge. However, several As-antisite-related defects with hyperfine patterns similar to EL2 have been detected in GaAs [178] and a more detailed assignment would thus require the calculation of hyperfine parameters.

For examining the stability of the present defect complexes, we consider the following dissociation reactions:



Eq. (3.10) refers to the positive charge state of the present defect, being stable for Fermi energies below $\text{VBM} + 0.59$ eV. This complex dissociates into two As antisites (D_1) and an As vacancy (D_2). The calculated dissociation energy is positive indicating the overall stability

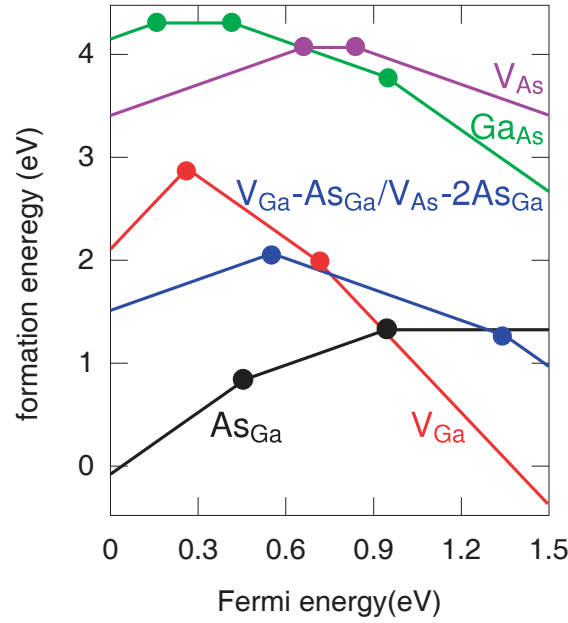


Figure 3.9 – Formation energy vs Fermi energy for the As_{Ga} defect (black), the Ga_{As} defect (green), the V_{Ga} defect (red), the V_{As} defect (violet), and the $V_{Ga}-As_{Ga}/V_{As}-2As_{Ga}$ bistable defect complex (blue). As-rich conditions are assumed.

of the $V_{As}-2As_{Ga}$ defect complex against dissociation. However, the formation energy of the isolated As_{Ga} defect is smaller and thus dominates over that of this defect complex. Eq. (3.11) refers the negative charge states of the present defect, being stable for Fermi energies above VBM+0.59 eV. This complex dissociates into an As antisite (D_1) and a Ga vacancy (D_3). The calculated binding energy is positive for all Fermi energies indicating stability of the defect complex against dissociation. However, the isolated As_{Ga} and V_{Ga} defects have lower formation energies in the midgap region and close to the CBM, respectively. This suggests that the concentration of the present defect complex does not dominate in thermal equilibrium conditions over its dissociation products. However, since radiation-damaged samples are generally not at thermal equilibrium, we propose the $V_{Ga}-As_{Ga}-V_{As}-2As_{Ga}$ defect complex to be at the origin of the observed Fermi-level pinning in radiation-damaged GaAs samples.

Conclusion

In Fig. 3.9 we summarize the formation energies of the stable intrinsic defects considered in this Chapter. The most stable defects are the As_{Ga} and V_{Ga} . The former is a double donor defect and is particularly stable in p -type conditions, the latter is an acceptor defect and is particularly stable in n -type conditions. The V_{Ga} defect transforms into the donor $V_{As}-As_{Ga}$ defect complex, leading to amphoteric behavior which can pin the Fermi-level at ~ 0.3 eV above VBM. We note that the initial results by Baraff and coworkers correctly pointed out the bistability of this defect but their calculated charge transition level between negative and positive charge states suffered from the band-gap deficiency of the local density approximation [129, 130].

Chapter 3. Intrinsic defects in bulk GaAs

The $V_{\text{Ga}}\text{-As}_{\text{Ga}}/V_{\text{As}}\text{-}2\text{As}_{\text{Ga}}$ bistable defect complex also shows low formation energies ranging between ~ 1 and ~ 2 eV. The bistability shown by this defect relies on the transformation of an As–As bond into two As DBs, and accounts for Fermi-level pinning at ~ 0.6 eV above VBM through an amphoteric mechanism. We emphasize that the amphoteric behavior of this defect supports the mechanism for Fermi-level pinning originally proposed by Walukiewicz as responsible for the experimental observations [127, 128]. Finally, Ga_{As} and V_{As} have formation energies ranging between ~ 3 and ~ 4.5 eV, indicating that their formation is unfavored.

4 Oxygen defects in bulk GaAs

In this Chapter, we study structural and electrical properties of O-defects in GaAs. O-doped GaAs is technological relevant because of its SI behavior. A large experimental characterization is available for the most relevant O-defect in GaAs [31, 33, 34, 34, 35, 36, 37, 38, 39, 40]. LVM experiments show an absorption peak at 845 cm^{-1} , associated to an interstitial bridging oxygen atom (O_b) [35], and a family of three bands, located at 730.7 cm^{-1} , 714.9 cm^{-1} and 714.2 cm^{-1} and labeled *A*, *B*, and *B'* [35, 37, 38]. This family of LVM bands share many properties and correspond to different charge states of the same defect [37, 38]. This defect has a Ga–O–Ga structure, with two stable charge states (+1 and –1), a metastable, paramagnetic, and neutral state, and is responsible for Fermi-level pinning $\sim 0.4\text{ eV}$ below CBM [31, 33, 34, 34, 36, 37, 38, 39, 40]. Finally optical transition between its stable charge states have been measured and correspond to 1.37 and 0.65 eV [33]. Despite, the efforts of the theoretical community the atomic structure of this O-defect is still uncertain as a good agreement with the experimental characterization is missing [41, 42, 43, 44, 45]

Here, we study a set of O-defects including bridging O atom in a As–O–Ga configuration, interstitial O atoms in tetrahedral sites, and O atoms substitutional to both Ga (O_{Ga}) and As atoms (O_{As}). In addition, we consider an As vacancy containing two O atoms, and defect complexes involving an O_{As} defect bound to either one or two As_{Ga} antisites, denoted $\text{As}_{\text{Ga}}\text{-O}_{\text{As}}$ and $(\text{As}_{\text{Ga}})_2\text{-O}_{\text{As}}$, respectively. Upon examination of the actual occurrence of O-defect through the application of two stability criteria, we conclude that only the bridging O defect and the $(\text{As}_{\text{Ga}})_2\text{-O}_{\text{As}}$ complex are expected to occur. The nearest neighbor environment, the Fermi-level pinning position, and the optical transition energies between charge states of the latter defect are in excellent agreement with experiment. Part of these results can be found in peer-reviewed article [179, 180].

Computational Details

The defects are generally studied in 64-atom supercells although for particular purposes, we carry out a few calculations using larger supercells containing 216 and 512 atoms. For relax the atomic structures we use the PBE functional while the electronic structure is relaxed through the HSE functional setting the parameters to the values described in Chapter 2 We use a translated $2\times 2\times 2$ **k**-mesh following Refs. [123, 160].

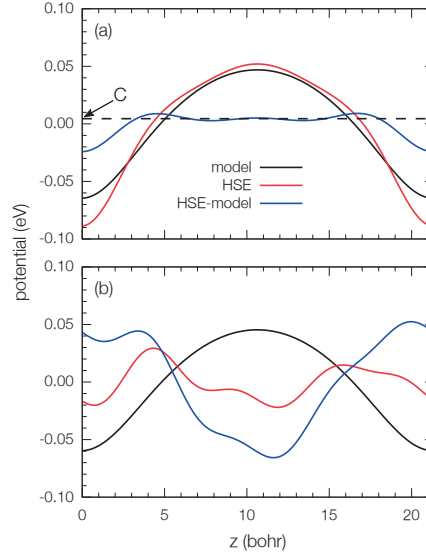


Figure 4.1 – Planar averages of the electrostatic potential of (a) the O_{As} defect (Sec. 4) and of (b) the O_i-Ga_4 defect (Sec. 4), both in the charge state -1 , as obtained in HSE calculations (red). The defect is located at the origin. The black lines correspond to the potential of a model Gaussian charge distribution with a width of 1 bohr (model). The blue lines represent the short-range defect potential and are obtained from the difference between the red and the black lines.

Assessing the localization of defect charge densities

The well localized behavior of defect charge densities can be assessed through the finite size correction scheme (described in Sec. 2.5). Indeed, the planar average of the short-range electrostatic potential far from the defect tends to a constant value if the defect charge is well localized [170]. When the defect state is localized within the supercell, the planar average of the HSE electrostatic potential is well reproduced by that of a model Gaussian charge distribution, as shown in Fig. 4.1(a). The width of the Gaussian used in this work is 1 bohr, and we verify that the correction to the energy is marginally sensitive to this parameter¹. The experimental value of 13.1 is considered for the static dielectric constant for GaAs [181]. The difference between the HSE and the model potentials gives the defect short range potential, which shows a flat behavior far away from the defect site [170]. The constant value C which is added to the short-range potential in order to make it vanish between two defects, corresponds to the alignment term ($\Delta_{q/0}$) of the finite-size correction. For illustration, we show in Fig. 4.1(b) a case in which the defect charge is not well localized. In this case, the difference between the HSE and the model potential is no longer short range and strongly oscillates far from the defect site. In some cases, these electrostatic considerations might not be sufficient to determine whether the defect state is well localized within the adopted supercell. The calculation of the screening charge is then a better indicator of the defect charge localization [152].

¹For instance the variation of the Gaussian width from 1 bohr to 5 bohr affects the calculated finite-size correction energy by less than 25 meV

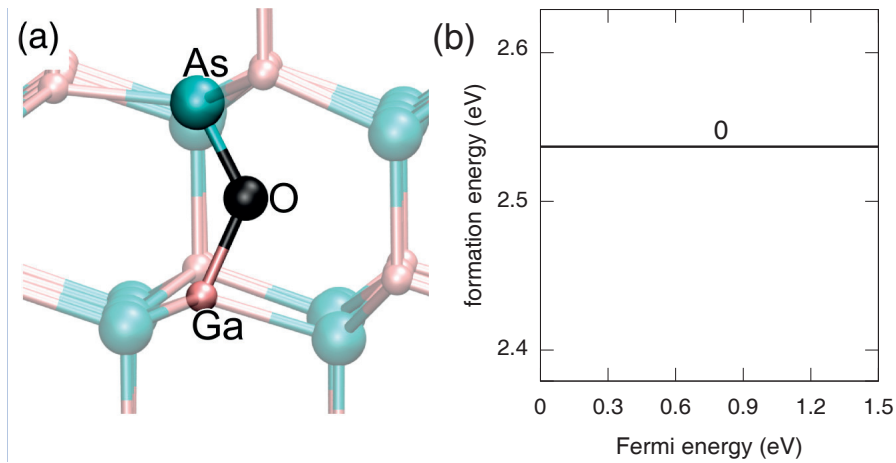


Figure 4.2 – O_b defect, in which the O atom occupies a bridging interstitial site: (a) relaxed structure and (b) formation energy vs Fermi energy.

Criteria for the occurrence of defect complexes

The same criteria for stability and actual occurrence of defect complexes described in Chapter 3 are applied, after some considerations, also to the present case of O-defects in GaAs. Non-interstitial O defects can also be considered as complex defects (DO) corresponding to an unoxidized intrinsic defect (D) in which an O atom has been captured. In this case, the simplest examples are O substitutional defects which can be pictured as O atoms captured in vacancies. To apply the first criterion we take the most stable interstitial O defect as the dissociation product defect which contains an O atom. This defect corresponds to the O_b occupying a bridging As–O–Ga configuration. As far as the second criteria is concerned, we assume that the global concentration of oxygen is fixed by external doping conditions leading to the necessity to compare the formation energy of the complex $E_f(DO)$ only with that of the most stable interstitial O-defect $E_f(O_b)$.

O_b

In the bridging interstitial defect O_b , the O atom binds to an As atom and a Ga atom of the regular GaAs network, as shown in Fig. 4.2(a). In the relaxed structure, the As–O and Ga–O bond lengths are 1.81 and 1.83 Å, respectively, while the As–O–Ga bond angle takes the value of 129° , in good agreement with previous theoretical studies [42, 43]. In this stable defect configuration, one As atom in the second-neighbor shell of the O atom belongs to the plane defined by the As–O–Ga unit. During a complete rotation around the axis of the original Ga–As bond, three equivalent defect configurations are found. Through nudged elastic band calculations with 12 images and one climbing image [157], we find that the energy barrier between two equivalent minima amounts to ~ 15 meV. The transition state occurs when the As–O–Ga plane contains a second-neighbor Ga atom.

The O_b defect configuration is only stable in its neutral charge state, in agreement with

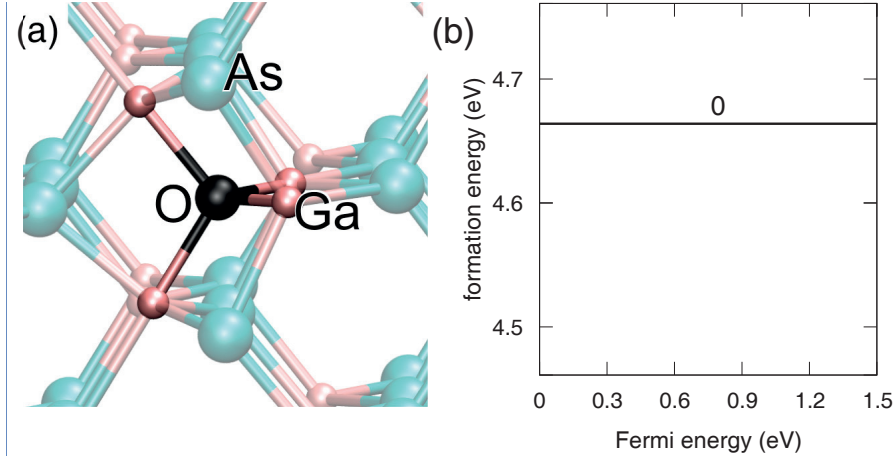


Figure 4.3 – Interstitial O_i -Ga₄ defect: (a) relaxed structure and (b) formation energy vs Fermi energy.

experimental evidence [36] and a previous calculation [42]. The formation energy calculated at the HSE level is 2.54 eV, as shown in Fig. 4.2(b), and corresponds to the lowest value among the interstitial defects considered in this work. For this reason, the O_b defect is taken as reference in the application of the criteria proposed at the beginning of the present section.

For completeness, we also investigate the bridging configuration proposed by Taguchi and Kageshima [44] and indeed find an equilibrium configuration. However, the identified structure does not correspond to a local minimum and readily relaxes towards that of the O_b defect upon a small displacement of the O atom. We remark that this equilibrium configuration corresponds to the symmetrical transition state for diffusion jumps between nearby O_b configurations, similarly to the Y configuration for O diffusion in silicon [182, 183].

O_i -Ga₄ and O_i -As₄

The zincblende structure of GaAs presents two tetrahedral interstitial sites in which interstitial oxygen (O_i) can be incorporated, one enclosed by four As atoms (O_i -As₄) and one by four Ga atoms (O_i -Ga₄). By carrying out structural relaxations of the O_i -As₄ defect in a 216-atom supercell, we find that the O_i -As₄ defect is unstable and relaxes without any barriers to O_i -Ga₄ defect structure. This spontaneous transition is not observed in the 64-atom supercell, as this cell is too small to describe the important deformations undergone by the GaAs network upon the hopping of the O atom from one interstitial site to the other. We note that the higher stability of the O_i -Ga₄ site can be rationalized through electrostatic arguments.

In the O_i -Ga₄ defect, the O atom is located at the tetrahedral site and forms four equivalent O-Ga bonds with bond lengths of 2.05 Å and four Ga-O-Ga angles of 109°, as shown in Fig. 4.3(a). This structure agrees well with previous semilocal calculations [43]. Our hybrid functional calculations indicate that only the neutral charge state is stable. In particular, the negatively charged states (from -1 to -3) do not give rise to localized charge states, as can

be inferred from the behavior of the electrostatic potential calculated upon the addition of electrons shown in Fig. 4.1(b). This assessment is at variance with previous studies, in which the charge localization was not considered as a criterion for defining the stability of a given charge state [43]. The defect formation energy calculated with the HSE hybrid functional is 4.66 eV, as shown in Fig. 4.3(b). By comparing the formation energy of the present defect with that of the O_b defect, we find a difference of more than ~ 2 eV, which clearly disfavors the incorporation of oxygen in the tetrahedral O_i -Ga₄ configuration.

O_{As}

The O_{As} defect was initially assumed as origin of the experimentally identified Ga-O-Ga structure, mostly because of the analogy with the VO center in silicon [35]. This assignment was supported by semilocal density functional calculations [41]. The O was found to occupy an off-center position and to bind two Ga atoms [41]. Moreover, the charge state -2 was found to be metastable in agreement with the observation of metastability associated with the B' band in the LVM spectra [41]. These results were confirmed in later studies, which located the $-1/-3$ charge transition level at ~ 0.5 eV below the CBM under the assumption that the calculated valence band edge could be aligned to the experimental one [42, 43].

Table 4.1 – Bond lengths (Å) and bond angles of relaxed structures of the O_{As} defect in various charge states. The Ga atoms are labeled according to Fig. 4.4.

Charge state	+1	0	-1	-2	-3
Symmetry	T_d	T_d	C_{2v}	C_{2v}	C_{2v}
bond angle					
Ga ¹ -O-Ga ¹	109.5°	109.5°	131.0°	130.5°	134.6°
Ga ² -O-Ga ²	109.5°	109.5°	67.4°	64.6°	63.2°
bond length (Å)					
O-Ga ¹	2.17	2.14	1.87	1.90	1.88
O-Ga ²	2.17	2.14	2.58	2.45	2.47
Ga ² -Ga ²	3.55	3.49	2.87	2.61	2.58

In the charge state +1, the O atom occupies the highly symmetric T_d position, as shown in Fig. 4.4(a). The four Ga atoms relax towards the central O atom by 0.58 Å, forming Ga-O bonds of 2.17 Å. Detailed structural properties such as bond lengths and bond angles are given in Table 4.1. The charge density of the highest occupied state is found to correspond to a delocalized state of the valence band [Fig. 4.4(a)]. This structure is consistent with electron counting arguments. In fact, every Ga dangling bond pointing towards the As vacancy may be thought as contributing $\frac{3}{4}$ electrons while the O atom in the charge state +1 brings 5 electrons. This results precisely in 8 electrons which account for the four Ga-O bonds. In the neutral charge state, the O atom still occupies a position of T_d symmetry [Fig. 4.4(b)]. The Ga-O bond lengths do not vary in an appreciable manner (Table 4.1). Inspection of the charge density of the highest occupied state reveals that the charge is localized in a spherically symmetric

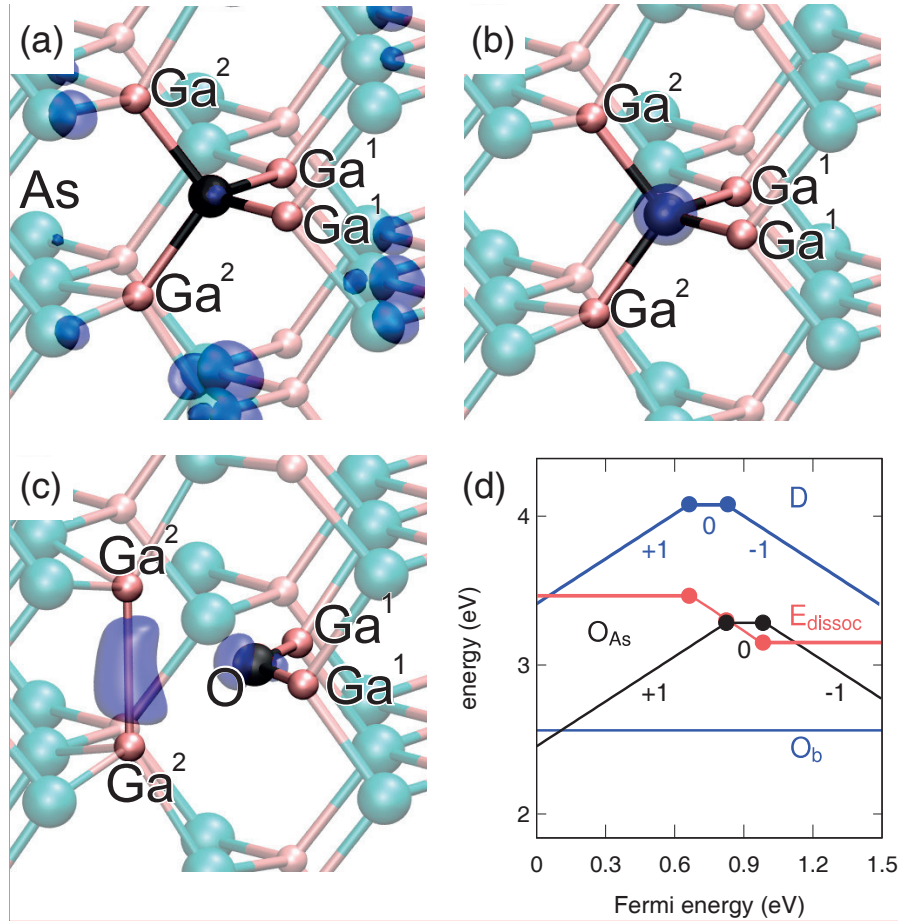


Figure 4.4 – O_{As} defect: relaxed structure in the charge states (a) +1, (b) 0, and (c) –1. The O atom occupies a tetrahedral (T_d) site in the positive and neutral charge states, but relaxes to a position of C_{2v} symmetry with only two Ga neighbors in the negative charge state. The charge density of the highest occupied state is shown in transparency. (d) formation (black) and dissociation (red) energies vs Fermi energy. In (d), we also show the formation energies of the dissociation products (blue), the V_{As} defect (D) and the O_b defect.

orbital on the O atom, which preserves the T_d symmetry of the defect structure. The $+/-0$ transition thus corresponds to charging and discharging this localized orbital, thereby only marginally affecting the atomic structure of the defect. In the charge state –1, one obtains a defect structure with localized charge upon the relaxation of the O atom to a position of lower symmetry (C_{2v}), as shown in Fig. 4.4(c). The O atom becomes twofold coordinated with Ga (Ga^1) showing Ga-O bond lengths of 1.87 Å, noticeably shorter than found for the symmetric T_d position in the neutral and singly positive charge states (cf. Table 4.1). The other two Ga atoms (Ga^2) which are no longer bonded to O move closer to each other and form a Ga-Ga bond of 2.87 Å. This bond formation implies a displacement of the Ga^2 atoms by 0.62 Å with respect to the neutral charge state and by 1.15 Å with respect to the pristine bulk. The charge density of the highest occupied orbital is localized [as evinced by the behaviors of electrostatic potential in Fig. 4.1(a)] and corresponds to the bonding state of the covalent Ga–Ga bond [Fig.

4.4(c)]. This defect structure is also consistent with the electron counting condition. Since the two Ga^1 atoms bring only $\frac{3}{4}$ electrons each, the saturation of the Ga–O–Ga structure requires the addition of $\frac{1}{2}$ electron. Similarly, the two Ga^2 atoms require the addition of $\frac{1}{2}$ electron to form a doubly occupied Ga–Ga bonding state. In the charge state -1 , the missing electron is precisely provided. We also considered defect structures of higher negative charge (-2 and -3). In these charge states, the defect structure is not found to undergo major modifications with respect to the singly negative charge state (Table 4.1). However, the charge density of the highest occupied states are found to be delocalized over the simulation cell, hinting at the possibility that the defect is unable to localize such high levels of negative charge.

The formation energies of the charge states $+1$, 0 , and -1 of the O_{As} defect are shown in Fig. 4.4(b). The finite-size corrections applied to the formation energies of charge states $+1$ and -1 amount to 0.12 and 0.15 eV, respectively. The calculated $+1/0$, and $0/-1$ charge transition levels lie at 0.82 and 0.99 eV above the VBM, respectively. The stability of both positive and negative charge states indicates that the defect is amphoteric supporting Fermi-level pinning at ~ 0.9 eV above VBM [127], in satisfactory agreement with the experimental pinning level at ~ 1.1 eV above the VBM [33]. However, the present defect does not show negative- U behavior neither a stable Ga–O–Ga structural unit in all three charge states, as observed in experiment [37]. Therefore, the O_{As} defect cannot account for the experimental characterization of the Ga–O–Ga defect.

For determining the dissociation energy, we consider the dissociation of the O_{As} defect into the isolated V_{As} defect and the O_{b} defect, according to



The formation energy of the V_{As} defect (D) is taken from the previous section as it has been calculated at the same level of theory at which we here investigate the O defects and is shown in Fig. 4.4(b) together with the formation energy of the O_{b} defect. The dissociation energy is then obtained from the difference between the formation energy of the O_{As} defect and the sum of the formation energies of the dissociation products according to Eq. (3.1). For the O_{As} defect, the dissociation energy assumes positive values for all Fermi energies in the band gap [Fig. 4.4(b)], indicating that the defect is stable against dissociation (first criterion in Sec. 3). However, the second criterion is not satisfied. Indeed, the formation energy of the O_{As} defect is higher than that of the O_{b} defect for all Fermi energies in the band gap, but a small range close to the VBM. Hence, despite its stability against dissociation, the O_{As} defect is unlikely to play a relevant role in GaAs:O.

The present electrical properties of the O_{As} defect obtained at the HSE level differ from the semilocal functional results reported previously [42, 43]. In Fig. 4.5 the formation energies for an As-rich environment as obtained within various theoretical schemes are reported as a function of the Fermi energy. We first focus on formation energies calculated at the PBE level of theory neglecting finite-size corrections and only applying the potential alignment procedure (cf. PBE PA in Fig. 4.5). Applying the scissor-operator as used in previous works [42, 43], we take the calculated VBM as it is and we shift the CBM to reproduce the experimental band gap. We find that the charge states $+1$, -1 , -2 , and -3 are stable, reproducing previous results [42, 43]. However, the charge state -2 is only stable within a very narrow range of Fermi energies (0.01

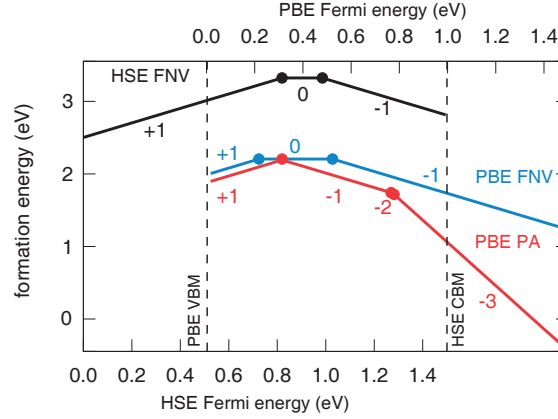


Figure 4.5 – Formation energy of the O_{As} defect in As rich conditions as a function of the Fermi energy, as calculated with the hybrid (HSE) functional (black) including FNV finite-size corrections. Corresponding values of the Fermi energy are read on the lower horizontal axis, where the energies are referred to VBM in the HSE calculation. Formation energies calculated with the semilocal (PBE) functional are also given, with (blue) and without (red) FNV finite-size corrections. The Fermi energy as defined with respect to the VBM in the PBE calculation can be read on the the upper horizontal axis. The alignment of the HSE and PBE energy scales is achieved through the average electrostatic potential in bulk GaAs.

eV) and its stability can thus not conclusively be ascertained with the accuracy of the present calculations. Similarly, the neutral charge state is found to be metastable, but its stability cannot be excluded on the basis of the present accuracy. This theoretical description appears consistent with the experimental characterization. The main features of the experimental LVM spectra are well reproduced, since three charge states (-1 , -2 , and -3) involve a Ga-O-Ga structure, among which the charge state -2 could represent the metastable one. However, the position of the $-1/-3$ charge transition level in our calculation occurs at 0.7 eV below the CBM, slightly deeper in the band gap than that found previously within the local density approximation (0.5 eV below the CBM) [42, 43]. As the experimental Fermi-level pinning occurs at 0.4 eV below the CBM [31, 33], the present results indicate that the present alignment at the PBE level has weakened the agreement of the O_{As} defect with experiment.

The agreement with experiment deteriorates further when considering finite-size corrections to the calculation of the formation energy (Eq. 2.7). Application of the FNV corrections to the semilocal PBE results considerably modifies the stable defect charge states within the band gap (cf. PBE FNV in Fig. 4.5). Furthermore, we use this correction scheme to verify the localized nature of the defect charge. The analysis of the -2 and -3 charge states of the O_{As} defect show delocalized behavior, similarly to those reported in Fig. 4.1(b). The consideration of finite-size corrections destabilize the -1 and $+1$ charge states removing the negative- U behavior associated with the neutral charge state. Thus, the novel picture that arises from finite-size corrected PBE results shows stability for just three charge states, among which only one accounts for the experimentally identified Ga-O-Ga local structure. Furthermore, the O_{As} defect lacks other experimental signatures, such as the occurrence of a metastable charge state (negative- U behavior) and a charge transition level causing Fermi-level pinning in the

upper part of the band gap. These observations shed further doubts on the assignment of the experimentally observed O defect to the O_{As} center.

As a further improvement, we evaluate the defect electronic structures through hybrid functional calculations which directly reproduce the experimental band gap without the need of a scissor operator and which have been shown to give accurate defect energy levels with respect to the band edges [160]. The corresponding formation energies (cf. HSE in Fig. 4.5) are qualitatively similar to those calculated with the semilocal functional. In particular, the charge transition levels calculated in PBE and HSE correspond within 0.1 eV when the electronic structures are aligned through the electrostatic potential (Fig. 4.5), in accord with a general property of atomically localized defects [149, 150, 151, 158]. For all charge states, the charge localization is confirmed through the inspection of the electrostatic potential, similarly to Fig. 4.1(a). For completeness, we also carry out a structural relaxation of the charge state -2 at the HSE level and confirm that its properties are inconsistent with a localized charge state [152].

Table 4.2 – Formation energies of the substitutional O_{As} and O_{Ga} defects in various charge states, as obtained with the HSE hybrid functional for p -type and n -type GaAs, in both As-rich and Ga-rich conditions. Energies are in eV.

Charge	Condition	O_{As}		O_{Ga}	
		p -type	n -type	p -type	n -type
-1	Ga-rich	3.92	2.39	8.82	7.29
	As-rich	4.30	2.77	6.92	5.39
0	Ga-rich	2.93	2.93	7.82	7.82
	As-rich	3.31	3.31	5.92	5.92
+1	Ga-rich	2.11	3.64	7.40	8.93
	As-rich	2.49	4.02	5.50	7.03

For reference, we report in Table 4.2 the defect formation energies for Fermi energies at the VBM (p -type) and at the CBM (n -type), calculated in both As-rich and Ga-rich conditions. When Ga-rich conditions are assumed, μ_{Ga} is taken from bulk Ga in the solid orthorhombic phase, whereas μ_{As} and μ_O result from the equilibrium conditions of GaAs and β -Ga₂O₃, respectively. When changing the atomic chemical potentials taken as reference, the defect formation energies undergo a rigid shift without affecting the positions of charge transition levels.

O_{Ga}

In the O_{Ga} defect, the O atom is centrally located in the Ga vacancy, where it forms four equivalent O–As bonds with lengths of 2.26 Å and four As–O–As angles of 109°. This atomic structure does not undergo significant variations upon charging.

Stable charge states are the singly positive, the neutral, and the singly negative charge states. In the As-rich condition, the formation energy of this defect varies between 5.39 eV and 5.92 eV, which make its formation unfavorable. Due to this high formation energy, it is clear that the second criterion for defect occurrence is by far not satisfied. Therefore, we refrain from

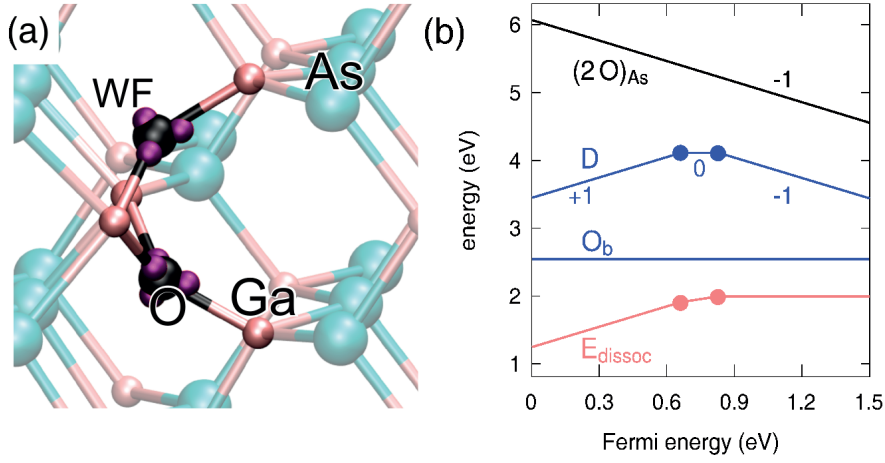


Figure 4.6 – $(2O)_{As}$ defect: (a) relaxed structure of the most stable configuration in the charge state -1 , and (b) formation (black) and dissociation (red) energies vs Fermi energy. In (a), the centers of relevant maximally localized Wannier functions are illustrated through small violet spheres. In (b), we also show the formation energies of the dissociation products (blue), the V_{As} defect (D) and the O_b defect.

graphically illustrating the calculated formation and dissociation energies. Calculated defect formation energies for various conditions are summarized in Table 4.2. From the comparison between the formation energies of the two substitutional defects, O_{As} and O_{Ga} , we infer that the former defect is energetically preferred.

$(2O)_{As}$

In order to saturate all the Ga dangling bonds facing an As vacancy, it is natural to consider two O atoms leading to the $(2O)_{As}$ defect. The electron counting rule suggests that two twofold coordinated O atoms could saturate the exposed Ga dangling bonds in the charge state -1 . However, upon direct relaxation in this charge state, we obtain two threefold coordinated O atoms, with one of the O atoms having moved to a nearby interstitial site.

In order to explore the configurational space available to the two O atoms, we carry out molecular dynamics simulations. We perform runs of 5 ps in both the neutral and -1 charge states at three different temperatures (300, 500, and 800 K). In addition to the structure found by direct relaxation, the molecular dynamics simulations identify a second structure, in which the O atoms are also threefold coordinated with Ga.

In the second configuration, only the Ga atoms facing the vacancy participate to the bonding, giving two fourfold and two fivefold coordinated Ga atoms, as shown in Fig. 4.6(a). Each O atom forms one short bond with a fourfold coordinated Ga atom (1.88 Å) and two long bonds with the two fivefold coordinated Ga atoms (2.00 Å). Oxygen bond angles are 125° in Ga-O-Ga units involving one fourfold and one fivefold coordinated Ga atom, and 94° in Ga-O-Ga units involving two fivefold coordinated Ga atoms.

To rationalize the electronic behavior of these defect structures, we adopt an analysis based on maximally localized Wannier functions (WF), which allow for a real-space representation of the electron localization [184]. In both $(2\text{O})_{\text{As}}$ defect structures, the O atoms are surrounded by four WF centers, three of which point towards a Ga atom and correspond to Ga–O bonds, as shown in Fig. 4.6(a). The forth WF center lies closer to the O atom and corresponds to a lone pair. Application of the electron counting rule reveals that both $(2\text{O})_{\text{As}}$ defect structures require one extra electron in order to doubly occupy all the bonds. Indeed, the Kohn-Sham energy of the Ga–O bonds are deep in the valence band and the only stable defect state is the charge state -1 .

For the determination of defect formation energies, we realize that the 64-atom supercell is too small to observe complete screening of the defect charge as expected for localized defect states [152]. To ensure proper screening behavior, we thus use 512-atom supercells with the sole Γ point. This \mathbf{k} -point sampling is equivalent to that used for the other oxygen-related defects, thereby allowing direct comparisons of formation energies. The defect configuration identified by molecular dynamics is the most stable one for the $(2\text{O})_{\text{As}}$. Its formation energy is displayed in Fig. 4.6(b). The applied finite-size correction is 0.09 eV. The structure achieved by direct relaxation lies 0.45 eV higher in energy. We note that, with respect to the O_{As} defect, the electrical properties undergo significant variation upon the capture of a second O atom. The amphoteric nature of the O_{As} defect disappears and the -1 charge state is the only stable defect state.

We obtain the dissociation energy [cf. Fig. 4.6(b)] by taking the isolated V_{As} defect (D) and two O_{b} defects as dissociation products, according to



The dissociation energy is found to be positive, indicating that the $(2\text{O})_{\text{As}}$ defect is stable against dissociation for all values of the Fermi energy. However, the application of the second criterion for the relevance of the $(2\text{O})_{\text{As}}$ defect indicates that it does not prevail over the formation of isolated V_{As} and 2O_{b} defects [cf. Fig. 4.6(b)].

For completeness, we also consider the dissociation channel by which the $(2\text{O})_{\text{As}}$ defect transforms to the isolated O_{As} and O_{b} defects. In this case, the calculated dissociation energy is positive only for Fermi energy above $\text{VBM}+0.5$ eV in the band gap, indicating defect instability upon the release of a single O atom in p -type conditions. Furthermore, in consideration of the second criterion, one infers that the O_{As} defect is present in higher concentrations than the $(2\text{O})_{\text{As}}$ defect, since the formation energy of the former ranges between 2 and 3 eV [cf. Fig. 4.4(b)], while that of the latter is higher than ~ 4 eV [Fig. 4.6(b)].

$\text{As}_{\text{Ga}}\text{-O}_{\text{As}}$

We consider the $\text{As}_{\text{Ga}}\text{-O}_{\text{As}}$ defect complex which consists of an O_{As} defect bound to an As_{Ga} antisite defect in its first-neighbor shell. In the charge state $+1$, the O atom binds to three Ga atoms facing the arsenic vacancy V_{As} and forms three equivalent bonds with lengths of 1.98 Å [Fig. 4.7(a)]. The As atom in the antisite position forms three equivalent As–As bonds with lengths of 2.50 Å, leading to a global structure of $\text{C}_{3\text{v}}$ symmetry. This As atom carries a

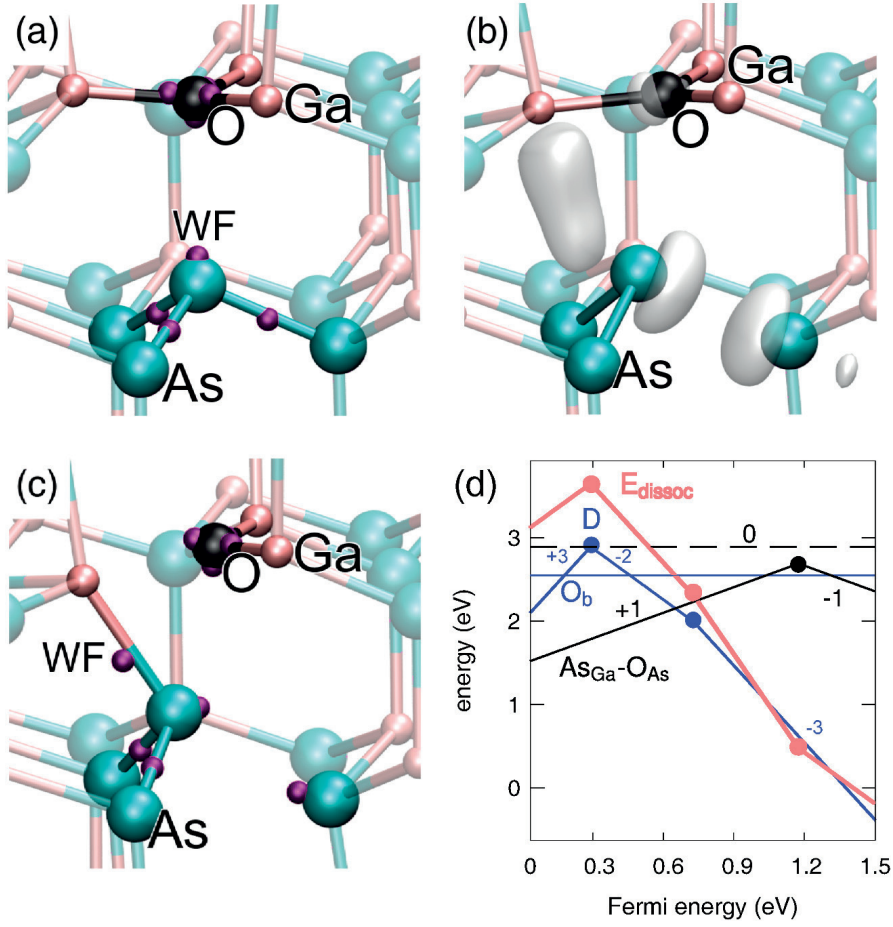


Figure 4.7 – $\text{As}_{\text{Ga}}\text{-O}_{\text{As}}$ defect: (a) relaxed structure in the charge state +1, (b) relaxed structure in the metastable neutral charge state with the density of the unpaired electron in transparency, (c) relaxed structure in the charge state -1, and (d) formation (black) and dissociation (red) energies vs Fermi energy. The small violet spheres in (a) and (c) indicate the center of the relevant maximally localized Wannier functions. In (d), we also show the formation energies of the dissociation products (blue), the unoxidized bistable $V_{\text{Ga}}/V_{\text{As}}\text{-As}_{\text{Ga}}$ defect complex (D) and the O_{b} defect.

lone pair, as confirmed through the calculation of maximally localized Wannier functions [Fig. 4.7(a)]. The electron counting rule is satisfied and all bonds are doubly occupied.

In the neutral charge state, the extra electron breaks the C_{3v} symmetry. Two of the O–Ga bonds shorten and one of the As–As bonds elongates, as shown in Fig. 4.7(b). Application of the electron counting rule implies a paramagnetic defect state with an unpaired electron, of which the charge density is illustrated in Fig. 4.7(b). This charge density shows antibonding character over the elongated As–As bond and bonding character between the antisite As atom and a nearby a Ga atom.

In the charge state -1, the addition of an electron drives the defect structure towards a closed-

shell configuration which satisfies the electron counting rule [cf. Fig. 4.7(c)]. The analysis through WF centers reveals that the O atom is twofold coordinated (with two O–Ga bond lengths of 1.91 Å) and that the antisite As atom binds to two As atoms and one Ga atom. The breaking of the As–As bond leaves oppositely-oriented lone pairs on the two As atoms [Fig. 4.7(c)].

The charge states +1 and –1 of the present defect are stable, while the neutral charge state is metastable, as can be seen from the defect formation energies reported in Fig. 4.7(d). Calculated finite-size corrections amount to 0.10 and 0.13 eV for charge states +1 and –1, respectively. The $\text{As}_{\text{Ga}}\text{-O}_{\text{As}}$ defect shows amphoteric character and a charge transition level at 1.16 eV above the VBM, in good agreement with the energy at which the Fermi level is pinned experimentally [31,33]. The number and type of stable charge states, the paramagnetic character of the neutral charge state, and its metastable nature all agree with experimental observations for the Ga–O–Ga defect. [34, 36, 37, 38, 39] However, the Ga–O–Ga core structure only occurs in the charge state –1 and transforms into a symmetrical O–Ga₃ structure in the charge state +1. This structural rearrangement disagrees with the experimental evidence that the Ga–O–Ga core persists in all three charge states [37, 38]. We remark that the mechanism by which the $\text{As}_{\text{Ga}}\text{-O}_{\text{As}}$ defect complex captures and releases two electrons is analogous to that observed for the $\text{V}_{\text{Ga}}\text{-As}_{\text{Ga}}/\text{V}_{\text{As}}\text{-2 As}_{\text{Ga}}$ defect complex, which we suggest to underlie the Fermi-level pinning in radiation damaged GaAs (cf. Chapter 3).

The stability of the $\text{As}_{\text{Ga}}\text{-O}_{\text{As}}$ defect complex can be examined by comparing its formation energy with those of its dissociation products, the isolated gallium vacancy V_{Ga} and the isolated O_{b} , according to the reaction:



In this decomposition, it should be accounted for that one of the dissociation products, the Ga vacancy, occurs in different structures depending on Fermi energy. The dissociation energy of the $\text{As}_{\text{Ga}}\text{-O}_{\text{As}}$ complex shows positive values exceeding 3 eV in *p*-type condition [cf. Fig. 4.7(d)].² However, the dissociation energy decreases with Fermi energy, reaching negative values in *n*-type condition. Hence, the stability criterion for the $\text{As}_{\text{Ga}}\text{-O}_{\text{As}}$ complex is fulfilled over almost the entire band gap, with the sole exception of a small energy region in the vicinity of the conduction band.

Under O doping conditions, to fulfill the second criterion for defect occurrence, the formation energy of the $\text{As}_{\text{Ga}}\text{-O}_{\text{As}}$ defect should be lower than that of the O_{b} defect [Fig. 4.7(d)]. This is indeed the case for all Fermi energies in the band gap, except for a small range around the defect charge transition level at 1.16 eV above the VBM, where the small differences between the formation energies of the $\text{As}_{\text{Ga}}\text{-O}_{\text{As}}$ and O_{b} defects suggest that these two defects coexist.

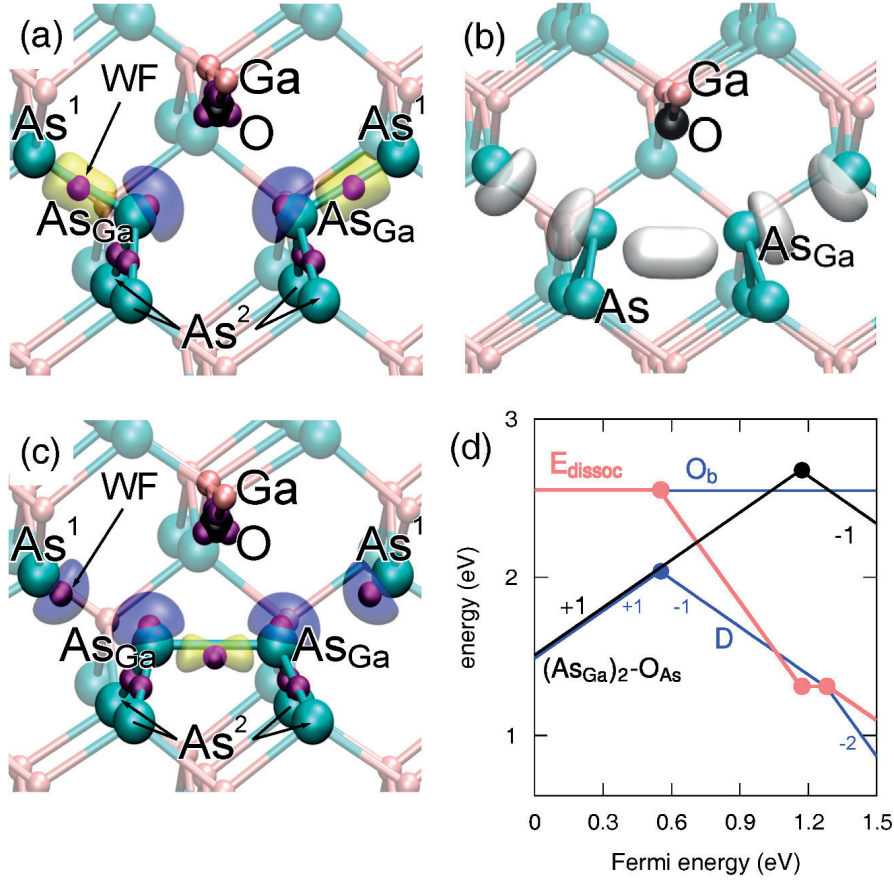


Figure 4.8 – $(\text{As}_{\text{Ga}})_2\text{-O}_{\text{As}}$ defect: (a) relaxed structure in the -1 , (b) neutral, (c) $+1$ charge state, and (d) formation (black) and dissociation (red) energies vs Fermi energy. In (a) and (c) relevant maximally localized Wannier functions (WF) are illustrated through their centers (small violet spheres) and through their isosurfaces, in (b) the charge density of the unpaired electron is shown in transparency. In (d), we also show the formation energies of the dissociation products (blue), the bistable $V_{\text{As}}\text{-}2\text{As}_{\text{Ga}}/V_{\text{Ga}}\text{-As}_{\text{Ga}}$ defect complex (D) and the O_{b} defect.

$(\text{As}_{\text{Ga}})_2\text{-O}_{\text{As}}$

The $(\text{As}_{\text{Ga}})_2\text{-O}_{\text{As}}$ defect structure was initially proposed by Pesola *et al.* [45] as origin of the experimentally identified Ga–O–Ga structure. To support this assignment, they showed that the defect is stable in its charge states $+1$ and -1 , while the neutral state is metastable, accounting for the observed negative- U behavior of the defect. The Ga–O–Ga structural unit was found to be stable in all the charge states of the defect and the calculated vibrational frequencies to agree with the experimental characterization.

Our relaxed structures of the $(\text{As}_{\text{Ga}})_2\text{-O}_{\text{As}}$ center (Fig. 4.8(a-c)) show overall good agreement with those found in Ref. [45]. The Ga–O–Ga unit in the defect core is largely insensitive to the charge state with Ga–O bond lengths of $1.83 \pm 0.01 \text{ \AA}$ and a Ga–O–Ga bond angle of $136.9^\circ \pm 1^\circ$,

²We here calculate the formation energy of the bistable $V_{\text{Ga}}/V_{\text{As}}\text{-As}_{\text{Ga}}$ defect at the same level of theory as the other O defects, finding good agreement with the calculations of Ref. [172].

thereby accounting for the close frequencies of the LVM bands. The As antisites in the defect core show more significant structural variations among the charge states. To explain the observed features, we adopt an analysis based on maximally localized Wannier functions [184] which allow for a real-space representation of the electron localization. In the positive charge state, the As antisites form three bonds with the surrounding As atoms, as shown in Fig. 4.8(a). The $\text{As}_{\text{Ga}}\text{-As}$ distances are $2.52 \pm 0.01 \text{ \AA}$, while the $\text{As}_{\text{Ga}}\text{-As}_{\text{Ga}}$ distance is 3.52 \AA . In our electronic-structure analysis, we find a single WF between the As_{Ga} and its As neighbors while two such WFs are found in between the As antisites. This indicates that the former linkages correspond to regular bonds, while the central antisites are not bonded and each of them carries a doubly occupied dangling bond (DB) pointing to the Ga-O-Ga unit [Fig. 4.8(a)]. The electron counting rule is then satisfied. In the negative charge state, the two As antisites are found at a closer distance (2.74 \AA), while the distances between the central As antisites and their neighboring As^1 increases to 2.89 \AA . The WF analysis indicates that the former linkage now corresponds to a regular bond while the latter are no longer bonded and give rise to the appearance of DBs at the As^1 sites [Fig. 4.8(c)]. The $\text{As}_{\text{Ga}}\text{-As}^2$ bond length is found to remain almost unchanged, at a value of 2.48 \AA . This defect structure satisfies the electron counting rule. The addition of two electrons to the charge state +1 thus leads to the net effect of transforming one of the As-As bonds into a couple of doubly occupied DBs. The structural variations between the +1 and -1 charge states are at the origin of the negative- U behavior of this center (vide infra). We note that the DBs on the central As antisites in the charge state -1 have slightly turned away from the Ga-O-Ga core structure, thereby lowering the steric constraints on the O vibrational modes and providing a simple explanation for the lower frequency of the B band with respect to that of the A band. In the neutral charge state [Fig. 4.8(b)], the $\text{As}_{\text{Ga}}\text{-As}_{\text{Ga}}$ bond is only singly occupied, as can be derived from electron counting arguments, in agreement with the paramagnetic behavior observed experimentally [40]. Moreover, the depletion of the central $\text{As}_{\text{Ga}}\text{-As}_{\text{Ga}}$ bond leads to a slight increase of the $\text{As}_{\text{Ga}}\text{-As}_{\text{Ga}}$ bond length (2.99 \AA) and to a slight decrease of the $\text{As}_{\text{Ga}}\text{-As}^1$ distance (2.72 \AA) as compared with the negative charge state. The DBs of the central As antisites do not change their orientation with respect to the charge -1, consistent with the close frequencies of the B and B' bands.

Figure 4.8(d) displays the formation energies of the various charge states of the $(\text{As}_{\text{Ga}})_2\text{-O}_{\text{As}}$ as a function of Fermi energy. The reported formation energies include finite-size corrections of 0.13 and 0.14 eV in the charge states +1 and -1, respectively. From Fig. 4.8(d), it is seen that the defect is amphoteric providing a mechanism [127] by which the experimentally observed Fermi-level pinning [31, 33, 34] can be accounted for [180]. As can be seen from Table 4.3, this brings this level in very close agreement with the experimental Fermi-level pinning position at $0.40 \pm 0.03 \text{ eV}$ below the CBM [31, 33, 34]. This result confers strong support to the assignment of the Fermi-level-pinning behavior to the $(\text{As}_{\text{Ga}})_2\text{-O}_{\text{As}}$ center.

A detailed characterization of the Ga-O-Ga center has been provided in terms of optical transition energies between its charge states [33], against which the $(\text{As}_{\text{Ga}})_2\text{-O}_{\text{As}}$ defect model has hitherto not adequately been confronted. Following the experimental work of Alt [33], we focus on the optical transitions from the valence band to the positive charge state of the defect ($A \rightarrow B'$) and from the negative charge state of the defect to the conduction band

³Ref. [33].

⁴Ref. [34].

Table 4.3 – Calculated charge transition level $\varepsilon(+/-)$ referred to the CBM and optical transition energies for the $(\text{As}_{\text{Ga}})_2\text{-O}_{\text{As}}$ center, compared with experimental results. Energies are given in eV.

	Theory	Experiment
Fermi-level pinning		
$\varepsilon(+/-)$	-0.37	-0.43 ³ , -0.36 ⁴
Optical transitions		
$A \rightarrow B'$	1.39	1.37 ²
$B \rightarrow B'$	0.69	0.65 ²

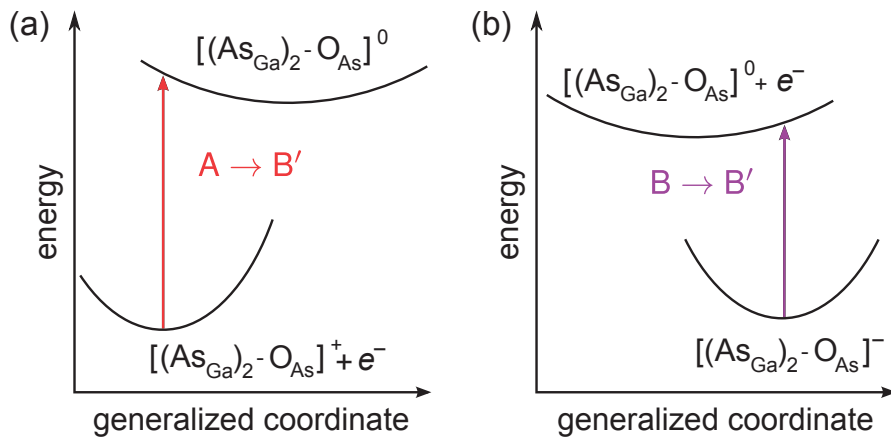


Figure 4.9 – Schematic configuration-coordinate diagrams illustrating the optical transitions involving the charged states of the $(\text{As}_{\text{Ga}})_2\text{-O}_{\text{As}}$ defect: (a) from the valence band to the positive charge state of the defect ($A \rightarrow B'$) and (b) from the negative charge state of the defect to the conduction band ($B \rightarrow B'$).

($B \rightarrow B'$). In the corresponding calculations, the optical transition energies are obtained by keeping fixed the structural configuration of the initial state, as illustrated in Fig. 4.9 through configuration-coordinate diagrams. The energy of the optical transition then corresponds to the energy difference between the final and initial state taken at the VBM or CBM depending whether the final state contains a hole at the VBM or an electron at the CBM. As given in Table 4.3, calculated and measured transition energies agree within less than 0.05 eV, thereby further corroborating the assignment of the Ga-O-Ga center to the $(\text{As}_{\text{Ga}})_2\text{-O}_{\text{As}}$ defect. We note that, the atomic transformation underlying the amphoteric behavior of the $(\text{As}_{\text{Ga}})_2\text{-O}_{\text{As}}$ defect corresponds to the bistability of the As-As dimer/DB defect [185]. Indeed, the structural rearrangements ensuing the capture/release of two electrons can be condensed as follows:



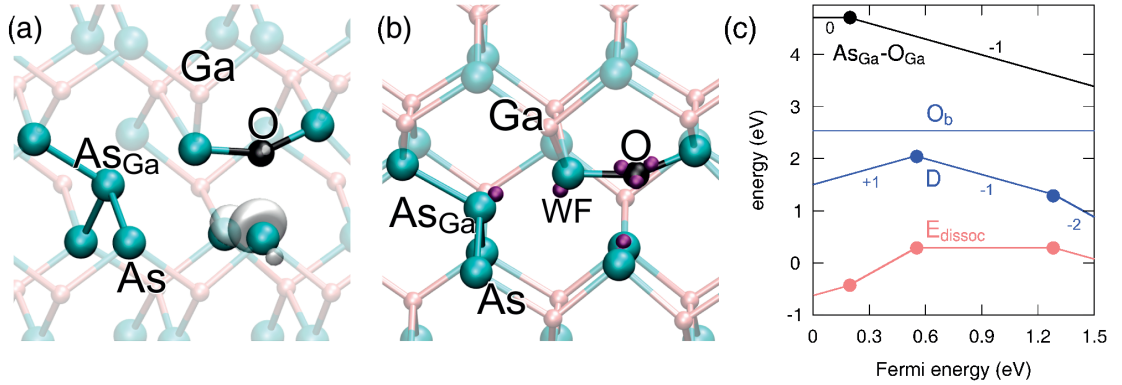


Figure 4.10 – $\text{As}_{\text{Ga}}\text{-O}_{\text{Ga}}$ defect: (a) relaxed structure in the neutral charge state, (b) relaxed structure in the charge state -1 , and (c) formation (black) and dissociation (red) energies vs Fermi energy. An isosurface of the empty defect state obtained at the PBE level for the neutral charge state is shown in (a). The small violet spheres in (b) indicate the center of the relevant maximally localized Wannier functions. In (c), we also show the formation energies of the dissociation products (blue), the unoxidized bistable $\text{V}_{\text{As}}\text{-2As}_{\text{Ga}}/\text{V}_{\text{Ga}}\text{-As}_{\text{Ga}}$ defect complex (D) and the O_{b} defect.

For examining the stability of the $(\text{As}_{\text{Ga}})_2\text{-O}_{\text{As}}$ defect, we consider the dissociation into the $\text{V}_{\text{Ga}}\text{-As}_{\text{Ga}}$ defect complex (D) and the O_{b} defect, according to



The $\text{V}_{\text{As}}\text{-2As}_{\text{Ga}}$ defect complex corresponds to one stable structure of the bistable $\text{V}_{\text{Ga}}\text{-As}_{\text{Ga}}/\text{V}_{\text{As}}\text{-2As}_{\text{Ga}}$ defect complex studied in Section 3. The dissociation energy of the $(\text{As}_{\text{Ga}})_2\text{-O}_{\text{As}}$ defect is displayed in Fig. 4.8(d). It is found to be larger than 1 eV for all Fermi energies within the band gap, guaranteeing defect stability against dissociation. As far as the second criterion for defect occurrence is concerned, we note that the formation energy of the $(\text{As}_{\text{Ga}})_2\text{-O}_{\text{As}}$ defect is smaller than that of the O_{b} defect for all Fermi energies in the band gap, but a small energy region around the defect charge transition level at 1.16 eV above the VBM. Under oxygen doping conditions, the $(\text{As}_{\text{Ga}})_2\text{-O}_{\text{As}}$ defect complex is thus expected to be relevant. As its amphoteric nature leads to Fermi-level pinning at the $+1/-1$ charge transition level [127], one should expect that the $(\text{As}_{\text{Ga}})_2\text{-O}_{\text{As}}$ and O_{b} defects coexist due their close formation energies at these Fermi energies. This assessment is consistent with experimental observations inferring that the O_{b} and the Ga-O-Ga defects occur simultaneously [35, 36].

$\text{As}_{\text{Ga}}\text{-O}_{\text{Ga}}$

We consider the $\text{As}_{\text{Ga}}\text{-O}_{\text{Ga}}$ defect complex which consists in a O_{Ga} defect nearest neighbor to an As_{Ga} defect. In the neutral charge state, the As atom in the antisite position forms three short As-As bonds of length 2.50 Å, while the distance to the forth As atom is 2.69 Å. The O atom binds to two As atoms facing the Ga vacancy leaving the other two As atoms with DBs [Fig. 4.10(a)]. These dangling bonds are partially empty as shown by the isosurface of the lowest unoccupied state, which shows localized behavior already at the PBE level. This

defect structure does not satisfies the electron counting rule and the neutral charge state is paramagnetic.

Upon the capture of one electron the defect structure undergoes minimal variations. The analysis of maximally localized WF shows that the two threefold coordinated As atoms which face the vacancy carry a doubly occupied dangling bond. Moreover, it also shows that the As antisite is threefold coordinated as the forth As–As bond breaks in favor of the formation of two opposite As DBs, as shown in Fig. 4.10(b). This defect configuration satisfies the electron counting rule.

The present defect is stable in the neutral and in the singly positive charge state as shown in Fig. 4.10(c). The formation energy ranges between 4.64 and 3.33 eV from *p*-type to *n*-type conditions. The finite-size correction calculated for the charge state -1 amounts to 0.11 eV. The defect level falls 0.19 eV above the VBM coinciding at the limit of the energy range accessible through our mixed PBE and HSE scheme (cf. Section 2.2). However, the isosurface of the lowest unoccupied state of the neutral charge state already shows well localized behavior at the PBE level, ensuring that this defect state is well described at the semilocal level. Furthermore, we note that the present charge transition level is very close to the charge transition level of an isolated As DB calculated in bulk GaAs (0.16 above VBM) [109]. Indeed, the defect state actively involved in the charge capture process corresponds to two As dangling bonds which are either partially or completely filled.

The stability of the $\text{As}_{\text{Ga}}\text{-O}_{\text{Ga}}$ defect complex is examined by comparing its formation energy with those of its dissociation products, the $\text{V}_{\text{Ga}}\text{-As}_{\text{Ga}}$ defect complex (*D*) and the O_{b} defect, according to



The dissociation energy of the $\text{As}_{\text{Ga}}\text{-O}_{\text{Ga}}$ defect is positive for Fermi energies above $\text{VBM}+0.40$ eV and does not exceed ~ 0.5 eV, revealing its limited stability against dissociation. The second criterion disfavors the formation of the $\text{As}_{\text{Ga}}\text{-O}_{\text{Ga}}$ defect complex as its formation energies are larger than those of its dissociation products for all values of Fermi energy.

Relative concentrations of the $\text{As}_{\text{Ga}}\text{-O}_{\text{As}}$ and $(\text{As}_{\text{Ga}})_2\text{-O}_{\text{As}}$ defects in cooled down conditions

Among the oxygen defects considered in this work, the $\text{As}_{\text{Ga}}\text{-O}_{\text{As}}$ and the $(\text{As}_{\text{Ga}})_2\text{-O}_{\text{As}}$ complexes show the lowest formation energy as shown in Fig. 4.11. The structure of these defects highlights the interaction between the O_{As} defect and As antisite defects. Indeed, the $\text{As}_{\text{Ga}}\text{-O}_{\text{As}}$ defect complex can be pictured as an O_{As} defect, to which a first As_{Ga} defect attaches,



The $(\text{As}_{\text{Ga}})_2\text{-O}_{\text{As}}$ complex then results from the attachment of a second As antisite,



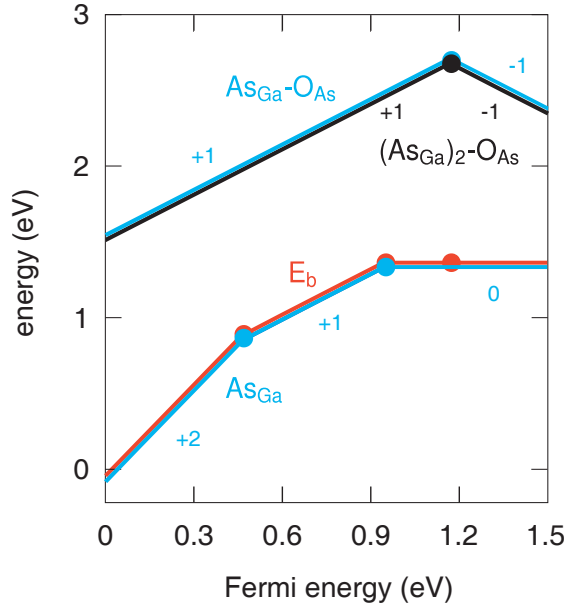


Figure 4.11 – Formation energy vs Fermi energy for the $(\text{As}_{\text{Ga}})_2\text{-O}_{\text{As}}$ defect complex (black) and for its dissociation products $\text{As}_{\text{Ga}}\text{-O}_{\text{As}}$ and As_{Ga} (light-blue) according to reaction (4.8). The corresponding binding energy E_b is also shown (red). The formation energies of $(\text{As}_{\text{Ga}})_2\text{-O}_{\text{As}}$ and $\text{As}_{\text{Ga}}\text{-O}_{\text{As}}$ are very close. Consequently, E_b essentially coincides with the formation energy of As_{Ga} .

At thermal equilibrium, the concentrations of the $\text{As}_{\text{Ga}}\text{-O}_{\text{As}}$ and $(\text{As}_{\text{Ga}})_2\text{-O}_{\text{As}}$ complexes are comparable to each other due to their very close formation energies (cf. Fig. 4.11). However, their relative concentration would be different when we consider cooled down conditions following a growth process at higher temperature [141]. To evaluate the binding energy for the attachment of an antisite, we compare in Fig. 4.11 the formation energies of $(\text{As}_{\text{Ga}})_2\text{-O}_{\text{As}}$ with those of its dissociation products, $\text{As}_{\text{Ga}}\text{-O}_{\text{As}}$ and the isolated As_{Ga} . The binding energy E_b , calculated in the same way as the dissociation energy given in Eq. (3.1), is essentially positive over the whole range of Fermi energies in the band gap, indicating stability of the $(\text{As}_{\text{Ga}})_2\text{-O}_{\text{As}}$ complex. More importantly, this assessment holds in correspondence of the charge transition levels of the defects at about 1.1 eV above the VBM, where the Fermi energy is expected to be pinned. At this value of the Fermi energy, $(\text{As}_{\text{Ga}})_2\text{-O}_{\text{As}}$ is 1.35 eV more stable than $\text{As}_{\text{Ga}}\text{-O}_{\text{As}}$ with an isolated As_{Ga} .

To determine the effect of these binding energies on the relative concentrations of these two complexes, we proceed as follows. Following Eq. (3.2), we express the thermodynamic equilibrium concentration of isolated As antisites $[\text{As}_{\text{Ga}}]$ at the growth temperature T_g :

$$[\text{As}_{\text{Ga}}] = N_{\text{sites}} \exp[-E_f(\text{As}_{\text{Ga}})/kT_g]. \quad (4.9)$$

Due to its small formation energy, the As_{Ga} is the dominant defect [123]. We assume that this concentration remains unmodified upon cooling down to lower temperatures and that it is essentially unaffected by reactions (4.7) and (4.8). In this picture, we assume that the available

Chapter 4. Oxygen defects in bulk GaAs

As_{Ga} can diffuse in the GaAs lattice as an isolated species or be bound within the $\text{As}_{\text{Ga}}\text{-O}_{\text{As}}$ and $(\text{As}_{\text{Ga}})_2\text{-O}_{\text{As}}$ complexes. Additionally, for a given oxygen impurity concentration C , we have that

$$[\text{As}_{\text{Ga}}\text{-O}_{\text{As}}] + [(\text{As}_{\text{Ga}})_2\text{-O}_{\text{As}}] = C, \quad (4.10)$$

holds for any temperature. Focusing on reaction (4.8), the mass action law at the cooled down temperature T reads

$$\frac{[(\text{As}_{\text{Ga}})_2\text{-O}_{\text{As}}]}{[\text{As}_{\text{Ga}}\text{-O}_{\text{As}}] \cdot [\text{As}_{\text{Ga}}]} = \frac{N_{\text{config2}}}{N_{\text{sites}} \cdot N_{\text{config1}}} \exp(E_b / kT), \quad (4.11)$$

where N_{config1} and N_{config2} are numbers of similar order, corresponding to the number of equivalent defect configurations for $\text{As}_{\text{Ga}}\text{-O}_{\text{As}}$ and $(\text{As}_{\text{Ga}})_2\text{-O}_{\text{As}}$, respectively.

Using Eqs. (4.11) and (4.10), we obtain

$$[(\text{As}_{\text{Ga}})_2\text{-O}_{\text{As}}] = \frac{\alpha}{1 + \alpha} C, \quad (4.12)$$

with

$$\alpha = [\text{As}_{\text{Ga}}] \frac{N_{\text{config2}}}{N_{\text{sites}} \cdot N_{\text{config1}}} \exp(E_b / kT). \quad (4.13)$$

Since $N_{\text{config1}} \approx N_{\text{config2}}$, this expression simplifies to :

$$\alpha \approx \exp[-E_f(\text{As}_{\text{Ga}}) / kT_g + E_b / kT]. \quad (4.14)$$

Two extreme conditions can be identified. When $\alpha \gg 1$, $[(\text{As}_{\text{Ga}})_2\text{-O}_{\text{As}}] = C$ implying that all oxygen defects are in the form $(\text{As}_{\text{Ga}})_2\text{-O}_{\text{As}}$. At variance, for $\alpha \ll 1$, $[(\text{As}_{\text{Ga}})_2\text{-O}_{\text{As}}] \ll C$ and all oxygen atoms are in the form $\text{As}_{\text{Ga}}\text{-O}_{\text{As}}$.

In the case of interest to the present work, we infer from Fig. 4.11 that $E_f(\text{As}_{\text{Ga}}) \cong E_b$ leading to the preferential formation of $(\text{As}_{\text{Ga}})_2\text{-O}_{\text{As}}$ for $T < T_g$. This result disfavors the formation of the $\text{As}_{\text{Ga}}\text{-O}_{\text{As}}$ complex, which can thus be dismissed from the analysis.

Conclusions

Here, we conclude this Section summarizing in Fig. 4.12 the calculated formation energies of the defects considered. The most stable oxygen defects are the O_b defect and the O substitutional to As attached to either one ($\text{As}_{\text{Ga}}\text{-O}_{\text{As}}$) or two $[(\text{As}_{\text{Ga}})_2\text{-O}_{\text{As}}]$ As antisites. The $(\text{As}_{\text{Ga}})_2\text{-O}_{\text{As}}$ defect was originally proposed by Pesola and coworkers and was shown to agree with experimental observations as far as the O local environment and vibrational frequencies are concerned [45]. However, this previous study did not establish a clear link with the electrical characterization and the optical transitions between different charge states of the defect and did not clarify whether this defect is expected to dominate in GaAs:O samples. In the present work, we find that the O_b defect is electrically inactive with a formation energy of 2.54 eV. The $\text{As}_{\text{Ga}}\text{-O}_{\text{As}}$ and $(\text{As}_{\text{Ga}})_2\text{-O}_{\text{As}}$ defects show essentially equivalent energetics. They are both

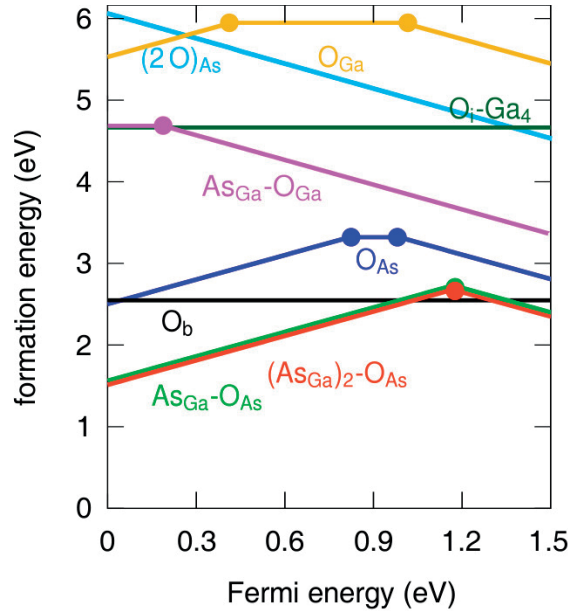


Figure 4.12 – Formation energy vs Fermi energy for the bridging interstitial oxygen defect O_b (black), the O_i -Ga₄ defect (dark-green), the O_{Ga} defect (yellow), the O_{As} defect (dark-blue), the $(2O)_{As}$ defect (light-blue), the As_{Ga} - O_{As} defect complex (light-green), the $(As_{Ga})_2$ - O_{As} defect complex (red), and the As_{Ga} - O_{Ga} defect complex (pink). As-rich conditions are assumed.

stable in the charge states +1 and -1, and both have formation energies of 1.55 and 2.33 eV in *p*-type and *n*-type condition, respectively. Their charge transition level at 1.16 eV above VBM is in good agreement with the experimental pinning level [33]. Both defects are stable against oxygen release and at the thermodynamic equilibrium they are expected to coexist with the O_b defect for Fermi energies close to the pinning level. However, taking into account the binding of As antisites, we conclude that the $(As_{Ga})_2$ - O_{As} complex is expected to dominate upon cooldown.

The formation energies of the other defects considered in this work are larger than that of the O_b defect, indicating that their formation is unfavorable. In particular, the formation energy of the isolated O_{As} defect is higher by ~0.5 eV than that of defect complexes in which the O_{As} defect is attached to one or two As antisites. The acceptor $(2O)_{As}$ defect, in which two O atoms are captured within the cavity of an As vacancy, is stable in the charge state -1 across the full band gap, with formation energies ranging between ~4.5 and ~6 eV. The interstitial O -Ga₄ defect is neutral and its formation involves a cost of 4.6 eV, more than 2 eV larger than that of the O_b defect, while the O -As₄ defect has been found to be unstable and to spontaneously transform into the O -Ga₄ defect. Finally, the substitutional O_{Ga} defect shows a formation energy ranging between 5 and 6 eV, about 3 eV larger than that of the other substitutional defect O_{As} , in both *p*-type and *n*-type conditions. Our calculations generally show that the defects with the lowest formation energies are characterized by O-Ga bonds, in agreement with the higher stability of Ga oxides with respect to As oxides [69, 71, 186, 187].

In conclusion, we have shown that the $(As_{Ga})_2$ - O_{As} defect complex corresponds to the domi-

nant oxygen defect in GaAs. The only competing O defect is the bridging oxygen interstitial (O_b), which shows close formation energies in correspondence of the charge transition level of the $(As_{Ga})_2-O_{As}$ complex. Since the Fermi level is found to pin in correspondence of this defect level, this finding suggests that the $(As_{Ga})_2-O_{As}$ and O_b could coexist, in accord with experimental observations [35, 36]. Our work also shows that this defect complex is stable both against the release of oxygen and the detachment of As_{Ga} antisites. Finally, the $(As_{Ga})_2-O_{As}$ defect is found to accurately account for the experimental Fermi-level-pinning position. Furthermore, the optical transition energies between its charge states closely reproduce the experimental values. These results bring the theoretical description of the $(As_{Ga})_2-O_{As}$ defect in agreement with the full experimental characterization of the Ga-O-Ga center and strongly support this defect as origin of the Fermi-level pinning in oxygen-doped GaAs.

5 Intermediately oxidized GaAs

In this Chapter, we consider intermediately oxidized GaAs compounds. In particular, in Section 5.1, we study the early stages of oxygen deposition on the GaAs(110) surface. Considering a more advanced stage in the oxidation process, we study in Section 5.2 the structural, the electronic, and the defect properties of the transition layer separating the GaAs substrate from the oxide. Parts of this Chapter can be found in peer-reviewed articles [3, 185].

5.1 Oxygen deposition on the GaAs(110) surface

Despite the fact that the clean GaAs(110) surface does not show any surface states [60], the deposition of very small quantities of various metals or oxygen are sufficient to induce Fermi-level pinning [51]. The pinning occurs at fixed energies which do not depend on the deposited species, suggesting that an intrinsic mechanism is operative. Since the observed pinning levels closely correspond to the defect levels of the As antisites, it was assumed that the pinning behavior originates from such defects together with charge compensating spectator defects of unknown origin [52]. However, whereas several experiments have pointed to a high concentration of As antisite defects in GaAs [31, 32], no definite evidence for the existence of spectator defects has been found.

Computational details

The surface is modeled through a slab of 5 GaAs layers within a simulation cell defined by a surface repeat unit of 3×6 atoms and a vacuum separation of 18 Å. One of the two surface layers is saturated with pseudo-hydrogen atoms carrying 1.25 and 0.75 electrons to satisfy the electron counting rule and is kept fixed during the simulations. We adopt a **k**-point sampling consisting of a $3 \times 3 \times 3$ mesh which ensures converged total energy differences, together with a kinetic energy cutoff of 90 Ry. The present calculations are performed at the PBE level.

Formation of a bistable As–As dimer

We first focus on the atomic rearrangements occurring at the GaAs(110) surface prior to oxygen deposition. Upon structural relaxation, the As rows carrying doubly occupied dangling

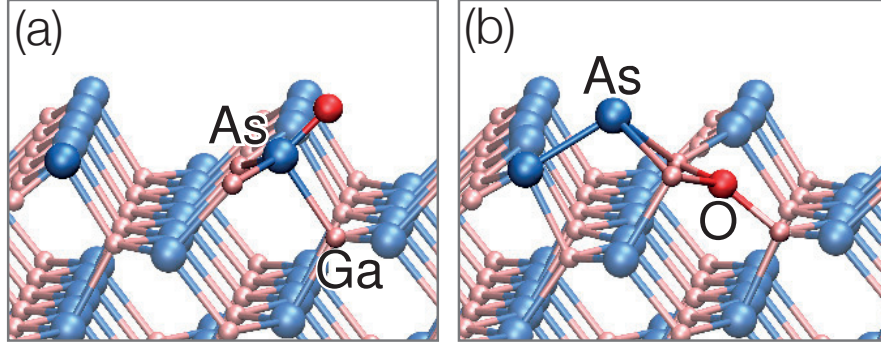
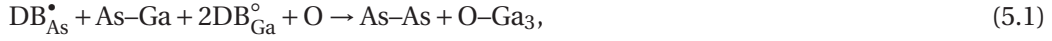


Figure 5.1 – Relaxed atomic structures of an O atom absorbed at the GaAs(110) surface. (a) and (b) correspond to the initial and final configurations of our MD simulation, respectively.

bonds (DB_{As}^*) move outwards while the Ga atoms carrying empty dangling bonds (DB_{Ga}^o) move inwards, as a consequence of charge rearrangement.

We then allow an isolated O atom to form a bond with a surface As atom [configuration A shown in Fig. 5.1(a)], following evidence from photoemission [51] and scanning-tunneling-microscopy [188]. The system is evolved through first-principles molecular dynamics at a temperature of 800 K, close to realistic oxidation conditions [97]. After 2 ps, the system transforms to a different configuration [B structure shown in Fig. 5.1(b)], in which an As–As dimer is formed and the O atom is coordinated with three Ga atoms, according to the reaction:



where $O-Ga_3$ indicates the threefold coordinated O atom. In order to study the minimum energy path connecting these two states we perform a NEB calculation using 29 images and two climbing images. Fig. 5.2 shows the MEP between the initial (A) and the final (B) structures. The oxidation reaction is exothermic by 2.0 eV and sequentially proceeds through two barriers of 0.1 eV and 0.4 eV, corresponding to the breaking of an As–Ga and of an As–O bond, respectively.

From the products of the reaction in Eq. (5.1), one notices that the electron counting rule is exactly satisfied. Indeed, the breaking of the As–Ga bond provides two electrons which are required for the bonding of an oxygen atom to three DB_{Ga}^o . The remaining DB_{As}^o then joins with the DB_{As}^* to form an As–As dimer.

Furthermore, we study the ability of the structure B to trap and release electrons. Upon the addition of two electrons and structural relaxation, the As–As dimer breaks giving rise to two doubly occupied dangling bonds. When the two additional electrons are removed, the As–As dimer is restored upon relaxation, leading to the same mechanism described in Chapter 3 and summarized in Fig. 3.8. Hence, this description establishes a direct link between GaAs oxidation and the formation of the As–As dimer/DB defect responsible for charge trapping (vide infra). Furthermore, the resulting surface transformation provides a mechanism by which the observed enrichment in interfacial As–As bonds occurs [106, 189].

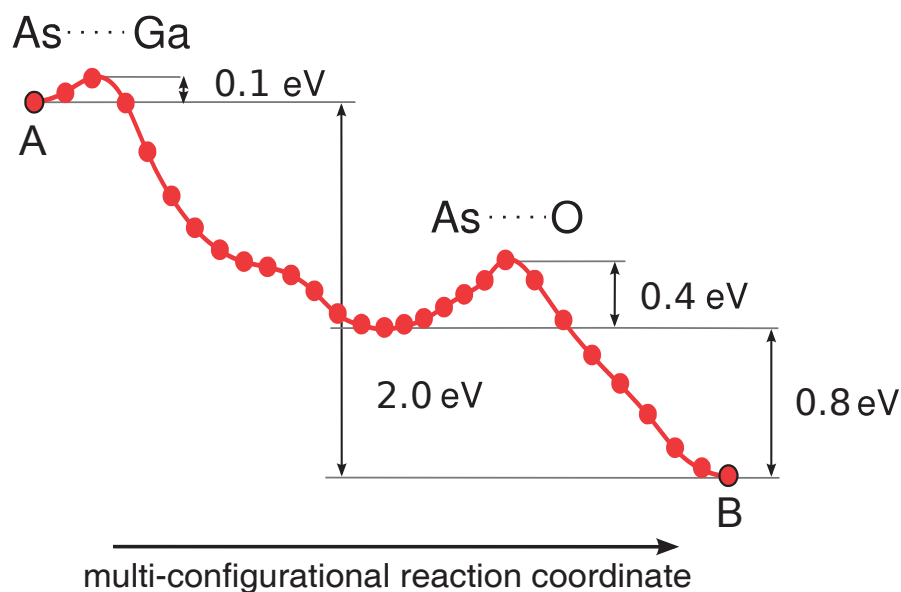


Figure 5.2 – Minimum energy path corresponding to the oxidation reaction at the GaAs(110) surface from the initial configuration (A) [shown in Fig. 5.1(a)] to the final configuration (B) [shown in Fig. 5.1(b)], as obtained through a nudged-elastic-band calculation [156]. We use 29 images, two of which are let free to climb the potential energy surface [157]. The two barriers correspond to the breaking of As–Ga and As–O bonds.

5.2 Ga As suboxide: an interfacial transition layer

It is known that ALD-generated GaAs/oxide interfaces present a suboxide transition layer between the semiconductor and the stoichiometric oxide [77]. This contrasts with the atomically controlled interfaces obtained through molecular beam epitaxy, which have been demonstrated to give rise to unpinned GaAs/oxide interfaces [66]. Hence, remarkable experimental efforts have been employed for achieving defect-free ALD interfaces by varying the synthesis and passivation procedures, in particular focusing on the removal of any native oxide species from the GaAs-based substrate [72, 73, 74, 75, 76, 77]. The reduction of the native oxide can be obtained through thermal treatments and self-cleaning processes [74, 190]. In particular, as shown by medium energy ion scattering spectroscopy and x-ray photoelectron spectroscopy, the deposition of trimethylaluminum is able to achieve a 65% reduction of the native oxide resulting in a thin suboxide layer composed of $\text{Ga}_2\text{As}_{0.3}\text{O}_2$ [74].

Computational details

We consider two amorphous models with different composition and generated through density-functional MD. To identify defects in our disordered model structures, we perform charging/discharging cycles until the defect structure no longer evolves [191]. Once optimally relaxed structures are obtained, the electronic structure is further described using the HSE functional with the Fock exchange parameter set to the same value used for bulk GaAs (cf. Section 2.2). To correct our defect energies from finite-size effects we use an intermediate

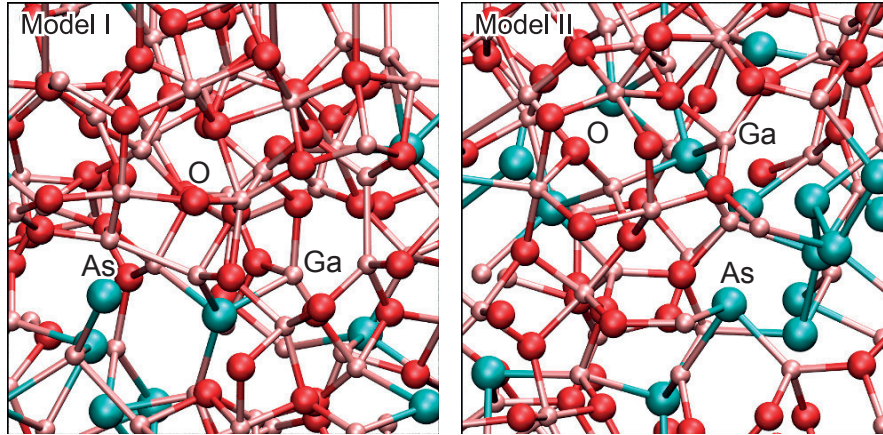


Figure 5.3 – Relaxed structures of amorphous suboxide models I and II. Ga, O, and As atoms are represented by pink, red, and light-blue spheres, respectively.

value for the dielectric constant, taken between those of GaAs and Ga_2O_3 . This choice affects the defect level by less than ~ 50 meV.

Structural properties

The initial configurations of the molecular dynamics simulations are generated from the α -phase of Al_2O_3 by randomly substituting Al atoms with Ga and As atoms and randomly inserting vacancies in both anion and cation sublattices until the desired stoichiometry is reached (cf. Table 5.1). For model I, the composition is taken to match the one resulting from the experimental characterization [74], whereas the composition in model II corresponds to a 50%-50% combination of GaAs and Ga_2O_3 . For each model, we perform an isobaric-MD simulation at 300 K for a period of 3 ps, in which one lattice parameter is let free to relax. Then, we fix the volume to the average value calculated over the last 2 ps of the simulation. Melt phases are generated through MD simulations at 3500 K for 5 ps. The melt is first quenched to 1500 K in 15 ps. After an equilibration for at least 5 ps, a further quench lasting 10 ps brings the temperature to 300 K. The volume of our amorphous models is then reoptimized achieving further density variations smaller than 7%. The final suboxide models I and II are illustrated in Fig. 5.3 and show densities of 5.52 g/cm^3 and 5.42 g/cm^3 , respectively.

Table 5.1 – Composition expressed in terms of GaAs and Ga_2O_3 and number of atoms in the present suboxide models.

Model	Composition	Number of atoms		
		Ga	As	O
I	$(\text{GaAs})_{0.23}(\text{Ga}_2\text{O}_3)_{0.50}\text{Ga}_{0.27}$	56	8	56
II	$(\text{GaAs})_{0.50}(\text{Ga}_2\text{O}_3)_{0.50}$	48	16	48

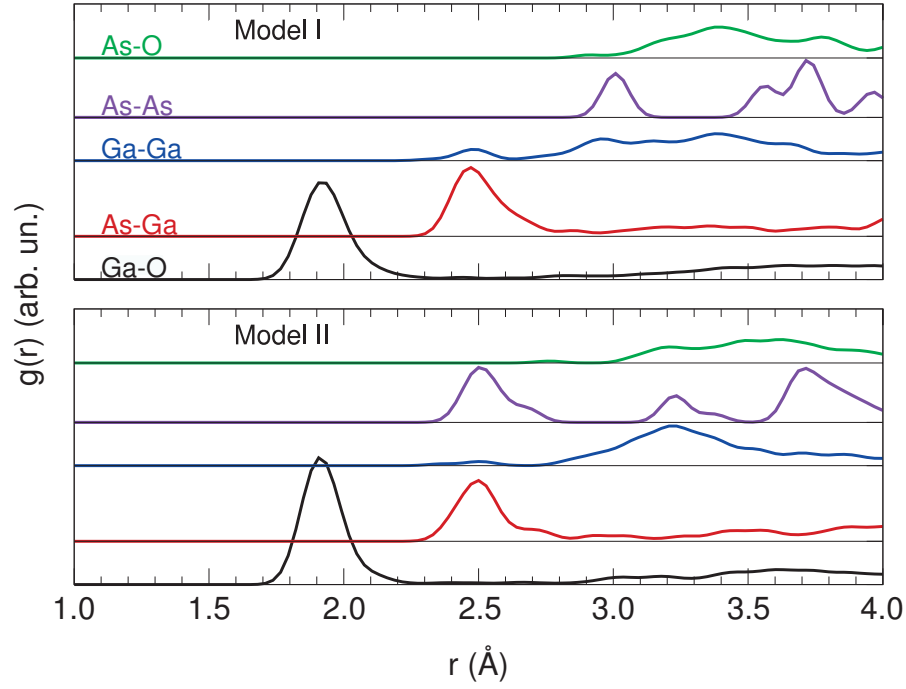


Figure 5.4 – Pair correlation functions $g(r)$ for the amorphous suboxide models I and II: Ga–O, As–Ga, Ga–Ga, As–As, and As–O. A Gaussian broadening with a standard deviation of 0.05 Å has been performed.

The study of the pair correlation functions $g(r)$ allows us to identify the nature of the atomic bonds in our model structures. The suboxide models show Ga–O, As–Ga, Ga–Ga, and As–As bonds with an average bond length of 1.9 Å, 2.5 Å, 2.5 Å, and 2.5 Å, respectively (Fig. 5.4). These values compare well with respective bond lengths of Ga–O bonds in gallium oxide (1.86 and 2.00 Å, Ref. [192]), of As–Ga bonds in bulk GaAs (2.45 Å, Ref. [14]), and of Ga–Ga (2.56 Å, Ref. [193]) and As–As bonds (2.51 Å, Ref. [194]) at reconstructed GaAs surfaces. The absence of any feature at distances smaller than 3.0 Å in the As–O correlation function indicates the absence of As–O bonds in our suboxide models (Fig. 5.4). Arsenic atoms generally bind to Ga atoms, but in model II one also observes the formation of As–As dimers. The present bonding pattern agrees well with the preferential removal of As oxide in comparison to Ga oxide upon thermal and surface treatment. [74, 75]

To describe the bonding pattern, we perform an analysis based on maximally localized Wannier functions (WF), which give an effective real-space representation of the electron localization. We consider two atoms to be bound when their distance is lower than the cutoff distance and a WF center is found along the bond. Table 5.2 shows the partial coordination numbers $CN(X - Y)$ indicating the average number of atomic species Y belonging to the coordination shell of atomic species X . One observes that $CN(\text{Ga-O})$ and $CN(\text{O-Ga})$ do not differ sensibly between the two models suggesting that these coordination numbers are insensitive to the presence of excess Ga. However, the addition of extra As atoms in model II leads to relevant variations in the partial coordination numbers. As one could expect, $CN(\text{Ga-Ga})$ is reduced and

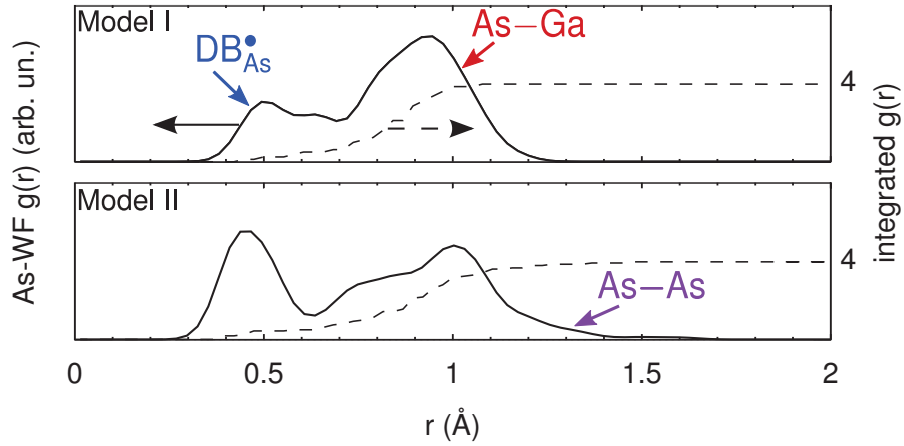


Figure 5.5 – Correlation function $g(r)$ between As and WF centers (continuous, referring to the vertical axis on the left) together with its running integration (dashed, referring to the vertical axis on the right) for models I and II.

CN(Ga-As) increased with respect model I. More interestingly, although there is no excess As with respect to the oxide stoichiometries, model II shows a finite value for CN(As-As) indicating the appearance of As-As bonds. This hints at the role of As in the formation of defects (vide infra).

In both our suboxide models, about 40% of the As atoms are threefold coordinated revealing the occurrence of As dangling bonds. To locate the center of the WF with respect to the As atoms, we focus on the As-WF correlation function (Fig. 5.5). From the running integral of the As-WF correlation function, one infers that every As atom has four WF centers within a distance of 2 Å, indicating that all the valence orbitals are fully occupied. The feature at ~ 0.5 Å in the As-WF correlation function clearly shows the presence of doubly occupied As dangling bonds ($\text{DB}_{\text{As}}^\bullet$), while the peak around 0.95 Å corresponds to regular As-Ga bonds. The feature extending beyond 1.25 Å in model II results from As-As homopolar bonds, in which the WF center is equidistant from the two As atoms (the As-As bond length being ~ 2.5 Å). Hence, we observe the coexistence of As-As and $\text{DB}_{\text{As}}^\bullet$ in model II. In this respect, the excess of Ga atoms in model I is seen to disfavor the formation of As-As bonds.

Table 5.2 – Partial coordination numbers $\text{CN}(X - Y)$ of atomic species X with atomic species Y in models I and II. We use cutoff distances of 2.5 Å for Ga-O bonds and of 2.9 Å for As-Ga, Ga-Ga, and As-As bonds.

$X \backslash Y$	Model I			Model II		
	O	Ga	As	O	Ga	As
O	-	3.16	-	-	3.15	-
Ga	3.16	0.54	0.50	3.13	0.17	0.92
As	-	3.63	-	-	2.75	0.69

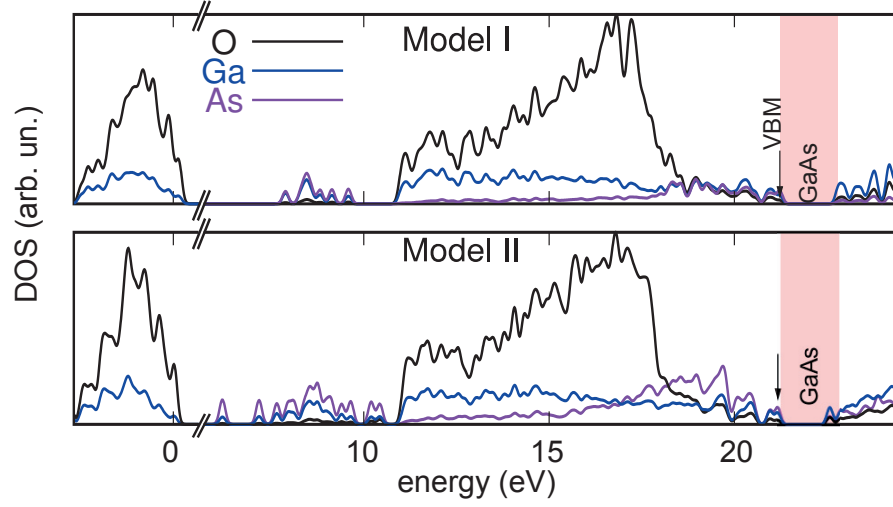


Figure 5.6 – Density of states projected on O, Ga, and As atoms for suboxide models I and II. The energies are referenced with respect to the 2s state of O atoms coordinated with two Ga atoms. The arrows identify the highest occupied state. The shaded areas indicate the location of the GaAs band gap, as aligned through an O-related defect in GaAs.

Electrical properties

In Fig. 5.6, we give the density of states for each of the two models as obtained at the hybrid functional level. The calculated band gaps are 1.6 eV for model I and 1.4 eV for model II, both rather close to the band gap of bulk GaAs (1.52 eV, Ref. [14]). To align the densities of states of the suboxides to the GaAs band gap, we focus on oxygen atoms in the suboxide models, which are twofold coordinated with Ga atoms. Their average 2s level is then aligned with that of the $(\text{As}_{\text{Ga}})_2\text{-O}_{\text{As}}$ defect in GaAs which presents the same nearest neighbor configuration [180]. Such an alignment procedure based on O 2s levels has previously been demonstrated to give reliable results for various band alignments [78, 195, 196]. With this alignment, the conduction and valence band offsets between GaAs and the suboxides are very small, on the order of 0.1–0.2 eV (cf. Fig. 5.7). The similarities between the band structures of GaAs and its suboxide stem from the fraction of GaAs incorporated in the suboxide models. Indeed, the projected densities of states on the various atomic species shows that the weight of Ga and As is dominant in the vicinity of the band gap (Fig. 5.6).

Defect search

The densities of states do not show any state in the band gap but one should focus on charge transition levels to identify possible electrically-active defects. Their calculation involves the addition or removal of electrons and the subsequent relaxation of the charged structures. Upon the removal of two electrons, model I undergoes a reversible transformation from two adjacent doubly occupied As dangling bonds to an As–As dimer according to the reaction:



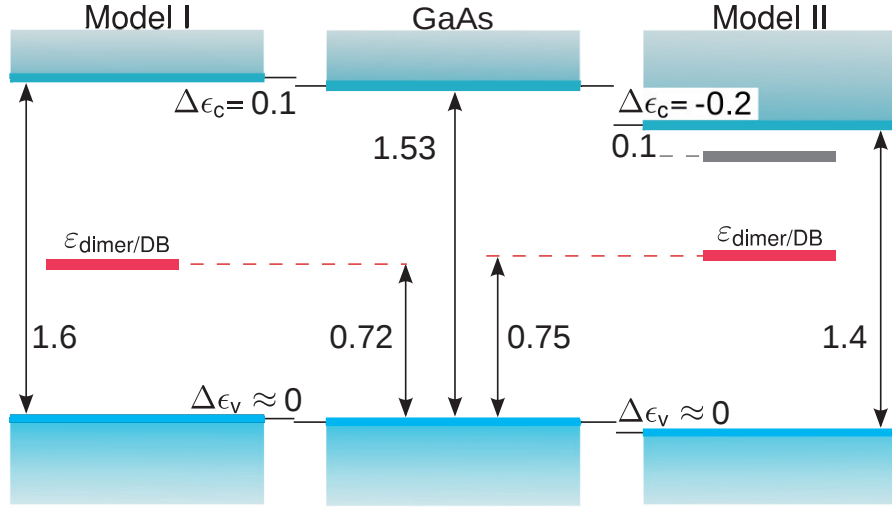


Figure 5.7 – Band alignments of suboxide models I (left panel) and II (right) with GaAs (middle). The valence ($\Delta\epsilon_v$) and conduction ($\Delta\epsilon_c$) band offsets are indicated. Calculated charge transition levels of the dimer/DB defect ($\epsilon_{\text{dimer/DB}}$) as calculated in models I and II are also shown. For model II, the charge transition level associated to a delocalized state is found at 0.1 eV from the bottom of the suboxide conduction band. Energies are in eV.

This defect coincides to the As–As dimer/DB defect formed at the surface upon O deposition (cf. Section 5.1) and involved in bulk defect complexes (cf. Chapters 3 and 4). The present alignment scheme sets the charge transition level of the dimer/DB defect level at 0.72 eV from the valence band maximum (VBM) of GaAs, as shown in Fig. 5.7. The calculated defect level thus coincides with the dominant peak at mid gap observed in the defect density of states at the GaAs/oxide interface, also found at 0.7 eV above the VBM. [103, 104]

We next investigate possible charge transition levels in model II. Given the occurrence of an As–As dimer in this model, we add two electrons to induce bond breaking. However, the charging leads to a more complex bond rearrangement involving the As dimer atoms but also a nearby Ga atom. The added electrons are finally found to be delocalized over a series of distorted Ga–As and As–As bonds, giving a charge transition level at only 0.1 eV below the conduction band of the suboxide (Fig. 5.7). Given the shallow nature of this state and its likely sensitivity to finite-size effects, no general conclusion can be drawn about the existence of such a state. In search of more localized defect states, we thus modify the structure of model II by removing the Ga atom which concurred to the structural rearrangements and saturating the remaining dangling bonds with H atoms. The modified suboxide model shows an isolated dimer/DB transformation upon capture and release of two electrons. The calculated defect level falls at 0.75 eV from the VBM of GaAs (Fig. 5.7), very close to the analogous level of model I found at 0.72 eV from the VBM of GaAs.

This result identifies the dimer/DB defect as a primary defect in GaAs-related systems and supports its assignment to the peak at mid gap observed in the density of defect states. Furthermore, the present results support that this defect is not necessarily only found at the termination of the GaAs substrate (upon surface reconstruction) but that it could also occur in

5.2. Ga As suboxide: an interfacial transition layer

the disordered part of the interfacial transition region. The study of our suboxide models shows that the presence of excess Ga reduces the chances of As–As dimer formation, thereby providing a natural explanation for the improved electrical behavior of devices prepared starting from Ga-rich GaAs surfaces. [104] As a side remark, we note that the Ga–Ga dimers which are present in our amorphous models do not undergo bistability upon the charging/discharging process, suggesting their electrical inactivity.

6 GaAs/oxide interface

In this Chapter we consider the GaAs/Al₂O₃ interface. In Section 6.1, we study the band alignment between GaAs and Al₂O₃. For the oxide component, we generate through MD simulation a disordered model which shows structural properties in good agreement with the experimental characterization. In Section 6.2, we study structural and electrical properties of GaAs defects at the interface. We consider a set of defects which have been shown to be relevant in the pinning of the Fermi-level in GaAs. The understanding achieved in this study is then applied to the case of InGaAs interfaces in Section 6.3. Parts of this Chapter can be found in peer-reviewed articles [1, 2, 185].

6.1 Band alignment and chemical bonding at the GaAs/Al₂O₃ interface

The band alignment at the interface between GaAs and amorphous Al₂O₃ (*a*-Al₂O₃), here denoted as GaAs/Al₂O₃ interface, is an important feature that characterizes its electronic properties. There is some incertitude in the valence band offset, with measured values ranging between 2.6 and 3.8 eV [86, 87, 88, 89, 90]. A theoretical study favors the lower valence band offsets with a calculated value of 2.8 eV, but this study might suffer from the fact that the adopted model relies on a strained crystalline phase of Al₂O₃ [197]. Also, it is not clear whether the relatively high concentration of defects observed with either X-ray photoemission [96] or electron spin resonance [106] could affect the band alignment. Concerned defects are As–As homopolar bonds and As antisites, both of which have already been the object of intense experimental and theoretical investigations [95, 98, 99, 103, 108, 115, 117, 160].

Computational details

In the amorphous calculations the Brillouin zone is sampled at the sole Γ point ¹, while a $2 \times 2 \times 2$ Monkhorst-Pack mesh is used for the interface models, ensuring converged properties as in the ensuing study of defects (Section 6.2). Structural relaxations are carried out at the PBE level. The electronic properties are then evaluated through the HSE functional in which we

¹The Γ point gives converged structural and electronic properties as verified with a $2 \times 2 \times 2$ Monkhorst-Pack mesh, corresponding to a \mathbf{k} -point density similar to that used for crystalline α -Al₂O₃ and κ -Al₂O₃.

adjust the fraction of Fock exchange to reproduce the experimental band gap of the material under consideration.

We determine the band offsets at the GaAs/Al₂O₃ interface following the scheme proposed in Refs. [198, 199]. First, the two interface components are treated separately as bulk materials. For bulk GaAs, we determine the band edges with respect to the average electrostatic potential taken as reference level. For amorphous Al₂O₃, we consider a disordered bulk model and refer the band edges to an atomic reference level consisting of the average 2s level of twofold coordinated O atoms. The line-up between the average electrostatic potential of GaAs and the oxide reference level is then achieved through an atomistic model structure of the GaAs/Al₂O₃ interface. In the interface model, the reference values of the two interface components are determined in bulk-like regions, which are unaffected by interface effects. The use of an atomic reference level for the oxide is motivated by its disordered nature. In particular, the use of O 2s levels has been shown to be robust and to give reliable results for variety of systems [78, 195, 196]. In the determination of band offsets, the accurate reproduction of the band gaps of the individual interface components has been demonstrated to be important [150]. For this, we will take advantage of the possibility of separately adapting the fraction of Fock exchange for each interface component. The choice of Fock exchange in the interface calculations is not critical, as the electrostatic line-up is hardly affected [150].

The properties of bulk GaAs are obtained from a bulk calculation carried out using the same computational framework as described in Section 2.2.

Amorphous Al₂O₃

The study of the oxide component requires more care because of its disordered structure. We generate a model of *a*-Al₂O₃ via Born-Oppenheimer MD simulations. We achieve the initial configuration by adapting a 160-atom model of *κ*-Al₂O₃ to an orthorhombic supercell. The equations of motion are evolved with a timestep of 1.2 fs. After equilibration at 3000 K for 1 ps, the melt is quenched to 300 K in 14 ps. The structure is then relaxed preserving only the shape of the supercell and allowing the lattice constants to relax freely in order to eliminate the residual stress. The final model of *a*-Al₂O₃ is obtained after an equilibration run of 5 ps at 300 K. The resulting lattice vectors are 11.5, 11.2, and 12.8 Å, corresponding to a mass density of 3.31 g/cm³. This value falls well within the experimental range (3.05–3.65 g/cm³) [79, 80, 81].

To validate the structure of our amorphous model, we focus on its total neutron radial distribution function $g_N(r)$ as obtained through an average over the final MD run at 300 K (Fig. 6.1). The calculated $g_N(r)$ is in fair agreement with the experimental data from Ref. [80] [cf. Fig. 6.1(a)]. The first maximum of the calculated $g_N(r)$ occurs at 1.83 Å only at slightly larger values than that of its experimental counterpart at 1.80 Å [80]. As Fig. 6.1(b) clearly shows, this peak is due to the Al–O correlation function, indicating that our amorphous model overestimates the Al–O bond length by only 1.6%, in accord with typical deviations achieved at the semilocal functional level [201]. The partial correlation functions for Al–O, Al–Al, and O–O, shown in Fig. 6.1(b) allow us to define cut-off distances at 2.05, 3.53, and 3.23 Å for Al–O, Al–Al, and O–O, respectively. Partial coordination numbers $[CN(X - Y)]$ correspond to the average number of atoms of species *Y* in the first coordination shell of the atomic species *X*. The distributions of $CN(X - Y)$ are shown in Fig. 6.2 and agree well with a previous amorphous model generated

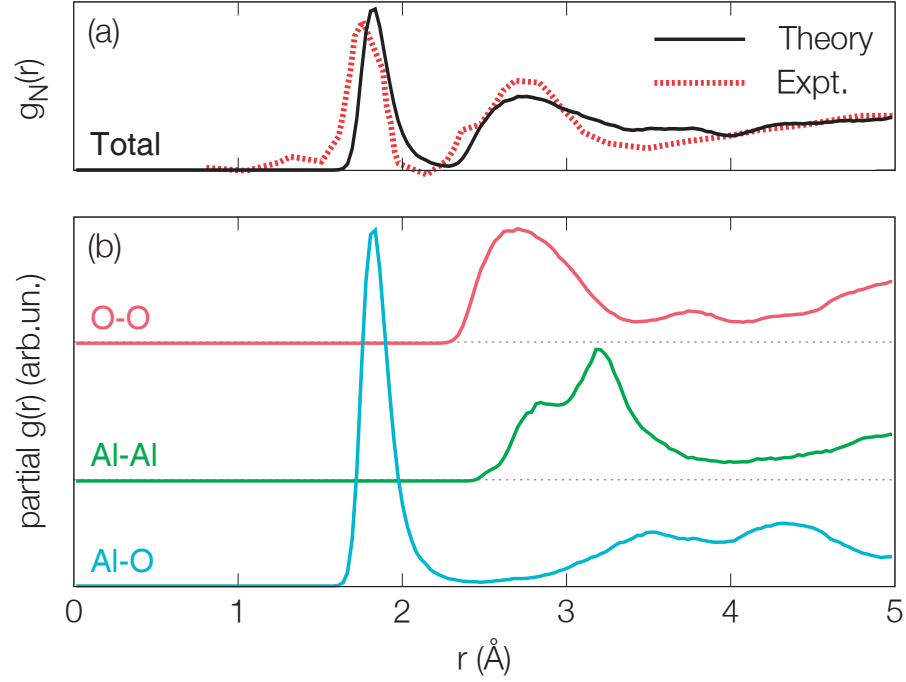


Figure 6.1 – (a) Total neutron radial distribution function of α -Al₂O₃ as calculated from a MD simulation at 300 K. The coherent neutron scattering lengths $b_{\text{Al}} = 0.3449 \times 10^{-4}$ Å and $b_{\text{O}} = 0.5803 \times 10^{-4}$ Å are used for Al and O, respectively [200]. Experimental data (red dotted line) are taken from Ref. [80]. (b) Radial distribution functions for O-O, Al-Al, and Al-O pairs.

by classical molecular dynamics [202]. Our amorphous model shows coexistence of AlO₄ and AlO₅ polyhedra with a small fractions of AlO₃ and AlO₆ structures. The average Al coordination number is 4.4, well within the experimental range (4.0–4.6) [79, 80, 81, 203]. The O atoms are mainly threefold coordinated, with the twofold and fourfold coordinations representing only 10% of the local O environment.

To achieve a good band offset, it is necessary that our hybrid functional calculations reproduce the band gap of α -Al₂O₃ [150]. However, there is a large experimental incertitude on the band gap of α -Al₂O₃, with measured values ranging between 6.1 and 7.0 eV [83, 84, 85, 86, 87, 88, 89, 90]. To determine the fraction of Fock exchange to be used in the hybrid functional, we thus turn to the α phase of crystalline Al₂O₃, for which the band gap at zero temperature is 9.13 eV [206]. The structure of the minimal cell of 30 atoms is first optimized at the PBE level. The structural parameters of the α phase, together with those of the κ phase considered for comparison, are found in good agreement with experiment (Table 6.1). Electronic-structure calculations at the HSE level then show that a fraction $\alpha = 0.45$ of Fock exchange needs to be considered to reproduce the experimental band gap of α -Al₂O₃. Application of the HSE functional defined by this value of the parameter α yields a band gap of 6.67 eV for our amorphous model of Al₂O₃, well within the experimental range and in agreement with several specific experimental estimates [86, 89, 90]. We also predict a band gap value of 8.10 eV for the κ phase of Al₂O₃, for which no experimental value is yet available. Calculated structural and electronic properties of the various oxide phases considered are compared to experiment in Table 6.1.

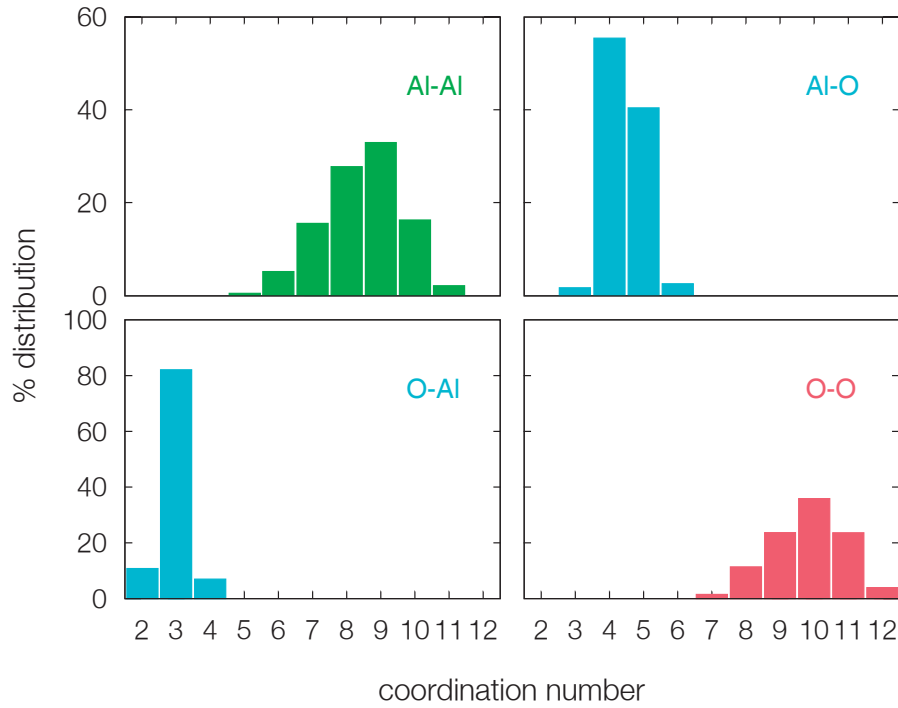


Figure 6.2 – Distribution of coordination number of Al and O atoms in α - Al_2O_3 as calculated in a MD simulation at 300 K. Average coordination numbers are $\text{CN}(\text{Al-Al})=8.4$, $\text{CN}(\text{Al-O})=4.4$, $\text{CN}(\text{O-Al})=3.0$, and $\text{CN}(\text{O-O})=9.8$.

It is of interest to compare the electronic density of states of our amorphous model of Al_2O_3 with those of the two crystalline phases (Fig. 6.3). The various band structures have been aligned through the average $2s$ level of twofold coordinated O atoms. We note that the band gap narrows going from α - Al_2O_3 to κ - Al_2O_3 and even more for our α - Al_2O_3 model. This narrowing of the band gap is seen to result mainly from a displacement of the conduction band. Indeed, the valence band maximum (VBM) of α - Al_2O_3 , of κ - Al_2O_3 and of our amorphous model of Al_2O_3 all line up within 0.3 eV, while the conduction band minimum (CBM) undergoes shifts up to ~ 2.1 eV. The relative position of the band edges of different phases of Al_2O_3 is experimentally not clearly established. Using internal photoemission, Afanas'ev *et al.* find that upon thermal crystallization of Al_2O_3 deposited on a Si substrate, the CBM only undergoes a small shift, whereas they infer a large shift for the VBM [207]. At variance, upon thermal crystallization of Al_2O_3 deposited on GaN, Toyoda *et al.* observe a bandgap variation due to the sole shift of the CBM [208]. Our results thus qualitatively favor the latter observations.

Band offset between GaAs and Al_2O_3

For determining the line-up of the band structures of GaAs and α - Al_2O_3 , we consider two atomistic model structures of the GaAs/ Al_2O_3 interface. The two interface models contain 227 atoms in a superlattice geometry and are derived from structures generated previously [113]. The two interface models differ by their chemical bonding, as shown in Fig. 6.4. Interface

6.1. Band alignment and chemical bonding at the GaAs/Al₂O₃ interface

Table 6.1 – Lattice parameters, mass density ρ , and band gap E_g of various phases of Al₂O₃: present theory vs experiment. For the crystalline phases, the experimental lattice parameters are taken from Refs. [204, 205]. The experimental band gap of α -Al₂O₃ is from Ref. [206]. For the amorphous, the experimental mass densities and band gaps are from Refs. [79, 80, 81] and Refs. [83, 84, 85, 86, 87, 88, 89, 90], respectively.

	a (Å)	b (Å)	c (Å)	ρ (g/cm ³)	E_g (eV)
α -Al ₂ O ₃					
Present theory	4.81		13.12	3.86	9.13
Expt.	4.76		12.99	3.98	9.13
κ -Al ₂ O ₃					
Present theory	4.88	8.41	9.03	3.64	8.10
Expt.	4.84	8.31	8.94	3.75	–
a -Al ₂ O ₃					
Present theory				3.31	6.67
Expt.				3.05–3.65	6.1–7.0

model I shows a GaAs substrate terminating with a Ga layer and is characterized by an interfacial layer of Ga–O chemical bonds [Fig. 6.4(a)]. At variance, the GaAs substrate in interface model II terminates with a layer of As atoms, resulting in the formation of As–Al chemical bonds at the interface [Fig. 6.4(b)]. Both models satisfy the electron counting rule which is expected to underlie the electronic properties of III-V semiconductors [111, 113]. More details concerning the interface structures are reported in Section 6.2. The interface calculations for determining the line-up between the reference levels are performed with a fraction of Fock exchange $\alpha = 0.45$, corresponding to the value used for Al₂O₃.² Combining the line-up calculations with the band-edge positions of the individual interface components results in calculated valence band offsets (VBOs) of 3.9 and 5.1 eV for interface models I and II, respectively.

When comparing to experimental data, it is convenient to focus on the VBO, as the VBM of Al₂O₃ only weakly depends on the oxide structure (cf. Fig. 6.3) and should thus be less sensitive to different growth conditions. Furthermore, it allows us to include among the experimental data results obtained for In_xGa_{1-x}As/Al₂O₃ interfaces [86, 89, 90], as the VBM has experimentally been found to be unaffected by variations in the In content [88]. With these caveats, measured values of the VBO range between 2.6 and 3.8 eV [86, 87, 88, 89, 90]. The calculated VBO of 3.9 eV for interface model I lies very close to the upper border of the experimental window, while the calculated VBO of 5.1 eV for interface model II lies higher by 1.3 eV than the highest measured value. This comparison favors an interfacial structure showing Ga–O chemical bonds and disfavors the occurrence of Al–As chemical bonds, in accord with a recent interpretation of As $2p$ X-ray photoemission spectra [118]. In Fig. 6.5, the available experimental data are superposed to the band alignment determined for interface model I. Two groups of experimental data can be distinguished, those obtained by XPS [86,

²The value $\alpha = 0.35$, used for GaAs, would affect the calculated offsets by less than 6 meV after that the shift of 0.90 eV in the reference O 2s level is consistently accounted for.

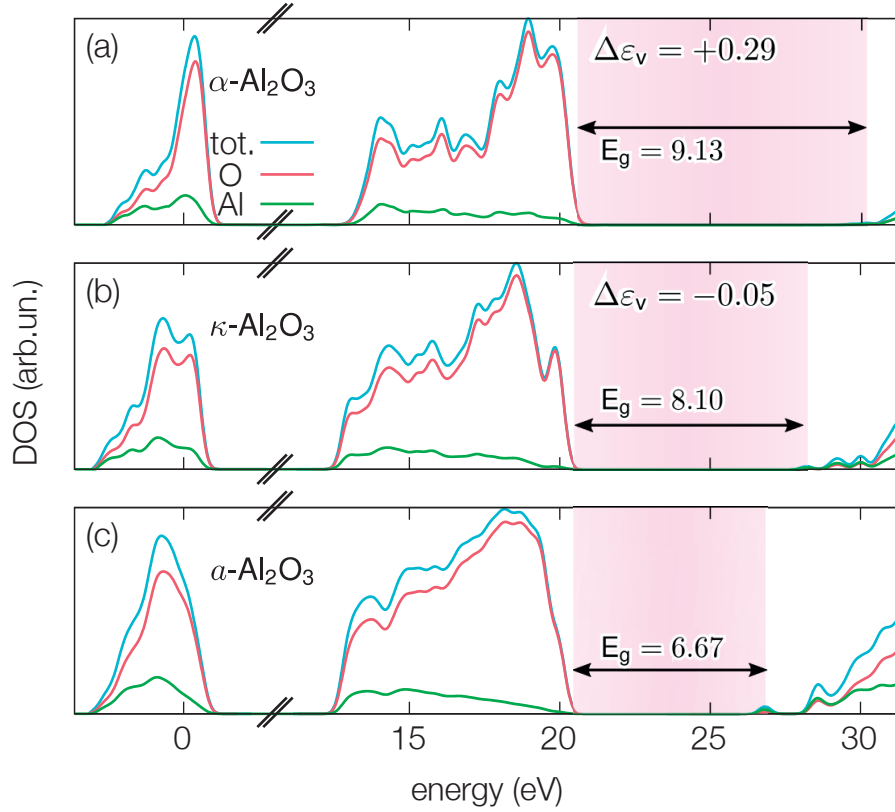


Figure 6.3 – Total electronic density of states and projection on O and Al atoms, as obtained from a HSE functional calculation with the fraction of Fock exchange set to 0.45 for (a) α - Al_2O_3 , (b) κ - Al_2O_3 , and (c) a - Al_2O_3 . The energies are referred to the average $2s$ level of the twofold coordinated O atoms, which is used for the alignment. A Gaussian broadening of width 0.2 eV is applied. The band gaps and the misalignment $\Delta\epsilon_v$ of the valence band with respect the amorphous in panel (c) are also reported.

89, 90] and those obtained by internal photoemission (IPE) [87, 88]. The comparison in Fig. 6.5 shows excellent agreement between theory and the XPS experiments [86, 89, 90]. Most noticeably, the agreement does not only concern the VBO but the full band structure at the interface. At variance the IPE experiments yield smaller VBOs (2.6–2.8 eV) [87, 88], resulting in band alignments in which the Al_2O_3 band gap is shifted to higher values by about 1.0–1.2 eV.

The characterization of GaAs/oxide interfaces has demonstrated high densities of defect states [95, 98, 99, 103]. In particular, XPS experiments on As $2p$ core levels show a concentration of 10^{13} sites/ cm^2 of As atoms involved in As–As linkages [96, 118]. We here address whether defect densities in such concentrations could affect the band alignment. We consider two variations of interface model I incorporating either As–As dimers [113] or As antisites [106], and calculate the corresponding VBOs. Assuming a linear relation between the defect density and the band offset, we then rescale the calculated VBOs to reflect a defect density of 10^{13} sites/ cm^2 . The VBO variations induced by As–As dimers and As antisites amount to 0.01 and 0.02 eV, respectively. These results clearly show that interfacial As-related defects do not affect

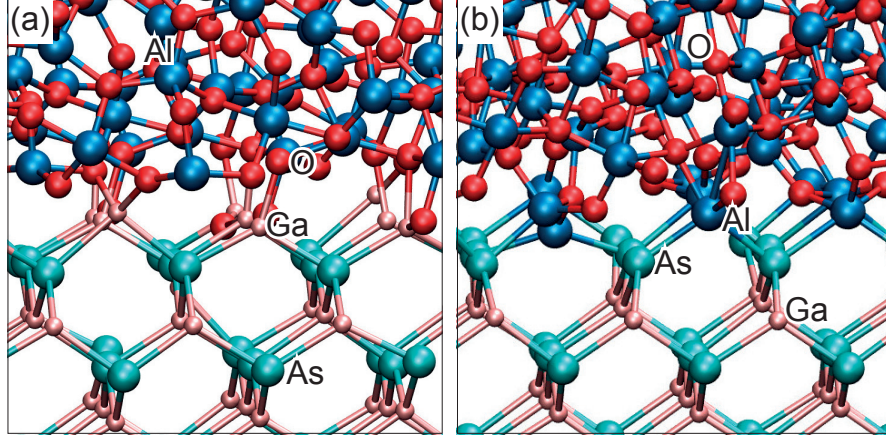


Figure 6.4 – Relaxed structures of the GaAs/Al₂O₃ interface: (a) model I and (b) model II.

the band alignment in any significant way.

6.2 Defects at the GaAs/Al₂O₃ interface

The interpretation of the experimental characterization of Fermi-level pinning at GaAs/oxide interfaces is not trivial. Unpinned GaAs/oxide interfaces have been realized through molecular beam epitaxy and the use of specific oxides [63, 66]. However, when the technologically preferred atomic layer deposition technique is used [77], the interface defect density is unsatisfactorily high [99], showing minor peaks in the vicinity of the band edges and a significant mid-gap peak [103, 104]. The minor peaks can be associated to isolated dangling-bond states [109, 115] or to antibonding states of the As-As dimer [105, 111, 113, 115]. For the mid-gap peak, there are both experimental [106] and theoretical [117, 118] indications which favor the As antisite defect. The assignment to this defect appears consistent with the As enrichment observed at the interface [106] and in the near-interface oxide [74, 77, 97, 189]. Furthermore, recent experiments have shown that using Ga-rich reconstructed GaAs surfaces results in a significant reduction of the mid-gap peak and in improved device performance [104].

Computational Details

Structural and electronic properties of defects at the interface are computed at the PBE level and aligned to the HSE band gap as described in Section 2.2. We rely on the use of a semilocal functional because of the size of our interface models which makes the use of hybrid functional a very demanding procedure. Indeed, in the direction perpendicular to the interface the supercell size is twice as large as that used for bulk defects. This allows us to sample the Brillouin zone through a $2 \times 2 \times 1$ \mathbf{k} -point mesh which results in the same \mathbf{k} -point density as in the bulk calculations³ (cf. Section 2.2).

³In this case, it was unnecessary to resort to an off-center \mathbf{k} -point mesh as the gap is opened through the quantum confinement effect.

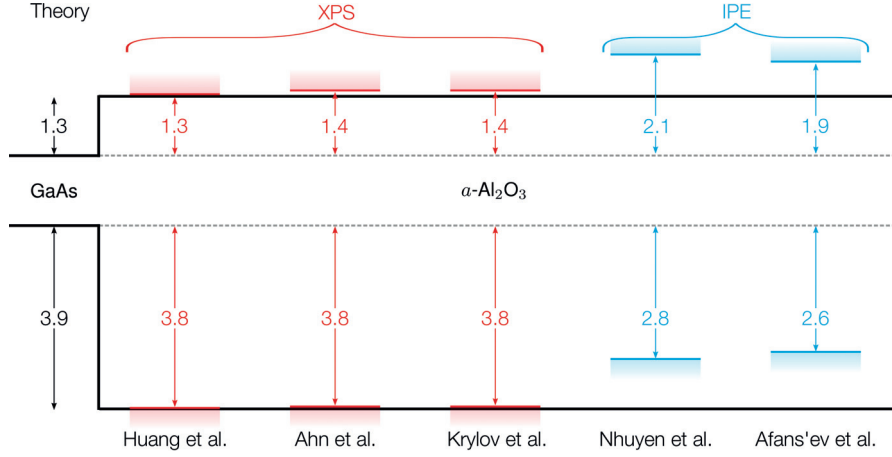


Figure 6.5 – Band alignment at the GaAs/ Al_2O_3 interface as obtained for interface model I. The calculated results are compared with different experimental determinations, achieved through XPS (Refs. [86, 89, 90]) and IPE (Refs. [87, 88]).

The alignment procedure with the HSE band gap follows the procedure described in Section 2.2. The application of this alignment scheme relies on a sufficiently large band gap at the PBE level. In our interface calculations, this condition is achieved as a consequence of the quantum-confinement effect associated to GaAs slab calculation. To correctly compare the formation energy of defects modeled at the interface and in the bulk, we ensure the same level of theory for the two studies. For this reason, in the following results, we report formation energies of bulk defects calculated at the PBE level and aligned to the HSE band gap. We stress that in these calculations, a large band gap is achieved through the use of an off-center \mathbf{k} -point mesh.

To estimate the accuracy of our alignment scheme applied to interfacial defects, we consider the As–As dimer/DB defect at the GaAs/ Al_2O_3 interface and compare the calculated charge transition level with the corresponding value obtained optimizing the electronic structure at the HSE level. First, we note that within the PBE functional, the use of the sole Γ point gives converged defect structures and charge transition levels. Then we perform HSE calculations of the As–As dimer/DB stable states, obtaining for the calculated charge transition level the same position within 0.02 eV. Hence, the use of the PBE functional does not lead to any significant loss of accuracy but represents a noticeable speed-up with respect to full HSE calculations.

Defects at the interface: parent interface models

For the study of defects at the interface between GaAs and Al_2O_3 , we adapt interface models from previous studies [113, 118]. In particular, the defect properties are studied using two parent model structures of the GaAs/ Al_2O_3 interface (see Fig. 6.6). The original models have undergone full structural relaxation upon minor modifications ensuring that the semiconductor-oxide interface is characterized by Ga–O bonds, as suggested from the calculation of valence band offsets (cf. Section 6.1) and the interpretation of As $2p$ core-level

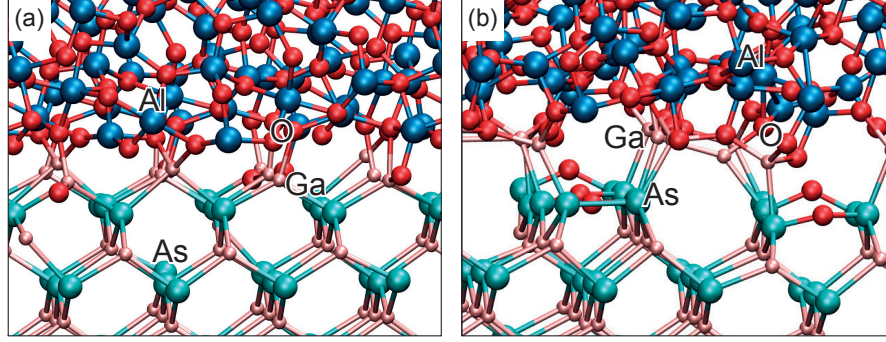


Figure 6.6 – Atomic structures of two parent GaAs/Al₂O₃ interface models considered in this study: (a) model I and (b) model I'. Model I' contains an interfacial As–As dimer which is shown in the foreground in (b).

spectra [118].

Model I corresponds to the interface used for the band alignment in Section 6.1. This model consists of 227-atom in a tetrahedral supercell and is shown in Fig. 6.6(a). The repeat interface unit in the direction parallel to the interface contains 8 interface atoms of GaAs. The oxide structure is derived from the κ phase of crystalline Al₂O₃ which shows a mass density and atomic coordinations similar to those of amorphous alumina grown through atomic layer deposition [190]. The interface pattern is obtained by superimposing κ -Al₂O₃(011) to GaAs(001) and allowing for small lateral strains.

Model I' has been designed to model the As–As dimer/DB defect [113]. Model I' is obtained from model I by displacing the oxide slab and the interfacial Ga layer along the [110] direction until the Ga atoms lie atop of the As atoms. Upon structural relaxation, the interfacial Ga and As atoms then form an equal number of As–As and Ga–Ga dimers. Oxygen atoms are subsequently inserted in the dimer bonds until a single As–As dimer remains, as shown in Fig. 6.6(b).

It is important to remark that the structures in both model I and model I' satisfy the electron counting-rule.

Bulk-like defects and interfacial defects

Focusing on the occurrence of defects in the vicinity of the interface, we differentiate between two types of defects. The first type of defects have corresponding isolated defects in the bulk and their sole difference is their proximity to the interface. We refer to these defects as *bulk-like defects*. This set includes the As_{Ga} defect, the (As_{Ga})₂-O_{As} defect, and the V_{As}-2 As_{Ga} defect complex. These defects are here modeled at interface model I. In this case the defect-free interface can be taken as reference in order to define the defect formation energy as described in eq. (2.7).

Next, we also consider another type of defects which does not have corresponding bulk defects.

These defects are peculiar to GaAs terminations such as surfaces or interfaces. We refer to this type of defects as to *interfacial defects*. Defects considered here and belonging to this type are the Ga DB, the As DB, and the As–As dimer/DB defect. Such defects generally require specific models such as interface model I'. When such defects are created within periodic defect-free structures, the periodicity is interrupted and can be restored only through the introduction of secondary defective structural units. The absence of a defect-free reference system which differs from the defect only by the appearance of the defect itself prevents the definition of absolute formation energies. For these defects, only relative formation energies of different charge states can be calculated.

The secondary structural units formed upon the creation of such defects in priorly defect-free systems may not satisfy locally the electron counting rule and thus carry a charge q' . For instance, in interface model I', the formation of the As–As dimer occurs in combination with the formation of the interfacial Ga–O–Ga and As–O–As structures. When the local charges are defined through electron counting arguments, the As–As dimer is in a charge state $q = 0.5$, while the Ga–O–Ga and As–O–As structures carry a compensating charge of $q' = -0.5$. From this reasoning it follows that the charge of the supercell Q does not necessarily correspond to the charge q carried by the defect of interest. Indeed, the total supercell charge Q corresponds to the sum of all local charges in the supercell, namely the sum of the defect charge q and of the charge q' of the secondary structural units. Moreover, in order to study the energy levels of the defect of interest, it is a necessary condition that upon charging the secondary structural units remain electrically inactive, i.e. that their charge q' does not vary. For this reason, we inserted O atoms into all homopolar bonds but one in the generation of interface model I'.

For the electronic properties of interfacial defects, we follow a two-step procedure. First, we obtain the defect energy ΔE^Q corresponding to the supercell with charge Q :

$$\Delta E^Q = E_{\text{tot}}^Q + E_{\text{corr}}^Q - E_{\text{ref}} + Q\epsilon_F, \quad (6.1)$$

where E_{tot}^Q is the total energy of the supercell and E_{corr}^Q the finite-size correction as it appears in eq. (2.7). As discussed, only the relative defect energies are accessible and a constant reference energy E_{ref} remains undefined. For simplicity, we fix E_{ref} such that the defect energy ΔE^Q vanishes for $\epsilon_F = \epsilon_v$. Any secondary structural units do not undergo any charge transition for Fermi energies within the band gap. Thus, their energy as function of ϵ_F shows a linear dependence with a slope defined by their charge q' . To the extent that q - q' interactions are negligible, it is then possible to obtain the defect energy ΔE^q pertaining to the sole defect of interest through the following subtraction

$$\Delta E^q = \Delta E^Q - q'\epsilon_F. \quad (6.2)$$

The relative defect energies obtained in this way are sufficient for determining the defect charge transition levels. However, in absence of absolute formation energies, it is not possible to establish any link with the defect abundances at thermodynamic equilibrium.

In order to illustrate the calculation of charge transition levels through this procedure, we consider an Al DB defect in a 64-atom bulk supercell of AlAs at the PBE level.⁴ We focus on AlAs

⁴The Brillouin is sampled at the Γ point; other computational parameters are taken as in Ref. [109]. For the

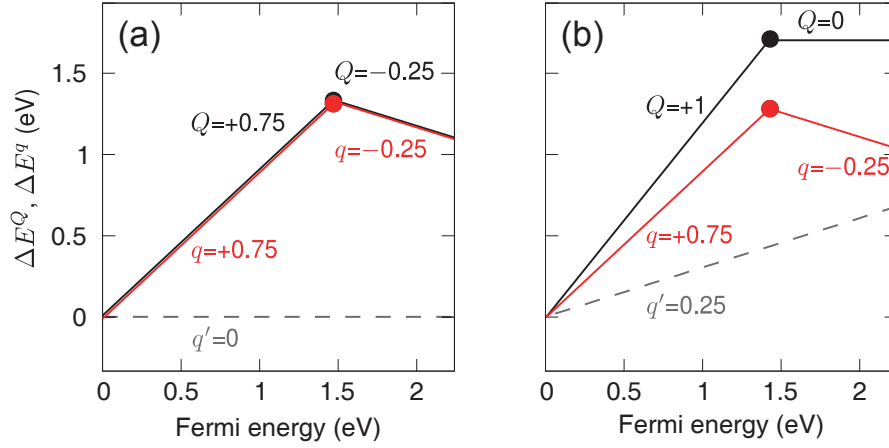


Figure 6.7 – Defect energy of an interfacial Al DB defect in bulk AlAs with different secondary structural units: (a) pseudo-H atoms saturate the As DBs in the cavity leading to neutral secondary structural units ($q'=0$), (b) one of the pseudo-H is replaced by a regular hydrogen atom leading to $q'=0.25$.

rather than on GaAs because the large band gap of AlAs encloses the DB defect levels already at the PBE level [109], while AlAs is equivalent to GaAs from the electron counting point of view. To generate the Al DB model, a cavity is created in the bulk structure by removing four atoms (one As and 3 Al atoms). All the undesired As DBs are then saturated with pseudo-H atoms carrying 3/4 electrons [209]. In this model, the pseudo-H represent the secondary structural units which are required to restore the bulk periodicity. These structures locally satisfy the electron counting rule leading to $q' = 0$ and $Q = q$. We consider the charge transition between the empty and the singly occupied DB, corresponding to charged calculations in which $Q = q = +0.75$ and $Q = q = -0.25$, respectively. In this case, the defect energies ΔE^Q and ΔE^q coincide, as shown in Fig. 6.7(a), where the energy scale is referenced with respect to the defect energy at the VBM. The charge transition level is found at 1.48 eV above the VBM.

To examine the possible role of q - q' interactions, it is interesting to note that the charge transition level calculated above closely agrees with the result of 1.37 eV obtained in Ref. [109] with different secondary structural units, namely a 6-atom cavity (3 As and 3 Al atoms) and a saturation with regular H atoms. To further explore such effects, we replace one pseudo-^{0.75}H with a regular H atom and repeat the calculations for the Al DB. Since the H-As bond releases 1/4 electrons to locally fulfill the electron counting rule, this modification leads to charged secondary units with $q' = +0.25$. Hence, the singly occupied DB ($q = -0.25$) in this setup corresponds to a neutral supercell with $Q = 0$, while the empty DB is achieved with a supercell charge of $Q = +1$. The corresponding defect energies ΔE^Q and ΔE^q are shown in Fig. 6.7(b). By comparing the two panels in Fig. 6.7, one notices that ΔE^Q substantially depends on the choice of secondary units, while ΔE^q barely changes and thus reliably reflects the properties of the defect of interest. Indeed, the charge transition level calculated within the two approaches differs by only 0.06 eV. This difference might be taken as an estimate of the effect of the neglected q - q' interactions in this case.

finite-size corrections we use the experimental value of the dielectric constant ($\epsilon=10.06$, Ref. [181]).

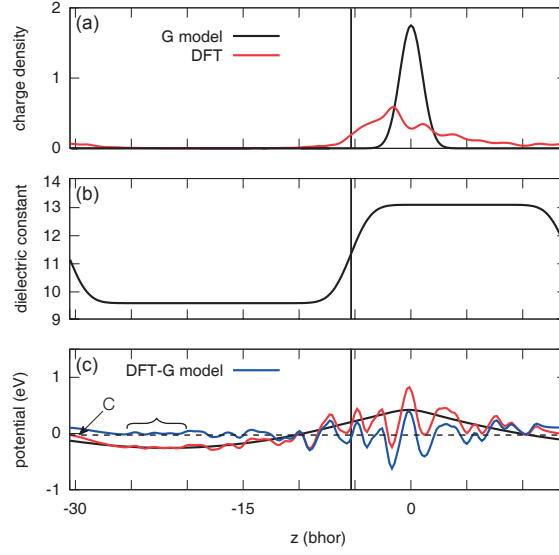


Figure 6.8 – (a) Planar-averaged distributions of the Gaussian model charge (G model, black line) and of the As_{Ga} defect charge in the +2 charge state as found in a DFT calculation at the PBE level (red line). The defect is located at the origin and the interface is visualized through a vertical line. (b) Dielectric constant profile across the interface as used in the present work. (c) Planar averages of the DFT-PBE electrostatic potential obtained as difference between the potentials of the +2 charged and the neutral As_{Ga} defect. The blue line represents the short-ranged defect potential and is obtained as the difference between the red and the black lines. The accolade indicates a region far from the defect in which the short-ranged potential is found to be constant.

Estimating the size of the q - q' interactions in general might not be trivial and is expected to depend on the size of the charge q' and on its location with respect to the defect charge q . In the case of the As-As dimer/DB defect, an extreme case has been considered corresponding to the addition of a Mg^{2+} ion among the secondary structural units (c.f. Section 6.2.2). Nonetheless, the charge transition level of the defect under investigation is found to shift by less than 0.2 eV. Such an error still does not exceed typical uncertainties associated to density functional calculations [160].

Finite-size corrections

The finite-size corrections applied to defects located close to the interface are calculated through the scheme described in Section 2.5 and derived in Ref. [171]. We model the defect charge through a Gaussian distribution with a width of 1 bohr [Fig. 6.8(a)] and we describe the dielectric-constant profile through an error function with a smoothness parameter of 2 bohr [Fig. 6.8(b)]. For the bulk dielectric constants of GaAs and Al_2O_3 , we use experimental values of 13.1 (Ref. [181]) and 9.6 (Ref. [210]), respectively. The size of the largest finite-size corrections obtained in this work are of the order of 0.2–0.4 eV for defects in the charge states ± 2 . The detailed parameters defining the dielectric-constant profile are not critical. For

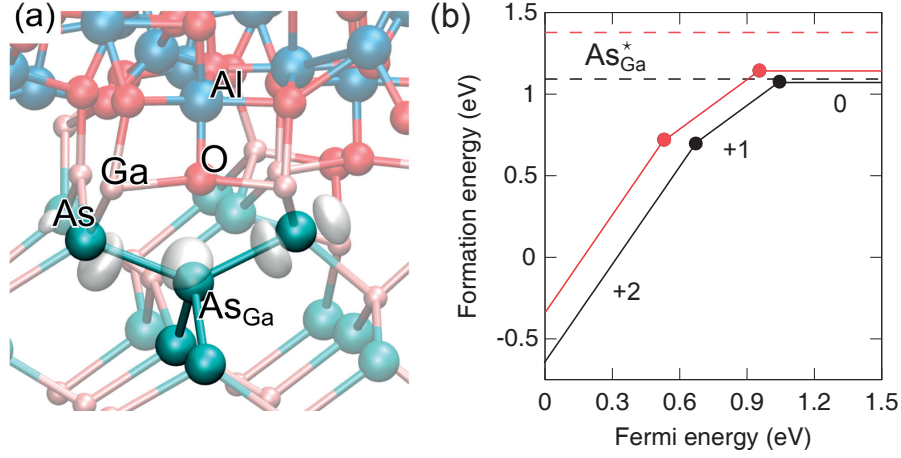


Figure 6.9 – (a) Relaxed structure of the As_{Ga} defect in the stable neutral charge state. The charge density of the defect state is shown in transparency. (b) Formation energy vs Fermi energy for the As_{Ga} defect as obtained through the use of model I of the GaAs/Al₂O₃ interface (black lines) and of a bulk model (red lines). The dashed lines correspond to the energy of the corresponding As_{Ga}^{*} defects. As-rich conditions are assumed.

instance, using theoretical dielectric constants or any other smoothness parameter ranging between 0.5 bohr and 4 bohr affects the corrections by less than 20 meV. The electrostatic potential generated by the Gaussian charge reproduces well the DFT potential obtained from the difference between the defect potentials in the charged and neutral charge states [Fig. 6.8(c)]. The resulting short-range potential is obtained from the difference of the DFT and the model potential and shows a flat behavior far from the defect, thereby ensuring that the defect charge distribution is well localized. The constant C added to this potential in order to make it vanish in between two defects corresponds to the alignment term of the finite-size correction.

6.2.1 Bulk-like defects

As_{Ga} defect

We model the As_{Ga} in the first Ga layer on the GaAs side of interface model I, as shown in Fig. 6.9(a) for the neutral defect charge state. In the bulk, the As_{Ga} defect is stable in the neutral, the singly positive, and the doubly positive charge states (cf. Chapter 3). The neutral charge state exhibits a metastability which has been associated to the EL2 defect [29, 211]. The metastable configuration (As_{Ga}^{*}) shows the As antisite atom occupying a C_{3v} position upon the breaking of one As–As bond and the relaxation to a nearby interstitial site. Application of the electron counting rule [111] reveals that the neutral As_{Ga} possesses two electrons in excess. In the stable neutral charge state, the two electrons are delocalized over the antisite atom and its As–As bonds, while they are localized in two doubly occupied As DBs in the metastable configuration.

Here, we consider the three stable charge states and the neutral metastable state for a location

of the antisite in proximity of the interface. In the most stable neutral state, there is a small departure from the tetrahedral symmetry. The bond length of the As–As bonds pointing to the Al_2O_3 component of the interface are $\sim 2.59 \text{ \AA}$, 0.07 \AA longer than those pointing to the GaAs component of the interface ($\sim 2.52 \text{ \AA}$). From the inspection of the defect charge density given in Fig. 6.9(a), we note that the structural asymmetry is associated with a preferential electron localization on the As atoms located closer to the interface. This can be understood by the attraction exerted by the highly polar Ga–O bonds at the interface. In the positive charge states, the As–As bond lengths become shorter and the overall structure of the defect core shows smaller deviations from tetrahedral symmetry. In particular, in the +2 charge state, the As–As bond lengths are $\sim 2.47 \text{ \AA}$ on the GaAs side and $\sim 2.48 \text{ \AA}$ on the oxide side.

The As_{Ga}^* configuration at the interface can be generated by breaking an As–As bond either on the semiconductor side of the antisite or on the oxide side of the antisite. In both cases the As_{Ga}^* configuration is higher in energy than the near-tetrahedral As_{Ga} . When the bond breaking occurs on the semiconductor side the metastable As_{Ga}^* is higher in energy by only 0.02 eV , whereas the bond breaking on the oxide side yields a metastable As_{Ga}^* at 0.23 eV , not far from the value of 0.24 eV found for a location in the bulk. This indicates that the As_{Ga}^* configuration with a bond breaking on the semiconductor side is stabilized at the interface. This effect can be assigned to the more significant backward relaxation of the antisite atom for displacement towards the oxide. In its most stable configuration, the As_{Ga}^* defect shows an average As–As bond length of 2.48 \AA while the distance between the two As atoms carrying a doubly occupied DB is 3.52 \AA .

The formation energies vs. Fermi energy for the stable charge states of the As_{Ga} defect are given in Fig. 6.9(b). The antisite defect shows a double-donor behavior, in which the neutral, the singly positive, and the doubly positive charge states are the most stable ones. The $\varepsilon_{+2/+1}$ and $\varepsilon_{+1/0}$ charge transition levels lie at 0.67 eV and 1.04 eV above the GaAs VBM. In this calculation, the finite-size corrections applied to the defect formation energies amount to 0.10 eV and 0.40 eV for the +1 and +2 charge states, respectively. For comparison, Fig. 6.9(b) also shows our calculated formation energies for the As_{Ga} in the bulk, which yield defect levels at 0.51 and 0.91 eV above the VBM. Our bulk results agree well with those reported in Chapter 3. The comparison shows that the defect levels of the As_{Ga} shift by only 0.15 eV to higher energies when the defect is located close to the interface, suggesting that the electrical properties remain similar. However, the defect formation energies in the positive charge states are lower. In particular, for p -type conditions, the formation energy decreases by $\sim 0.45 \text{ eV}$, suggesting that the defect incorporation is facilitated at the interface.

Recent electron spin resonance experiments have provided support for the occurrence of As_{Ga} antisite defects at GaAs/oxide interfaces [106]. Furthermore, specific features in the As $2p$ core-level spectra [97] can be assigned to the As_{Ga} antisite [118]. Therefore, this defect has often been proposed for being responsible of the mid-gap peak in the experimental density of interface states [106, 117, 118]. Density-of-states measurements have reported the occurrence of two midgap peaks, one of donor-like states at 0.5 eV and one of acceptor-like states at 0.9 eV above the VBM [76, 103]. Other measurements on interfaces grown in As-rich conditions report the presence of a single midgap peak at 0.7 eV above the VBM [104]. Such density-of-states experiments are subject to incertitudes of 0.2 eV due to estimates of defect cross-sections [103], and thus prevent any conclusive statement concerning the number of peaks. Nevertheless,

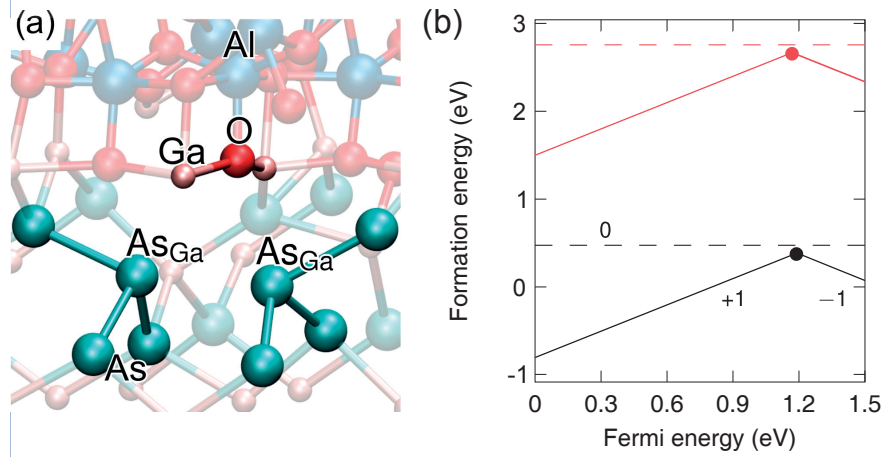


Figure 6.10 – (a) Relaxed structure of the $(\text{As}_{\text{Ga}})_2\text{-O}_{\text{As}}$ defect in the metastable neutral charge state. (b) Formation energy of the $(\text{As}_{\text{Ga}})_2\text{-O}_{\text{As}}$ defect vs Fermi energy as obtained through the use of model I of the GaAs/Al₂O₃ interface (black lines) and of a bulk model (red lines). The bulk result is obtained from the defect structures described in Section 4, but the electronic structure is here obtained at the PBE level. As-rich conditions are assumed.

most of these observations are compatible with the As_{Ga} defect. This defect introduces defect levels in the midgap region of the GaAs band gap and is consistent with the As enrichment observed at the interface [74, 77, 97, 106, 189]. However, it acts as a double donor and therefore it completely lacks the acceptor-like behavior observed experimentally [76]. Moreover, because of its donor properties, the occurrence of sole As antisite defects cannot stabilize the Fermi level without the participation of an acceptor-like defect [126]. Thus, despite clear experimental evidence supporting the occurrence of As_{Ga} antisites at the GaAs/oxide interfaces [106], these defects cannot trivially account for the observed Fermi-level pinning.

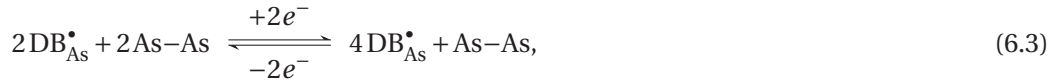
$(\text{As}_{\text{Ga}})_2\text{-O}_{\text{As}}$ defect

The $(\text{As}_{\text{Ga}})_2\text{-O}_{\text{As}}$ defect is composed of two As antisite defects, which are nearest neighbors in the Ga sublattice and separated by an As vacancy, in which an O atom is captured. The relaxed structure at the interface is shown in Fig. 6.10(a). In bulk GaAs, this defect is stable in the singly positive and singly negative charge states, while it is metastable in the neutral charge state. The amphoteric behavior of this defect accounts for the Fermi-level pinning in oxygen-doped GaAs, with the calculated +1/−1 charge transition level in excellent agreement with the measured position of the pinned Fermi energy [31, 33] (cf. Chapter 4).

In proximity of the interface, this defect shows many similarities with its bulk counterpart. The stable charge states are still the +1 and −1 charge states, both satisfying the electron counting rule. In the +1 charge state, each of the two As antisite atoms forms three As–As bonds and one As DB leading to an overall release of 3/2 electrons, which account for the saturation of the Ga–O–Ga unit. The As–As bond lengths are 2.49 ± 0.01 Å and the distance between the

As antisite atoms is 3.61 Å. The O atom is threefold coordinated forming two Ga–O bonds of ~1.9 Å and one Al–O bond of 1.82 Å. Upon electron capture, the defect structure undergoes structural rearrangements which mostly involve the As atoms of the defect core, in analogy to the defect behavior in the bulk. In the –1 charge state, the two antisite atoms move closer and form a bond, while each of them breaks one of its As–As backbonds giving four doubly occupied DBs in total. In this configuration, the average As–As bond length is 2.52 Å and the As_{Ga}–As_{Ga} bond length is 2.70 Å, while the structural unit involving the O atom undergoes minimal variations. In the neutral charge state, the defect structure is similar to that of –1 defect state, with the As_{Ga}–As_{Ga} being only singly occupied.

The transformation of the defect structure from the +1 to the –1 charge state only involves the defect As atoms, leaving the Al–O–Ga₂ unit unchanged. The capture of two electrons can thus be expressed as:



which can be simplified to give:



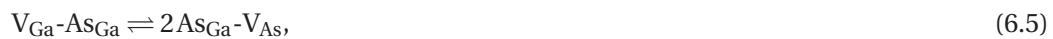
This reaction thus corresponds to an As–As dimer breaking up into two opposite doubly occupied As DBs.

The formation energies of the (As_{Ga})₂-O_{As} defect are shown as a function of the Fermi energy in Fig. 6.10(b). Calculated finite-size correction energies are about 0.1 eV for both the positive and the negative charge state. The amphoteric behavior of the defect could lead to Fermi-level pinning at the +1/–1 charge transition, found at 1.19 eV above the GaAs VBM. Compared to the same defect in the bulk [cf. Fig. 6.10(b)], the defect level shifts by only 0.05 eV towards higher energy. However, the formation energy drops by more than ~2 eV, suggesting that the flexible bond pattern at the interface facilitates the incorporation of this defect complex.

In correspondence of the calculated defect level, the experimental density of interface states shows a small peak to which an acceptor character has been associated [76]. This measurement has been done using a *n*-type capacitor and is thus not sensitive to a possible donor-like behavior of the defect. The (As_{Ga})₂-O_{As} defect can thus not be ruled out as possible origin of the defect states lying close to conduction band minimum.

V_{Ga}-As_{Ga}/V_{As}-2 As_{Ga} defect complex

As described in Chapter 3 the V_{Ga}-As_{Ga}/V_{As}-2 As_{Ga} defect complex has two different stable forms. The V_{Ga}-As_{Ga} form results from the binding of a V_{Ga} and a As_{Ga}. This form of the defect can then transform to the V_{As}-2 As_{Ga} form via the displacement of one As atom neighboring the gallium vacancy into V_{Ga}:



being the same transformation which occurs to the corresponding bulk defect [cf. Eq. 3.7]. In the bulk, this defect is amphoteric and bistable as the structure on the left hand side is

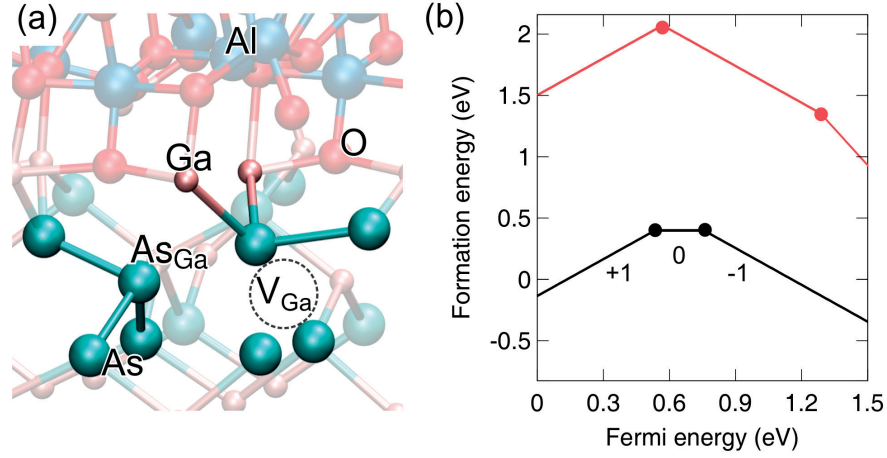


Figure 6.11 – (a) Relaxed structure of the distorted $V_{\text{Ga}}\text{-As}_{\text{Ga}}$ defect in the charge state -1 . (b) Formation energy of the $V_{\text{Ga}}\text{-As}_{\text{Ga}}/V_{\text{As}}\text{-2As}_{\text{Ga}}$ defect complex vs Fermi energy as obtained through the use of model I of the GaAs/Al₂O₃ interface (black lines) and of a bulk model (red lines). As-rich conditions are assumed.

stable in negative charge states and spontaneously transforms into the structure on the right hand side in positive charge states. This defect complex is invoked in order to explain the Fermi-level pinning observed in highly irradiated GaAs.

We here study the $V_{\text{As}}\text{-2As}_{\text{Ga}}$ defect complex in the proximity of the GaAs/oxide interface. This form is found to be stable in the charge state $+1$. Its structure closely resembles the $(\text{As}_{\text{Ga}})_2\text{-O}_{\text{As}}$ defect but lacks the O atom saturating the Ga DBs. The electron counting rule is satisfied by the formation of a stretched Ga–Ga bond which captures the $1/2$ electrons released by the As–As bonds formed by the two As antisites. The addition of one electron leads to a distorted form of the $V_{\text{Ga}}\text{-As}_{\text{Ga}}$ defect, which is then essentially maintained in the charge states -1 . The presence of the interface favors a distortion by which one of the As atoms neighboring the As_{Ga} forms a bond to an As atom of the network rather than to the As_{Ga} , as shown in Fig. 6.11(a) for the -1 charge state. From the electronic point of view, this atomic configuration does not differ from the bulk form of the $V_{\text{Ga}}\text{-As}_{\text{Ga}}$ defect, as it shows the same amount of As–As bonds and As DBs. Accordingly, the electron counting rule is satisfied in this charge state.

The formation energies vs. Fermi energy for these defect complexes are shown in Fig. 6.11(b). Calculated finite-size correction energies amount to 0.10 eV for the singly positive and negative charge states. It is remarkable to point out that this defect complex undergoes strong stabilization in proximity of the interface, with a reduction of the formation energies between 1.66 (in p -type conditions) and 1.29 eV (in n -type conditions) with respect to corresponding bulk values. This confers strong stability to this defect even compared to the interfacial As_{Ga} : in p -type conditions the formation energies differ by less than 0.2 eV, but the $V_{\text{Ga}}\text{-As}_{\text{Ga}}$ defect complex is more stable than the As_{Ga} by as much as 1.43 eV in n -type conditions. The overall electronic behavior of the defect complex at the interface differs from that of its bulk counterpart insofar the -2 charge state is no longer found to be stable at the interface. The $+1/-1$ defect level of the interface defect is found at 0.65 eV above the GaAs

VBM, close to the respective value for the bulk defect at 0.55 eV. Unlike for the bulk defect, we find that the neutral charge state of the interface defect is stable in a narrow range of Fermi energies, between 0.53 and 0.76 eV above the GaAs VBM.

The dominant structural rearrangements involved in the charge capture/release process underlying the amphoteric behavior of this defect can be best rationalized by considering the +1 and the −1 defect states where the electron counting rule is perfectly satisfied. The process can be described by the combination of two net reactions. The first one corresponds to the bistability of the As dimer/DB defect and is electrically active:



while the second reaction represents the suppression of homopolar bonds in favor of regular Ga-As bonds without any electron transfer:



For the $V_{\text{Ga-AsGa}}/V_{\text{As-2AsGa}}$ defect complex, the +1/−1 charge transition occurs at about 0.6 eV above the GaAs VBM for both the interface and bulk defect. However, the charge transition level of the $(\text{AsGa})_2\text{-O}_{\text{As}}$ defect which is also governed by Eq. (6.6) occurs at much higher energies, namely at 1.19 eV above the GaAs VBM. We explain this behavior through Eq. (6.7) which energetically favors the right-hand side of the reaction. This stabilizes the negative defect state with respect to the positive one, and thus results in a lower defect level.

The amphoteric nature of the defect complex drives the Fermi-level towards midgap, where the neutral charge state of the interface defect is stable. The +1/0 and 0/−1 defect levels fall close to the midgap peaks in the experimental D_{it} [76, 103, 104]. The +1/0 and 0/−1 defect levels show donor-like and acceptor-like behavior, respectively, in accord with actual observations [76]. These defect levels thus show overall consistency with the midgap peaks in the D_{it} .

6.2.2 Interfacial defects

Ga DB defect

A subsurface Ga dangling bond is modeled at the GaAs/Al₂O₃ interface through the formation of a cavity in model I of the GaAs/Al₂O₃ interface, as shown in Fig. 6.12(a). After removing an interfacial As atom and a subsurface Ga atom, we saturate the undesired DBs with H atoms making sure that the electron counting rule is satisfied, in a similar way as described in Ref. [115]. Indeed, the three created H-As bonds release 3/4 electrons, while the two Ga-H bonds capture 2/4 electrons. The remaining 1/4 electrons are captured by the Ga DB which then becomes singly occupied in the neutral supercell ($Q = 0$). In this defect configuration, the defect charge is $q = -1/4$ and the secondary structural units carry a charge of $q' = 1/4$. We also consider the unoccupied dangling bond, with a defect charge of $q = +0.75$ and a supercell charge of $Q = +1$.

Upon charging the dangling bond, the defect charge changes sign going from $q = +0.75$ in the unoccupied state to $q = -0.25$ in the singly occupied state. This clearly reveals the amphoteric nature of the Ga DB defect. In the singly occupied state, the average Ga-As bond length formed

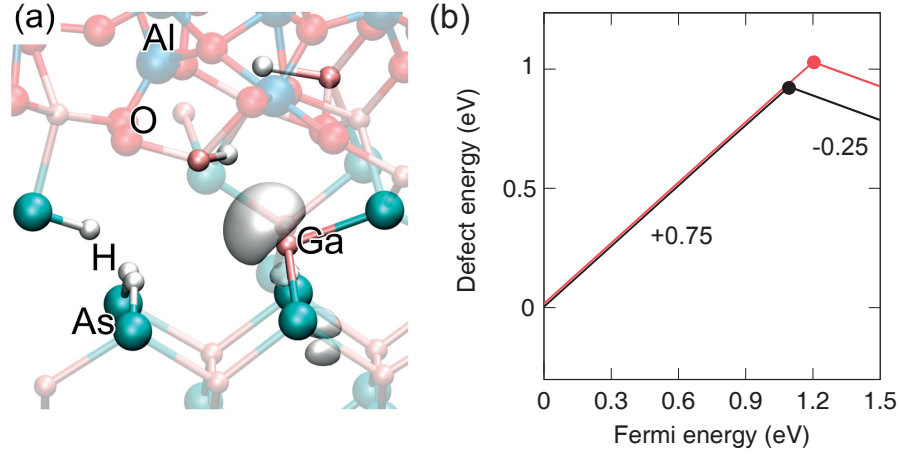


Figure 6.12 – (a) Relaxed structure of the Ga DB defect at the GaAs/Al₂O₃ interface. The charge density of the singly occupied defect state is shown in transparency. (b) Defect energy of the Ga DB defect as obtained through the use of model I of the GaAs/Al₂O₃ interface (black lines) and of a bulk model (from Ref. [109], red lines).

by the Ga atom carrying the dangling bond is 2.48 Å, very close to the bulk Ga–As bond length of 2.45 Å [cf. Fig. 6.12(a)]. In the unoccupied DB state, this average bond length reduces to 2.37 Å upon structural relaxation.

The defect energies vs. Fermi energy are given in Fig. 6.12(b). For the supercell in the charge state $Q = +1$, we find the finite-size correction to be negligible (0.01 eV). The calculated defect level $\varepsilon_{0.75/-0.25}$ lies at 1.09 eV above the bulk GaAs VBM. The present result is close to previous calculations performed for a DB in bulk GaAs [109] [cf. Fig. 6.12(b)] or in an As-terminated GaAs/oxide interface model [115]. All these results agree in locating the defect level of the Ga DB defect in the upper part of the GaAs band gap. In this energy region, the experimental density of interface states only shows a small peak [76, 103]. Therefore, the Ga DB defect could be at the origin of this experimental feature.

As DB defect

An As dangling bond is modeled at the GaAs/Al₂O₃ interface through the creation of a cavity in model I of the GaAs/Al₂O₃ interface, as shown in Fig. 6.13(a). After removing one interfacial Ga atom and one interfacial O atom, one H atom is inserted to saturate the undesired As dangling bond. In this model, the compensating structural units consist of the saturated As–H bond and of the interfacial rearrangements upon which a fivefold coordinated Ga atom becomes fourfold coordinated supplying half an electron. In our model, the As DB state is doubly occupied ($q = -3/4$) in the neutral supercell ($Q = 0$) and is singly occupied ($q = +1/4$) when the supercell is charged with a total charge $Q = +1$.⁵ In the doubly occupied defect state shown in Fig. 6.13(a), the average bond length of the As–Ga bonds involving the As atom

⁵Upon structural relaxation of the singly occupied DB state, we constrain the H–As bond length to control the electron counting and to avoid more involved structural relaxations.

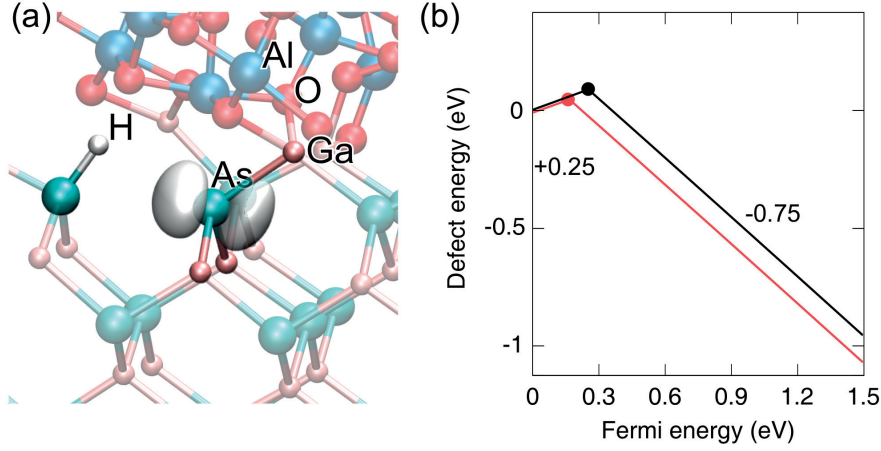


Figure 6.13 – (a) Relaxed structure of the As DB defect at the GaAs/Al₂O₃ interface. The charge density of the doubly occupied defect state is shown in transparency. (b) Defect energy of the As DB defect as obtained through the use of model I of the GaAs/Al₂O₃ interface (black lines) and of a bulk model (from Ref. [109], red lines).

carrying the DB is 2.40 Å and undergoes minimal variation upon removal of one electron.

The defect energies vs. Fermi energy are given in Fig. 6.13(b). A finite-size correction of 0.16 eV is applied to the defect energy of the singly occupied DB state obtained with a total charge $Q = +1$ in the supercell. The calculated charge transition level $\epsilon_{0.25/-0.75}$ is found at 0.25 eV above the GaAs VBM, in good agreement with a previous result obtained for an As DB in bulk GaAs [109] [cf. Fig. 6.13(b)]. This defect thus offers an interpretation for the origin of the small peak in the D_{it} close to the VBM [76, 103].

As–As dimer/DB defect

An isolated As–As dimer/DB defect is modeled at the GaAs/Al₂O₃ interface as described in Sec. 6.2. The application of the electron counting rule shows that each As–O–As or As–As interfacial unit releases half an electron while each Ga–O–Ga interfacial unit captures half an electron. In the neutral supercell, our interface model contains an As–As dimer defect carrying a local charge $q = 0.5$ and compensating structural units with a charge $q' = -0.5$ corresponding to the interfacial Ga–O–Ga and As–O–As units [113]. The As–As dimer undergoes bond breaking upon the capture of two electrons leading to the formation of two doubly occupied As dangling bonds ($2 \text{ DB}_{\text{As}}^{\bullet}$). The electron counting rule assigns a charge state of $q = -1.5$ to the $2 \text{ DB}_{\text{As}}^{\bullet}$ configuration. When the two extra electrons are removed, the reaction spontaneously reverts upon structural relaxation. The As–As dimer and the $2 \text{ DB}_{\text{As}}^{\bullet}$ configurations have opposite charge states and the associated defect is thus amphoteric.

In the As–As dimer defect state, the As–As bond length is 2.57 Å. The dimer can accommodate one extra electron in its antibonding state leading to a state that we denote $(\text{As–As})^{\star}$. In this state, the As–As bond length has increased to 2.89 Å. Upon the capture of a second extra

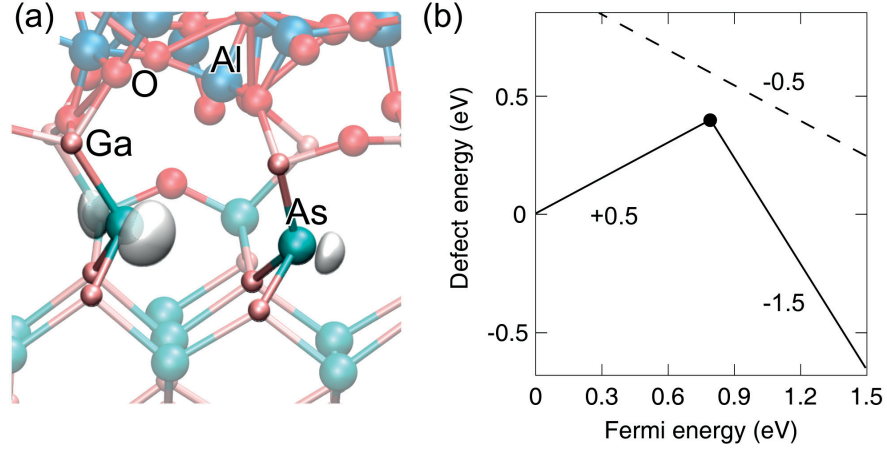


Figure 6.14 – (a) Relaxed structure of the 2 DB*_{As} defect state of the As–As dimer/DB defect. (b) Defect energy of As–As dimer/DB defect and of the metastable (As–As)* defect state as obtained through the use of model I' of the GaAs/Al₂O₃ interface.

electron, the homopolar bond breaks giving rise to the 2 DB*_{As} configuration, in which the two As atoms are separated by 4.21 Å. This charge state is illustrated in Fig. 6.14(a).

Figure 6.14(b) gives the relative defect energies of the various charge states as a function of Fermi energy. Finite-size corrections applied to the (As–As)* and the 2 DB*_{As} states amount to 0.07 and 0.20 eV, respectively. The stable defect states are the As–As dimer state and the 2 DB*_{As} state, showing a negative-*U* behavior. The calculated charge transition level $\epsilon_{0.5/-1.5}$ between these defect states falls at 0.79 eV above the GaAs VBM. We note that this level agrees very well with the charge transition level calculated for the same defect occurring in two amorphous suboxide models when aligned to the GaAs band gap (cf. Section 5.2). The (As–As)* state is found to be unstable for all Fermi energies in the GaAs band gap. The metastability of this defect state suggests that it does not play any role in the Fermi-level pinning, unlike previously assumed [111, 113]. In the present calculation, the defect level $\epsilon_{0.5/+0.5}$ lies at 0.99 eV above the VBM, lower by ~0.3 eV compared to the defect level found in Ref. [113] for an interface model with an As-terminated GaAs substrate.

To examine possible consequences of the neglected $q-q'$ interaction on the energetics of the present defect, we consider a second model interface. A Mg atom is added in the middle of the oxide layer, leading to a drastic modification of the electrostatic conditions. In the globally neutral simulation cell ($Q = 0$), the two valence electrons provided by the Mg atom drive the transformation of the As–As dimer to 2 DB*_{As}. Through the electron counting rule, we infer that the simulation cell now contains structural units accounting for a global charge of $q' = +1.5$, in addition to the defect charge. The charge q' arises in part from the interfacial bonding pattern [113] and in part from the presence of the Mg ion. Following the removal of two electrons from the simulation cell ($Q = +2$), the dimer is recovered upon structural relaxation. The relevant $+2/0$ charge transition level occurs at 0.61 eV above the valence band maximum [cf. Fig. 6.15(b)], shifted by 0.19 eV to lower energy compared to the corresponding level achieved for the model interface without the Mg atom shown in Fig. 6.15(a). Since the

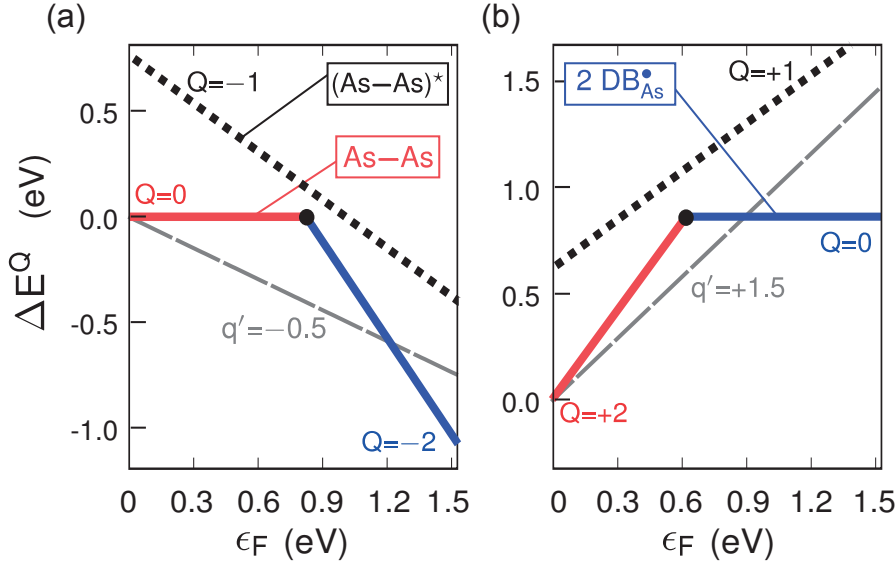


Figure 6.15 – Relative energies ΔE^Q of our two GaAs/oxide model interfaces vs. Fermi energy ϵ_F for various charge states Q of the simulation cell. The model interfaces both show an interfacial dimer/DB defect (a) without or (b) with an additional Mg atom in the oxide. The gray dashed lines indicate the energy of the structural units of charge q' , which are unrelated to the defect.

charge q' in the two considered model interfaces significantly differs in sign, amount, and distribution, this discrepancy can be considered as an estimate of the effect of the interaction between the defect charge q and the charge q' . The resulting indetermination in the position of the defect level in Fig. 6.14(b) is thus of the same size as typical theoretical errors (~ 0.2 eV) [160].

The $\epsilon_{0.5/-1.5}$ defect level calculated at 0.79 eV is consistent with the mid-gap peak at ~ 0.7 eV in the experimental defect density of states [76, 103, 104]. Furthermore, the amphoteric nature of the As-As dimer/DB defect naturally explains the occurrence of Fermi-level pinning through a feedback mechanism [127]. The description of this defect also agrees with the experimental observation that the defect states change from donor-like to acceptor-like upon the crossing of the mid-gap peak [76]. The dependence of the As enrichment of the surface prior to the oxide deposition [104] is a natural consequence of the As-related nature of this defect. Finally, the absence of Fermi-level pinning in MBE-grown samples could be related to the difficulty of forming an interfacial defect such as the As-As dimer/DB during these specific growth conditions which favor bulk-like reconstructions.

Our model also explains the connection between Fermi-level pinning and As antisites as invoked in the oxygen deposition experiments by Spicer and collaborators [51]. Upon exposure to a low dose of oxygen, the Fermi level is found to be pinned at either the higher or lower defect level of the As antisite defect, depending on the type of doping in GaAs. We note that, when calculated at the same level of theory, the defect levels of the As antisite lie at 0.67 and 1.04 eV above the valence band maximum [123], and thus *straddle* the charge transition level

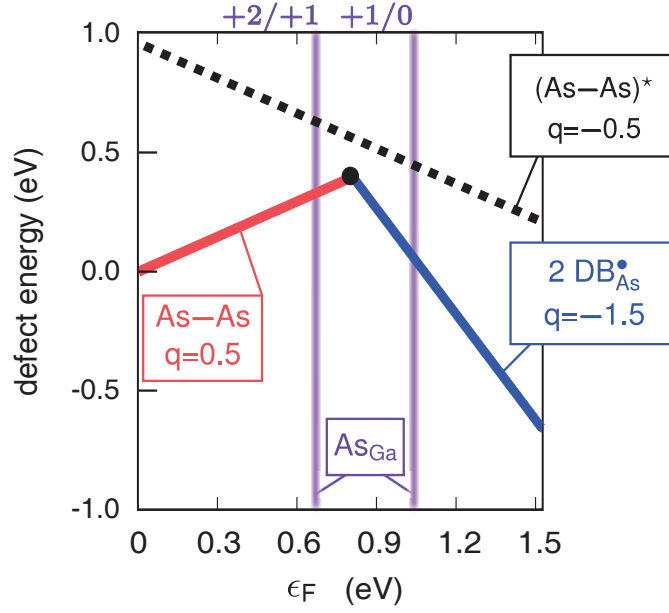


Figure 6.16 – Energy of the dimer/DB defect vs. Fermi energy for its various charge states q . The defect energies are referred to the As–As dimer in p -type GaAs. The vertical lines correspond to the charge transition levels of the As antisite defect [123].

of the dimer/DB defect (Fig. 6.16). Furthermore, it is well known that the As antisite defect occurs in high concentrations in bulk GaAs [31, 189]. The observed pinning behavior can then be explained as follows. A minority concentration of the dimer/DB defect is generated upon the exposure to a low dose of oxygen [51] through the mechanism described in Fig. 5.1. These defects give rise to charge compensation driving the Fermi level from the band edge to the charge transition level of the dimer/DB defect. However, the Fermi level remains pinned when it hits the first-encountered level of the majority antisite defects.

As 2*p* core-level shift

XPS experiments performed on n -type GaAs/oxide interfaces identify the presence of As–As linkages in the vicinity of the interface which are not responsive to passivation techniques [96]. Moreover, recent ESR experiments have detected the presence of As_{Ga} defects at the interface [106], which could be at the origin of the XPS signal. This assignment has been confirmed through the calculation of core-level shifts of the neutral As_{Ga} defect and of the As–As dimer, which clearly show that the calculated shift relative to the former defect agrees with the experimental line [118]. However, our study of the As–As dimer/DB metastability implies that in n -type condition the As–As defect occurs in the form of 2 DB_{As}[•]. As the XPS experiment is performed on a n -type GaAs/oxide interface we study the 2*p* core-level shift of the As_{Ga} defect and 2 DB_{As}[•] defect at the interface with Al₂O₃.

We compute the As 2*p* core-level shift through total energy differences of the system with an excited As atom. The unperturbed system is used as reference. The excited As atom

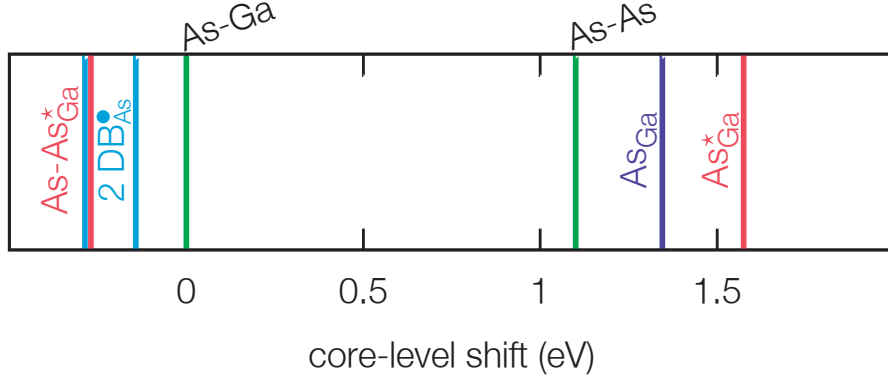


Figure 6.17 – Calculated As $2p$ core-level shifts for the stable and metastable neutral As antisite defect (As_{Ga} and As_{Ga}^*), the threefold As atom in the As_{Ga}^* configuration ($\text{As-As}_{\text{Ga}}^*$), and the two As atoms carrying a doubly occupied DB in the 2DB_{As}^* defect configuration. Experimental signals (green lines) of the As $2p$ core-level shift for bulk As atoms (As–Ga) and for the As–As structure (As–As). Theoretical values are referred to the As–Ga line.

is described through an appropriate pseudopotential carrying a core hole in the $2p$ level [212]. We consider vertical transitions in which the atomic structure is kept fixed. Within the pseudopotential approach, absolute binding energies are not accessible, but core-level shifts can be accurately given with respect to a reference. As a reference we use the XPS line of the As–Ga bond, corresponding to the average value obtained for four As atoms in the bulk region (far from the interfaces) of our interface models. Due to the use of different pseudopotentials for the As atoms with respect to our other calculations, we adopt a kinetic-energy cutoff of 100 Ry and a \mathbf{k} -points mesh $2 \times 2 \times 2$.

The calculated line for the stable neutral As_{Ga} falls at 1.34 eV from the As–Ga line. For the As antisite atom in the As_{Ga}^* configuration the calculated core-level falls at 1.57 eV, while the As atom carrying a DB and facing the Ga vacancy gives a line at -0.27 eV. For the 2DB_{As}^* defect structure, we calculate core level shifts of -0.29 and -0.14 eV with respect to the As–Ga line. In comparison with previous calculations, we note that the present shift for the stable neutral As_{Ga} defect increases by 0.24 eV. This difference can be ascribed to the presence of the interface in the present calculation (values obtained in Ref. [118] refer to bulk calculations). The comparison with the experimental lines assigns the measured As–As line to the As antisite atom. However, we note that the lines calculated for the 2DB_{As}^* defect fall very close to the experimental As–Ga line. In particular, considering that the half width at half maximum of the experimental peak amounts to ~ 0.7 eV, the presence of the 2DB_{As}^* defect can not be excluded since the corresponding signal fall within the width of the As–Ga line.

Discussion and Conclusions

In this Section, we studied a set of defects susceptible to play a role in Fermi-level pinning at GaAs/oxide interfaces. All considered defects were generated within atomistic models representing the GaAs/ Al_2O_3 interface and properly accounting for the local screening properties.

In particular, we focused on the As antisite, the $V_{\text{Ga}}\text{-As}_{\text{Ga}}/V_{\text{As}}\text{-}2\text{As}_{\text{Ga}}$ complex, the $(\text{As}_{\text{Ga}})_2\text{-O}_{\text{As}}$ defect, the As dangling bond, the Ga dangling bond, and the As–As dimer/DB defect. These defects can be distinguished in two types. The first three defects are bulk-like defects which could either exist in the bulk or in the vicinity of the interface. For this type of defects, a pristine reference has been defined and formation energies have explicitly been evaluated. In particular, it has been possible to compare the formation energy of these defects with those of their bulk counterparts. The last three defects are interfacial defects occurring at the termination of crystalline GaAs and do not admit any bulk correspondent. For these defects, the absence of a pristine reference prevents the calculation of absolute formation energies. Nevertheless, relative defect energies associated to their various charge states and charge transition levels could still be determined.

Table 6.2 – Formation energies of the bulk-like defects considered in the present work in their charge state q , as calculated in bulk GaAs and at the GaAs/Al₂O₃ interface. The Fermi level is taken at the VBM (p -type condition). The formation energies are given in eV.

Defect	q	Bulk	Interface
As_{Ga}	+2	−0.34	−0.64
	+1	0.18	0.03
	0	1.14	1.08
As_{Ga}^*	0	1.38	1.10
$(\text{As}_{\text{Ga}})_2\text{-O}_{\text{As}}$	+1	1.49	−0.81
	0	2.75	0.46
	−1	2.31	1.57
$V_{\text{Ga}}\text{-As}_{\text{Ga}}/V_{\text{As}}\text{-}2\text{As}_{\text{Ga}}$	+1	1.51	−0.15
	0	-	0.38
	−1	2.65	1.15
	−2	3.94	-

Among the bulk-like defects considered, the $(\text{As}_{\text{Ga}})_2\text{-O}_{\text{As}}$ defect shows the lowest formation energy. The $V_{\text{Ga}}\text{-As}_{\text{Ga}}/V_{\text{As}}\text{-}2\text{As}_{\text{Ga}}$ defect complex shows low formation energies for all values of the Fermi energy, and is ~ 1.4 eV more stable than the As_{Ga} defect in n -type conditions. Since the As antisite has experimentally been observed at the interface [106], the present results suggest that the $(\text{As}_{\text{Ga}})_2\text{-O}_{\text{As}}$ and $V_{\text{Ga}}\text{-As}_{\text{Ga}}/V_{\text{As}}\text{-}2\text{As}_{\text{Ga}}$ defects should occur at similar if not higher concentrations. Table 6.2 summarizes the formation energies of the bulk-like defects considered in this work as calculated in bulk GaAs and at the GaAs/Al₂O₃ interface. The comparison shows that the interface systematically stabilizes the bulk-like defects. The stabilization energy can be sizeable involving several eV as for example in the case of the $(\text{As}_{\text{Ga}})_2\text{-O}_{\text{As}}$ defect, or limited to only a few tenths of eV as in the case of the As antisite.

In Table 6.3, we summarize the charge transition levels as obtained in bulk GaAs and at the GaAs/Al₂O₃ interface for all the defects considered in the present work. The comparison shows that charge transition levels of defects located in the bulk or in the vicinity of the interface are generally rather close differing by at most 0.14 eV. The larger differences seen in the charge transition levels of the $V_{\text{Ga}}\text{-As}_{\text{Ga}}/V_{\text{As}}\text{-}2\text{As}_{\text{Ga}}$ defect should be assigned to the

Table 6.3 – Charge transition levels $\epsilon_{q1/q2}$ between the charge states $q1$ and $q2$ of the defects considered in the present work as calculated in bulk GaAs and at the GaAs/Al₂O₃ interface. The charge transition levels of the Ga and As DB modeled in bulk GaAs are taken from Ref. [109]. The charge transition levels are given in eV and are referenced with respect to the VBM.

	$\epsilon_{q1/q2}$	Bulk	Interface
Bulk-like defects			
As _{Ga}	$\epsilon_{+2/+1}$	0.53	0.67
	$\epsilon_{+1/0}$	0.96	1.04
(As _{Ga}) ₂ -O _{As}	$\epsilon_{+1/-1}$	1.14	1.19
V _{Ga} -As _{Ga} /V _{As} -2 As _{Ga}	$\epsilon_{+1/0}$	-	0.53
	$\epsilon_{0/-1}$	-	0.76
	$\epsilon_{+1/-1}$	0.57	-
	$\epsilon_{-1/-2}$	1.29	-
Interfacial defects			
Ga DB	$\epsilon_{+0.75/-0.25}$	1.20	1.09
As DB	$\epsilon_{+0.25/-0.75}$	0.16	0.25
As-As dimer/DB	$\epsilon_{+0.5/-1.5}$	-	0.79

structural modifications undergone by this defect at the interface.

The charge transition levels of the defects are more informative as they can directly be compared with the experimental D_{it} . In Fig. 6.18, the charge transition levels of the defects studied in this work are compared with various experimental measurements. The small peaks in the vicinity of the valence and conduction band edges can be associated to As and Ga dangling bonds, respectively, in accord with previous findings [109, 115]. Our results reveal that the (As_{Ga})₂-O_{As} defect also gives a defect level in the proximity of the GaAs CBM. Regarding the mid-gap peak, the As_{Ga}, the V_{Ga}-As_{Ga}/V_{As}-2 As_{Ga} complex, and the As-As dimer/DB defect all show defect levels in the concerned energy region. Among these defects, the As_{Ga} defect being a double-donor is unable to account for the experimental characterization, which rather points to a defect with amphoteric character [76]. Both the V_{Ga}-As_{Ga}/V_{As}-2 As_{Ga} defect complex and the As-As dimer/DB defect present the observed amphoteric behavior in this region of the GaAs band gap. Interestingly, despite their very different atomic structures, both these defects exhibit the same atomistic mechanism at the origin of their amphoteric nature, namely the transformation of one As-As bond into 2 DB_{As}[•] and vice versa upon the capture and release of two electrons. Our results go beyond previous studies by Lin and Robertson [111] and by Miceli and Pasquarello [113] on interfacial As-As dimers in which only a metastable dimer state was addressed.

To conclude, we remark that the As-As dimer/DB bistability has been found to be operative in

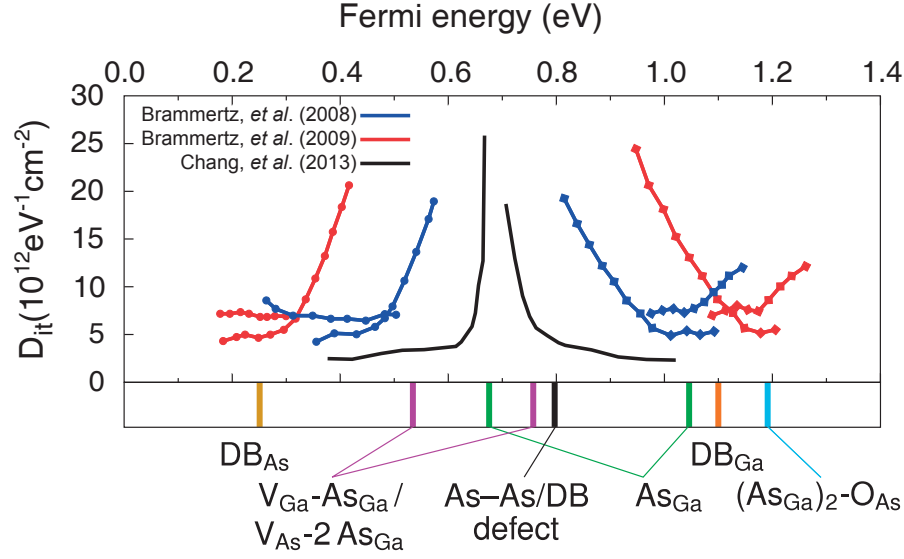


Figure 6.18 – Charge transition levels of the defects considered in this study positioned with respect to the experimental D_{it} at GaAs/oxide interfaces obtained by Brammertz *et al.* [76, 103] (red and blue lines) and by Chang *et al.* [104] (black lines). The lines with dots indicate donor-like defects while the lines with squares indicate acceptor-like defects.

a number of As-related defects leading to defect levels in the band gap of GaAs. The associated amphoteric behavior provides a feedback mechanism by which the Fermi-level can be pinned at the charge transition level where the positively and negatively charged defect state coexist. In particular, the $V_{Ga}-As_{Ga}/V_{As}-2 As_{Ga}$ complex and the As–As dimer/DB defects yield defect levels at mid gap and are valid candidate defects for the origin of the Fermi-level pinning at the GaAs/oxide interfaces. Moreover, we propose a rationale for the interpretation of the Fermi-level pinning observed in the early stages of the oxygen deposition on the GaAs surface. It is based on the formation of the As–As dimer/DB defect and clarifies the role of the As_{Ga} defect.

6.3 The role of In

The experimental density of interface states at the InGaAs/oxide interface shows a major peak in the vicinity of the valence band and a second smaller feature at mid-gap responsive to passivation treatments [76, 119, 120]. However, a significant contribution to the defect density appearing at ~ 0.3 eV above the conduction band edge [76, 119] represents a major obstacle for proper device operation leading to Fermi-level pinning in the proximity of the conduction band [121]. The measured D_{it} is independent from the nature of the deposited oxide, suggesting that the defects underlying the poor quality of the interfaces relate to the semiconductor substrate [119, 122].

Density functional calculations are instrumental for revealing the atomistic nature of these defects. Isolated As dangling bonds have been shown to give defect states close the valence band

edge [109], and thus provide an interpretation for the major peak in the density of interface states. Similarly the peak at mid-gap is consistent with the calculated defect level of the As antisite in InGaAs [123], in accord with observations at GaAs/oxide interfaces [106]. However, the trap states which are resonant with the conduction band have not yet conclusively been identified. Possible candidates are In or Ga dangling bonds [109] and the antibonding state of the As–As dimer [113, 124].

Computational details

We adopt the same scheme used for the study of defects at the GaAs/Al₂O₃ interface. In order to speed up the calculations, allowing the study of different cation environment of the defect, we sample the Brillouin zone at the sole Γ point. We verified that this \mathbf{k} -points sampling ensures converged results.

As–As dimer/DB defect

We address the As–As dimer/DB defect at the InGaAs/oxide interface by considering the model I' structure of the GaAs/Al₂O₃ interface. In this model, the As–As dimer shows six Ga first neighbors, four of which are located on the GaAs side of the interface and two on the Al₂O₃ side. Previous work showed that defect levels in InGaAs are fairly insensitive to the local environment extending beyond the first shell of neighbors [123]. Taking advantage of this property, we study the effect of In atoms on the As–As dimer/DB defect level by only considering substitutions within the first shell of Ga atoms. In view of the In concentration considered in this work, we limit our investigation to the most probable configurations involving three In atoms. We consider various configurations differing by the distribution of the In atoms among the six available sites, as illustrated in Fig. 6.19.

For each chemical environment, we consider the As–As dimer defect state and the corresponding charged configuration with $2\text{ DB}_{\text{As}}^{\bullet}$. For comparison with previous work [124], we also consider the (As–As)^{*} dimer state which corresponds to the trapping of one electron in its antibonding state. For all these configurations and charge states, the structure is fully relaxed and the total energy determined. The relaxed As–As dimer has an average inter-atomic distance of 2.53 Å (± 0.01 Å) in both the As–As and the (As–As)^{*} dimer states. This distance

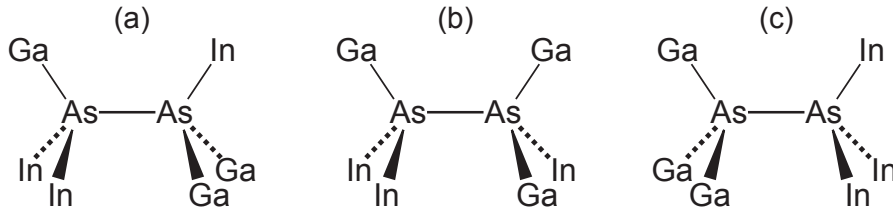


Figure 6.19 – Representation of the considered chemical environments around the As–As dimer/DB defect. The cations below the As–As dimer are located on the GaAs side of the interface while the cations above the As–As dimer are on the Al₂O₃ side of the interface.

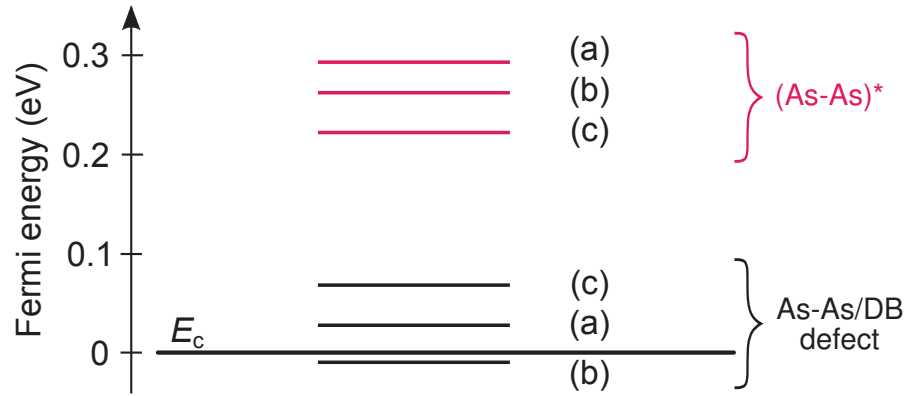


Figure 6.20 – Charge transition levels of the As–As dimer/DB defect (black lines) and of the (As–As)^{*} defect (red lines) at the InGaAs/Al₂O₃ interface as obtained for the chemical environments illustrated in Fig. 6.19. The energies are referenced with respect to the conduction edge (E_c) of InGaAs.

increases to 4.21 Å (± 0.15 Å) in the defect states with 2 DB_{As}^{*}. The average Ga–As and In–As bond lengths both undergo a small decrease upon the capture of two electrons, going from 2.52 to 2.44 Å and from 2.63 to 2.58 Å, respectively.

From the total energies of the defect states, we obtain their relative formation energies and the corresponding charge transition levels. The calculated defect levels are first aligned with respect to the GaAs band edges through the average electrostatic potential in the bulk GaAs component of the reference interface model [113]. We then align the band gap of InGaAs to that of GaAs using the experimental band offset [213]. The stable charge states of the As–As dimer/DB defect correspond to the As–As dimer and the 2 DB_{As}^{*} states. The (As–As)^{*} dimer state is found to be metastable, as found in the absence of In (cf. Section 6.2.2). At the InGaAs/Al₂O₃ interface, the calculated levels of the As–As dimer/DB defect are found to be resonant with the bottom of the InGaAs conduction band (Fig. 6.20). The defect levels which refer to the capture of one electron in the metastable (As–As)^{*} dimer state lie deeper in the conduction band, at 0.2–0.3 eV from the band edge (Fig. 6.20). In comparison to previous work [113], the energies calculated for the (As–As)^{*} dimer states are lower by ~ 0.3 eV due to the consideration of Ga terminated substrates in the present study.

The different arrangements of In atoms in the first neighbor shell of the defect only lead to minimal variations (± 0.05 eV) of the calculated defect levels. Comparison of the As–As dimer/DB and (As–As)^{*} defect levels with those obtained at the GaAs/Al₂O₃ interface, i.e. in the absence of any In atom in the first-neighbor shell of the As–As dimer/DB defect, shows differences smaller than 0.1 eV, indicating that the defect levels are only weakly affected by the presence of In atoms.

When the Fermi energy is progressively taken to higher values the As–As dimer/DB and (As–As)^{*} defects act as electron traps. This behavior is thus in accord with the experimental observation of acceptor states in the conduction band of InGaAs [76, 119]. In Fig. 6.21, we compare experimental defect densities at the In_{0.53}Ga_{0.47}As/Al₂O₃ interface [76, 119] with

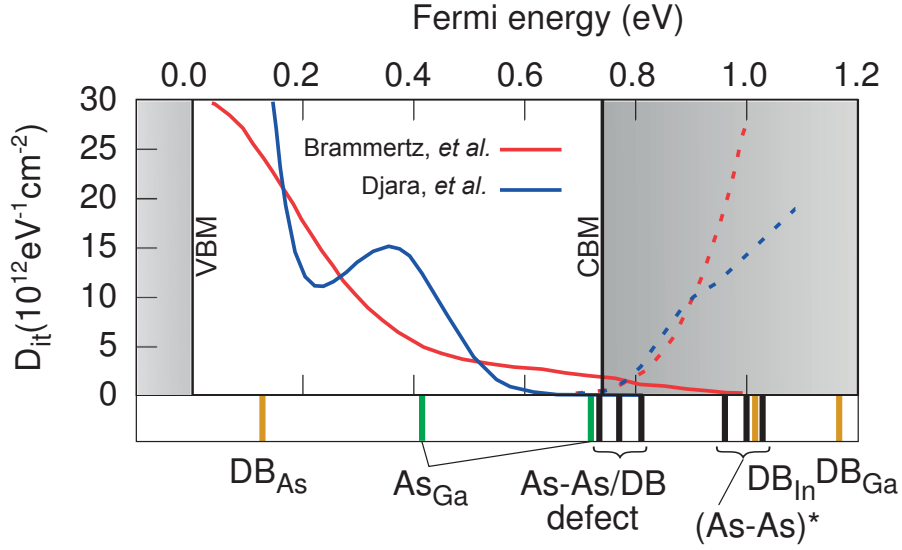


Figure 6.21 – Charge transition levels of the As–As dimer/DB and (As–As)^{*} defects positioned with respect to the experimental density of interface states at the InGaAs/oxide interface as measured by Brammertz *et al.* [122] (blue lines) and Djara *et al.* [119] (red lines). The continuous lines indicate donor-like defects, while the dotted lines indicate acceptor-like defects. For comparison, calculated charge transition levels from previous studies are also shown: DB_{As}, DB_{In} and DB_{Ga} levels from Ref. [109], As_{Ga} level from Ref. [123].

calculated energy levels of various candidate defects. In addition to the energy levels of the As–As dimer/DB and (As–As)^{*} defects calculated in this work, we also show the defect levels of the isolated As dangling bond [109], the As antisite [123], the In dangling bond and the Ga dangling bond [109] as reported in the literature. Experimental defect densities generally show low values at the conduction band minimum and increase as the Fermi-level moves deeper into the conduction band [76, 119]. In the concerned energy region, the defect levels of the As–As dimer/DB defect are found to lie in correspondence of the conduction band edge, while the In and Ga dangling bond states lie higher by 0.2–0.4 eV. In view of typical theoretical incertitudes of ~0.2 eV [160], either the As–As dimer/DB defect or the cationic dangling bonds (In and Ga) could account for the increase in the experimental density in the conduction band of InGaAs. Note that the (As–As)^{*} related states could act as trap states in dynamical measurements, but are thermodynamically metastable.

7 Conclusion

In the present thesis work, we address the origin of Fermi-level pinning at the GaAs/oxide interfaces due to defects through hybrid functionals. We perform preliminary studies on bulk GaAs considering a set of intrinsic and O defects. In particular, we investigate a set of intrinsic bulk defects including antisites, vacancies, and a bistable defect complex which involves a Ga vacancy and an As antisite (cf. Chapter 3). The properties of the latter complex agree with the experimental observation of Fermi-level pinning at 0.6 eV in radiation-damaged samples. Moreover, its formation energy is comparable with those of the most stable defects (As antisite and Ga vacancy). Interestingly, we note that its bistable and amphoteric behavior originates from the bistability of the As–As bond which transforms into two As dangling bonds (As–As dimer/DB bistability).

Considering O defects, we find that the oxidized form of this defect complex shows interesting structural and electrical properties (cf. Chapter 4). The capture of an O atom breaks the atomic transformation at the basis of the bistability observed in the un-oxidized defect. However, also this O defect complex shows a bistable nature which involves a different atomistic transformation but which can still be related to that of the As–As dimer/DB bistability. We show that this $(\text{As}_{\text{Ga}})_2\text{-O}_{\text{As}}$ defect complex is stable against dissociation of O and As antisite atoms, and that it has the lowest formation energy among the considered defects. Thus, it is the dominant O defect in GaAs and it competes with the O_{b} defect only in a small range of Fermi energies. The characterization of the $(\text{As}_{\text{Ga}})_2\text{-O}_{\text{As}}$ defect agrees with the large body of experimental data available in the literature. It accurately accounts for the experimental Fermi-level pinning position, the Ga–O–Ga core structure, the metastable and paramagnetic properties of the neutral charge state, the stability of the +1 and –1 charge states, and the optical transition energies between its charge states. These results strongly support this defect as origin of the Fermi-level pinning in oxygen-doped GaAs. As a first general result, these preliminary studies on bulk GaAs reveal the importance of the amphoteric behavior in defect-induced Fermi-level pinning. Moreover, they show the important role of the As–As/DB bistability observed in bulk defect complexes in GaAs.

Due to the importance of the GaAs oxidation process during the deposition of an oxide we consider intermediately oxidized GaAs systems (cf. Chapter 5). In particular, we focus on the sub-monolayer deposition of O atoms on the GaAs(110) surface. Through molecular dynamics and nudged-elastic-band simulations, we observe and study the mechanism which leads to

the formation of superficial As–As dimer/DB defect upon O absorption. Then, we generate amorphous suboxide models representative of the interface transition layer by a molecular dynamics quench from the melt. We generate two models with different stoichiometries in order to simulate the composition proposed through ion scattering experiments and its As-rich variation. Our structural analysis reveals the absence of As–O bonds indicating that the composition of the suboxides is a mixture of GaAs and Ga oxide. The band gaps of these suboxides compare well with that of GaAs. Upon a three step alignment procedure, the calculated band offsets with respect to GaAs band edges are found to be within 0.2 eV. Finally, we observe the occurrence of the As–As dimer/DB defect in both our suboxide models, leading to charge transition levels at ~ 0.7 eV above the VBM of GaAs, in accord with the experimental defect density of states. These results qualitatively correlate the GaAs oxidation process with the formation of the As–As dimer/DB defect and quantitatively locate its charge transition level in the midgap region of the GaAs band gap. The agreement with the measured density of interfacial states reveals the important role that this defect can play at GaAs/oxide interfaces.

Finally, we address the GaAs/Al₂O₃ interface. We calculate the band offsets between GaAs and an amorphous model of Al₂O₃ generated by molecular dynamics quench of the melt. The structural properties of our model are validated through comparison with the experimental radial distribution function. The electronic band gap is calculated with hybrid functionals after obtaining the proper fraction of Fock exchange from crystalline alumina. Calculated band offsets favor the occurrence of Ga–O bonds at the interface and show excellent agreement with experimental results achieved through X-ray photoemission experiments. Then, we study structural and electrical properties of defects occurring on the GaAs side of this interface, which shows Al₂O₃ as the representative oxide material. The As–As dimer/DB defect and the $V_{\text{Ga}}\text{-As}_{\text{Ga}}/V_{\text{As}}\text{-2As}_{\text{Ga}}$ defect complex show a bistable nature which can be attributed to the reversible transformation between an As–As dimer and two As dangling bonds. These defects show charge transition levels at ~ 0.7 eV above the VBM, thereby separating the regimes in which donor-like and acceptor-like defects are stable, in agreement with the midgap density of defect states measured experimentally. These results corroborate the primary role of the As–As dimer/DB defect in the Fermi-level pinning observed at GaAs/oxide interfaces. Also, the dependence of the mid-gap peak intensity on the level of As enrichment at the GaAs surface prior to oxidation is a natural consequence of the As-related origin of the proposed defects. The achievement of unpinned GaAs/oxide interfaces through MBE growth can be rationalized as this growth technique prevents the rearrangement of As atoms in the form of dimer/DB defects. In retrospect, by comparing the calculated electrical properties of the As–As dimer/DB defect with those of the As antisite defect, we suggest a rationale for the observed Fermi-level pinning at the surface, in which the role of As antisites is clarified. Finally, we study the effect of the incorporation of In atoms in the first neighboring shell of the As–As dimer/DB defect at the interface. We observe minimal variations of the defect charge transition level upon the inclusion of In atoms, leading to defect levels resonant with the bottom of the InGaAs conduction band. Comparison with the experimental density of defect states suggests that the As–As dimer/DB defect is a valid candidate defect for the defect density in the conduction band of InGaAs.

In conclusion, this thesis addresses Fermi-level pinning phenomena covering different GaAs systems (including bulk, surface, and interfaces with oxides) and occurring at different positions in the band gap. Despite these differences in the resulting macroscopic electrical

behaviors we propose a common atomistic mechanism underling these physical processes. Indeed, we find that the As–As dimer/DB transformation can be found as isolated defect or within defect complexes preserving its bistable and amphoteric nature. These properties are ultimately responsible for the electrical feedback mechanism which causes Fermi-level pinning in radiation-damaged GaAs, at GaAs surfaces, and at GaAs/oxide interfaces.

Bibliography

- [1] D. Colleoni, G. Miceli, and A. Pasquarello, "Fermi-level pinning through defects at GaAs/oxide interfaces: A density functional study," *Phys. Rev. B*, vol. 92, p. 125304, Sept. 2015.
- [2] D. Colleoni, G. Miceli, and A. Pasquarello, "Arsenic related defect states resonant with the semiconductor conduction band at the $\text{In}_{0.53}\text{Ga}_{0.47}\text{As}$ /oxide interface: A density functional study," *Microelectron. Eng.*, vol. 147, p. 260, Nov. 2015.
- [3] D. Colleoni and A. Pasquarello, "Interfacial Ga-As suboxide: Structural and electronic properties," *Appl. Phys. Lett.*, vol. 107, p. 031605, July 2015.
- [4] Statista, "<http://www.statista.com/statistics/266973/global-semiconductor-sales-since-1988/>," 2015.
- [5] Statista, "<http://www.statista.com/statistics/271608/global-vehicle-sales-of-automobile-manufacturers/>," 2015.
- [6] S. D. Offsey, J. M. Woodall, A. C. Warren, P. D. Kirchner, T. I. Chappell, and G. D. Pettit, "Unpinned (100) GaAs surfaces in air using photochemistry," *Appl. Phys. Lett.*, vol. 48, p. 475, Feb. 1986.
- [7] S. Datta, T. Ashley, J. Brask, L. Buckle, M. Doczy, M. Emeny, D. Hayes, K. Hilton, R. Jeffries, T. Martin, T. Phillips, D. Wallis, P. Wilding, and R. Chau, "85nm gate length enhancement and depletion mode insb quantum well transistors for ultra high speed and very low power digital logic applications," *Electron Devices Meeting, 2005. IEDM Technical Digest. IEEE International*, p. 763, Dec. 2005.
- [8] R. Chau, S. Datta, M. Doczy, B. Doyle, B. Jin, J. Kavalieros, A. Majumdar, M. Metz, and M. Radosavljevic, "Benchmarking nanotechnology for high-performance and low-power logic transistor applications," *IEEE T. Nanotechnol.*, vol. 4, p. 153, Mar. 2005.
- [9] D.-H. Kim, J. del Alamo, J.-H. Lee, and K.-S. Seo, "Logic Suitability of 50-nm $\text{In}_{0.7}\text{Ga}_{0.3}\text{As}$ HEMTs for Beyond-CMOS Applications," *IEEE Electron Dev.*, vol. 54, p. 2606, Oct. 2007.
- [10] A. Pethe, T. Krishnamohan, D. Kim, S. Oh, H.-S. Wong, Y. Nishi, and K. Saraswat, "Investigation of the performance limits of III-V double-gate n-MOSFETs," in *Electron Devices Meeting, 2005. IEDM Technical Digest. IEEE International*, p. 605, Dec. 2005.
- [11] D. Kim, T. Krishnamohan, and K. Saraswat, "Performance Evaluation of III-V Double-Gate n-MOSFETs," in *Device Research Conference*, p. 67, June 2008.

Bibliography

- [12] D. Kim, T. Krishnamohan, and K. Saraswat, "Performance Evaluation of 15nm Gate Length Double-Gate n-MOSFETs with High Mobility Channels: III-V, Ge and Si," *ECS Trans.*, vol. 16, p. 47, Oct. 2008.
- [13] *Fundamentals of III-V Semiconductor MOSFETs*. Springer, 2009.
- [14] I. Vurgaftman, J. R. Meyer, and L. R. Ram-Mohan, "Band parameters for III–V compound semiconductors and their alloys," *J. Appl. Phys.*, vol. 89, p. 5815, June 2001.
- [15] J. S. Blakemore, "Semiconducting and other major properties of gallium arsenide," *J. Appl. Phys.*, vol. 53, p. R123, Oct. 1982.
- [16] L. Hrivnák, "Semi-insulating GaAs," *Czech. J. Phys. B*, vol. 34, p. 436, May 1984.
- [17] G. R. Cronin and R. W. Haisty, "The preparation of semi-insulating gallium arsenide by chromium doping," *J. Electrochem. Soc.*, vol. 111, p. 874, July 1964.
- [18] J. F. Woods and N. G. Ainslie, "Role of Oxygen in Reducing Silicon Contamination of GaAs during Crystal Growth," *J. Appl. Phys.*, vol. 34, p. 1469, May 1963.
- [19] G. Martin, A. Mitonneau, and A. Mircea, "Electron traps in bulk and epitaxial GaAs crystals," *Electron. Lett.*, vol. 13, p. 191, Mar. 1977.
- [20] G. J. Rees, *Semi-Insulating III-V Materials: Nottingham 1980*. Shiva Publishing Limited, 1980.
- [21] K. Elliott, R. T. Chen, S. G. Greenbaum, and R. J. Wagner, "Identification of As_{Ga} antisite defects in liquid encapsulated Czochralski GaAs," *Appl. Phys. Lett.*, vol. 44, p. 907, May 1984.
- [22] M. Kaminska, "EL2 defect in GaAs," *Phys. Scr.*, vol. 1987, p. 551, Jan. 1987.
- [23] G. Vincent, D. Bois, and A. Chantre, "Photoelectric memory effect in GaAs," *J. Appl. Phys.*, vol. 53, p. 3643, May 1982.
- [24] H. J. v. Bardeleben, N. T. Bagraev, and J. C. Bourgoin, "Optically induced regeneration of the stable configuration of the EL2 defect in GaAs," *Appl. Phys. Lett.*, vol. 51, p. 1451, Nov. 1987.
- [25] F. Koschnick and J.-M. Spaeth, "Structural Analysis of Intrinsic Defects in GaAs and Al_xGa_{1-x}As by Magnetooptically Detected Magnetic Resonance Spectroscopy," *Phys. Stat. Sol. B*, vol. 216, p. 817, Dec. 1999.
- [26] R. J. Wagner, J. J. Krebs, G. H. Stauss, and A. M. White, "Submillimeter EPR evidence for the As antisite defect in GaAs," *Solid State Commun.*, vol. 36, p. 15, Oct. 1980.
- [27] M. Baeumler, U. Kaufmann, and J. Windscheif, "Photoresponse of the As_{Ga} antisite defect in as-grown GaAs," *Appl. Phys. Lett.*, vol. 46, p. 781, Apr. 1985.
- [28] G. Baraff, "Recent changes in our understanding of EL2 in GaAs," in *1992 Proceedings of the 7th Conference on Semi-Insulating III-V Materials*, p. 11, 1992.

-
- [29] J. Dabrowski and M. Scheffler, "Theoretical evidence for an optically inducible structural transition of the isolated antisite in GaAs: identification and explanation of EL2?," *Phys. Rev. Lett.*, vol. 60, p. 2183, May 1988.
- [30] B. K. Meyer, D. M. Hofmann, J. R. Niklas, and J.-M. Spaeth, "Arsenic antisite defect As_{Ga} and EL2 in GaAs," *Phys. Rev. B*, vol. 36, p. 1332, Jul 1987.
- [31] M. Jordan, M. Linde, T. Hangleiter, and J. Spaeth, "Deep-level defects in high-resistivity GaAs grown by the horizontal bridgman technique," *Semicond. Sci. Technol.*, vol. 7, no. 6, p. 731, 1992.
- [32] M. Luysberg, H. Sohn, A. Prasad, P. Specht, Z. Liliental-Weber, E. R. Weber, J. Gebauer, and R. Krause-Rehberg, "Effects of the growth temperature and As/Ga flux ratio on the incorporation of excess as into low temperature grown GaAs," *J. Appl. Phys.*, vol. 83, no. 1, p. 561, 1998.
- [33] H. C. Alt, "Experimental evidence for a negative-U center in gallium arsenide related to oxygen," *Phys. Rev. Lett.*, vol. 65, no. 27, p. 3421, 1990.
- [34] H. C. Alt, Y. V. Gomeniuk, and U. Kretzer, "Charge states and quantitative infrared spectroscopy of electrically active oxygen centers in gallium arsenide," *J. Appl. Phys.*, vol. 101, p. 073516, Apr. 2007.
- [35] J. Schneider, B. Dischler, H. Seelewind, P. M. Mooney, J. Lagowski, M. Matsui, D. R. Beard, and R. C. Newman, "Assessment of oxygen in gallium arsenide by infrared local vibrational mode spectroscopy," *Appl. Phys. Lett.*, vol. 54, no. 15, p. 1442, 1989.
- [36] M. Skowronski, S. T. Neild, and R. E. Kremer, "Location of energy levels of oxygen-vacancy complex in GaAs," *Appl. Phys. Lett.*, vol. 57, no. 9, p. 902, 1990.
- [37] H. C. Alt, "Fine structure of the oxygen-related local mode at 714 cm^{-1} in GaAs," *Appl. Phys. Lett.*, vol. 55, no. 26, p. 2736, 1989.
- [38] H. C. Alt, "Photosensitivity of the 714 and 730 cm^{-1} absorption bands in semi-insulating GaAs: Evidence for a deep donor involving oxygen," *Appl. Phys. Lett.*, vol. 54, p. 1445, Apr. 1989.
- [39] F. K. Koschnick, M. Linde, M. V. B. Pinheiro, and J.-M. Spaeth, "Optically detected electron-paramagnetic-resonance investigations of the substitutional oxygen defect in gallium arsenide," *Phys. Rev. B*, vol. 56, p. 10221, Oct. 1997.
- [40] M. Linde, J.-M. Spaeth, and H. C. Alt, "The paramagnetic charge state of substitutional oxygen in GaAs," *Appl. Phys. Lett.*, vol. 67, p. 662, July 1995.
- [41] R. Jones and S. Öberg, "Multiple charge states of substitutional oxygen in gallium arsenide," *Phys. Rev. Lett.*, vol. 69, p. 136, July 1992.
- [42] T. Mattila and R. M. Nieminen, "Ab initio study of oxygen point defects in GaAs, GaN, and AlN," *Phys. Rev. B*, vol. 54, no. 23, p. 16676, 1996.
- [43] W. Orellana and A. C. Ferraz, "Structural properties and energetics of oxygen impurities in GaAs," *Phys. Rev. B*, vol. 61, p. 5326, Feb. 2000.

Bibliography

- [44] A. Taguchi and H. Kageshima, "First-principles investigation of the oxygen negative- U center in GaAs," *Phys. Rev. B*, vol. 57, no. 12, p. 6779, 1998.
- [45] M. Pesola, J. Boehm, V. Sammalkorpi, T. Mattila, and R. M. Nieminen, "Microscopic structure of oxygen defects in gallium arsenide," *Phys. Rev. B*, vol. 60, no. 24, p. 16267, 1999.
- [46] P. K. Larsen, J. F. van der Veen, A. Mazur, J. Pollmann, J. H. Neave, and B. A. Joyce, "Surface electronic structure of GaAs(001)-(2 \times 4): Angle-resolved photoemission and tight-binding calculations," *Phys. Rev. B*, vol. 26, p. 3222, Sep 1982.
- [47] H. Tsuda and T. Mizutani, "Photoionization energy variation among three types of As-stabilized GaAs (001) 2 \times 4 surfaces," *Appl. Phys. Lett.*, vol. 60, p. 1570, Mar. 1992.
- [48] M. D. Pashley, K. W. Haberern, R. M. Feenstra, and P. D. Kirchner, "Different Fermi-level pinning behavior on n - and p -type GaAs(001)," *Phys. Rev. B*, vol. 48, p. 4612, Aug 1993.
- [49] M. D. Pashley, K. W. Haberern, W. Friday, J. M. Woodall, and P. D. Kirchner, "Structure of GaAs(001) (2 \times 4) – c (2 \times 8) determined by scanning tunneling microscopy," *Phys. Rev. Lett.*, vol. 60, p. 2176, May 1988.
- [50] B. A. Banse and J. R. Creighton, "Formation of "super" As-rich GaAs(100) surfaces by high temperature exposure to arsine," *Appl. Phys. Lett.*, vol. 60, p. 856, Feb. 1992.
- [51] W. Spicer, P. Chye, C. Garner, I. Lindau, and P. Pianetta, "The surface electronic structure of 3-5 compounds and the mechanism of Fermi level pinning by oxygen (passivation) and metals (Schottky barriers)," *Surf. Sci.*, vol. 86, p. 763, July 1979.
- [52] W. E. Spicer, "New and unified model for schottky barrier and III–V insulator interface states formation," *J. Vac. Sci. Technol.*, vol. 16, p. 1422, Sept. 1979.
- [53] P. Skeath, I. Lindau, P. W. Chye, C. Y. Su, and W. E. Spicer, "Investigation of the mechanism for Schottky barrier formation by group III metals on GaAs(110)," *J. Vac. Sci. Technol.*, vol. 16, p. 1143, Sept. 1979.
- [54] W. E. Spicer, I. Lindau, P. Skeath, C. Y. Su, and P. Chye, "Unified mechanism for Schottky-barrier formation and III-V oxide interface states," *Phys. Rev. Lett.*, vol. 44, no. 6, p. 420, 1980.
- [55] W. E. Spicer, I. Lindau, P. Skeath, and C. Y. Su, "Unified defect model and beyond," *J. Vac. Sci. Technol.*, vol. 17, p. 1019, Sept. 1980.
- [56] W. E. Spicer, Z. Liliental-Weber, E. Weber, N. Newman, T. Kendelewicz, R. Cao, C. McCants, P. Mahowald, K. Miyano, and I. Lindau, "The advanced unified defect model for Schottky barrier formation," *J. Vac. Sci. Technol. B*, vol. 6, p. 1245, July 1988.
- [57] W. E. Spicer, "“Pinning” and Fermi level movement at GaAs surfaces and interfaces," *J. Vac. Sci. Technol. A*, vol. 8, p. 2084, May 1990.
- [58] A. Kahn, E. So, P. Mark, C. B. Duke, and R. J. Meyer, "Surface and near-surface atomic structure of GaAs (110)," *J. Vac. Sci. Technol.*, vol. 15, p. 1223, July 1978.

- [59] J. Van Laar and J. J. Scheer, "Influence of volume dope on Fermi level position at gallium arsenide surfaces," *Surf. Sci.*, vol. 8, p. 342, Sept. 1967.
- [60] J. R. Chelikowsky and M. L. Cohen, "Self-consistent pseudopotential calculation for the relaxed (110) surface of GaAs," *Phys. Rev. B*, vol. 20, p. 4150, Nov. 1979.
- [61] W. Mönch and H. Gant, "Chemisorption-Induced Defects on GaAs(110) Surfaces," *Phys. Rev. Lett.*, vol. 48, p. 512, Feb. 1982.
- [62] B. A. Joyce, "Molecular beam epitaxy," *Rep. Prog. Phys.*, vol. 48, p. 1637, Dec. 1985.
- [63] M. Passlack, M. Hong, and J. P. Mannaerts, "Quasistatic and high frequency capacitance-voltage characterization of Ga₂O₃-GaAs structures fabricated by in situ molecular beam epitaxy," *Appl. Phys. Lett.*, vol. 68, no. 8, p. 1099, 1996.
- [64] M. Hong, M. Passlack, J. P. Mannaerts, J. Kwo, S. N. G. Chu, N. Moriya, S. Y. Hou, and V. J. Fratello, "Low interface state density oxide-GaAs structures fabricated by insitu molecular beam epitaxy," *J. Vac. Sci. Technol. B*, vol. 14, p. 2297, May 1996.
- [65] M. Passlack, M. Hong, J. Mannaerts, R. Opila, S. Chu, N. Moriya, F. Ren, and J. Kwo, "Low D_{it}, thermodynamically stable Ga₂O₃-GaAs interfaces: fabrication, characterization, and modeling," *IEEE Electron Dev.*, vol. 44, p. 214, Feb. 1997.
- [66] M. Hong, J. Kwo, A. R. Kortan, J. P. Mannaerts, and A. M. Sergent, "Epitaxial cubic gadolinium oxide as a dielectric for gallium arsenide passivation," *Science*, vol. 283, p. 1897, Mar. 1999.
- [67] M. J. Hale, S. I. Yi, J. Z. Sexton, A. C. Kummel, and M. Passlack, "Scanning tunneling microscopy and spectroscopy of gallium oxide deposition and oxidation on GaAs(001)-c(2×8)/(2×4)," *J Chem. Phys.*, vol. 119, no. 13, p. 6719, 2003.
- [68] R. W. Johnson, A. Hultqvist, and S. F. Bent, "A brief review of atomic layer deposition: from fundamentals to applications," *Mater. Today*, vol. 17, p. 236, June 2014.
- [69] H. Hasegawa, K. E. Forward, and H. L. Hartnagel, "New anodic native oxide of GaAs with improved dielectric and interface properties," *Appl. Phys. Lett.*, vol. 26, p. 567, May 1975.
- [70] N. Yokoyama, T. Mimura, K. Odani, and M. Fukuta, "Low-temperature plasma oxidation of GaAs," *Appl. Phys. Lett.*, vol. 32, p. 58, Jan. 1978.
- [71] D. S. L. Mui, H. Liaw, A. L. Demirel, S. Strite, and H. Morkoç, "Electrical characteristics of Si₃N₄/Si/GaAs metal-insulator-semiconductor capacitor," *Appl. Phys. Lett.*, vol. 59, p. 2847, Nov. 1991.
- [72] M. Ameen, L. Nyns, S. Sioncke, D. Lin, T. Ivanov, T. Conard, J. Meersschaut, M. Y. Feteiha, S. V. Elshocht, and A. Delabie, "Al₂O₃/InGaAs metal-oxide-semiconductor interface properties: Impact of Gd₂O₃ and Sc₂O₃ interfacial layers by atomic layer deposition," *ECS J. Solid State Sci. Technol.*, vol. 3, p. N133, Jan. 2014.

Bibliography

- [73] T. Aoki, N. Fukuhara, T. Osada, H. Sazawa, M. Hata, and T. Inoue, "High-performance GaAs-based metal-oxide-semiconductor heterostructure field-effect transistors with atomic-layer-deposited Al_2O_3 gate oxide and in situ AlN passivation by metalorganic chemical vapor deposition," *Appl. Phys. Express*, vol. 7, p. 106502, Oct. 2014.
- [74] H. D. Lee, T. Feng, L. Yu, D. Mastrogiovanni, A. Wan, T. Gustafsson, and E. Garfunkel, "Reduction of native oxides on GaAs during atomic layer growth of Al_2O_3 ," *Appl. Phys. Lett.*, vol. 94, no. 22, p. 222108, 2009.
- [75] D. Shahrjerdi, D. I. Garcia-Gutierrez, E. Tutuc, and S. K. Banerjee, "Chemical and physical interface studies of the atomic-layer-deposited Al_2O_3 on GaAs substrates," *Appl. Phys. Lett.*, vol. 92, p. 223501, June 2008.
- [76] G. Brammertz, H. Lin, K. Martens, A.-R. Alian, C. Merckling, J. Penaud, D. Kohen, W.-E. Wang, S. Sioncke, A. Delabie, M. Meuris, M. R. Caymax, and M. Heyns, "Electrical properties of III-V/Oxide interfaces," *ECS Trans.*, vol. 19, p. 375, 2009.
- [77] M. Caymax, G. Brammertz, A. Delabie, S. Sioncke, D. Lin, M. Scarrozza, G. Pourtois, W.-E. Wang, M. Meuris, and M. Heyns, "Interfaces of high-k dielectrics on GaAs: their common features and the relationship with Fermi level pinning (invited paper)," *Microelectron. Eng.*, vol. 86, p. 1529, July 2009.
- [78] J. F. Binder, P. Broqvist, and A. Pasquarello, "Electron trapping in substoichiometric germanium oxide," *Appl. Phys. Lett.*, vol. 97, no. 9, p. 092903, 2010.
- [79] Y. Oka, T. Takahashi, K. Okada, and S.-I. Iwai, "Structural analysis of anodic alumina films," *J. Non-Cryst. Solids*, vol. 30, p. 349, Jan. 1979.
- [80] P. Lamparter and R. Kniep, "Structure of amorphous Al_2O_3 ," *Physica B*, vol. 234–236, p. 405, June 1997.
- [81] S.-M. Lee, D. G. Cahill, and T. H. Allen, "Thermal conductivity of sputtered oxide films," *Phys. Rev. B*, vol. 52, p. 253, July 1995.
- [82] D. Norman, S. Brennan, R. Jaeger, and J. Stöhr, "Structural models for the interaction of oxygen with Al(111) and Al implied by photoemission and surface EXAFS," *Surf. Sci.*, vol. 105, p. L297, Apr. 1981.
- [83] S. Miyazaki, "Photoemission study of energy-band alignments and gap-state density distributions for high-k gate dielectrics," *J. Vac. Sci. Technol. B*, vol. 19, p. 2212, Nov. 2001.
- [84] H. Y. Yu, M. F. Li, B. J. Cho, C. C. Yeo, M. S. Joo, D.-L. Kwong, J. S. Pan, C. H. Ang, J. Z. Zheng, and S. Ramanathan, "Energy gap and band alignment for $(\text{HfO}_2)_x(\text{Al}_2\text{O}_3)_{1-x}$ on (100) Si," *Appl. Phys. Lett.*, vol. 81, p. 376, July 2002.
- [85] K. Y. Gao, T. Seyller, L. Ley, F. Ciobanu, G. Pensl, A. Tadich, J. D. Riley, and R. G. C. Leckey, " Al_2O_3 prepared by atomic layer deposition as gate dielectric on 6H-SiC(0001)," *Appl. Phys. Lett.*, vol. 83, p. 1830, Sept. 2003.

-
- [86] M. L. Huang, Y. C. Chang, C. H. Chang, T. D. Lin, J. Kwo, T. B. Wu, and M. Hong, "Energy-band parameters of atomic-layer-deposition $\text{Al}_2\text{O}_3/\text{InGaAs}$ heterostructure," *Appl. Phys. Lett.*, vol. 89, p. 012903, July 2006.
 - [87] N. V. Nguyen, O. A. Kirillov, W. Jiang, W. Wang, J. S. Suehle, P. D. Ye, Y. Xuan, N. Goel, K.-W. Choi, W. Tsai, and S. Sayan, "Band offsets of atomic-layer-deposited Al_2O_3 on GaAs and the effects of surface treatment," *Appl. Phys. Lett.*, vol. 93, p. 082105, Aug. 2008.
 - [88] V. V. Afanas'ev, A. Stesmans, G. Brammertz, A. Delabie, S. Sionke, A. O'Mahony, I. M. Povey, M. E. Pemble, E. O'Connor, P. K. Hurley, and S. B. Newcomb, "Energy barriers at interfaces between (100) $\text{In}_x\text{Ga}_{1-x}\text{As}$ ($0 < x < 0.53$) and atomic-layer deposited Al_2O_3 and HfO_2 ," *Appl. Phys. Lett.*, vol. 94, p. 202110, May 2009.
 - [89] J. Ahn, I. Geppert, M. Gunji, M. Holland, I. Thayne, M. Eizenberg, and P. C. McIntyre, "Titania/alumina bilayer gate insulators for InGaAs metal-oxide-semiconductor devices," *Appl. Phys. Lett.*, vol. 99, p. 232902, Dec. 2011.
 - [90] I. Krylov, D. Ritter, and M. Eizenberg, "The physical origin of dispersion in accumulation in InGaAs based metal oxide semiconductor gate stacks," *J. Appl. Phys.*, vol. 117, p. 174501, May 2015.
 - [91] J. R. Weber, A. Janotti, and C. G. Van de Walle, "Native defects in Al_2O_3 and their impact on III-V/ Al_2O_3 metal-oxide-semiconductor-based devices," *J. Appl. Phys.*, vol. 109, p. 033715, Feb. 2011.
 - [92] L. Lin, J. Robertson, and S. J. Clark, "Shifting Schottky barrier heights with ultra-thin dielectric layers," *Microelectron. Eng.*, vol. 88, p. 1461, July 2011.
 - [93] M. Xu, K. Xu, R. Contreras, M. Milojevic, T. Shen, O. Koybasi, Y. Wu, R. Wallace, and P. Ye, "New insight into Fermi-level unpinning on GaAs: Impact of different surface orientations," in *Electron Devices Meeting (IEDM), 2009 IEEE International*, p. 1, Dec. 2009.
 - [94] C. L. Hinkle, A. M. Sonnet, E. M. Vogel, S. McDonnell, G. J. Hughes, M. Milojevic, B. Lee, F. S. Aguirre-Tostado, K. J. Choi, J. Kim, and R. M. Wallace, "Frequency dispersion reduction and bond conversion on n-type GaAs by in situ surface oxide removal and passivation," *Appl. Phys. Lett.*, vol. 91, p. 163512, Oct. 2007.
 - [95] J. P. d. Souza, E. Kiewra, Y. Sun, A. Callegari, D. K. Sadana, G. Shahidi, D. J. Webb, J. Fompeyrine, R. Germann, C. Rossel, and C. Marchiori, "Inversion mode n-channel GaAs field effect transistor with high-k/metal gate," *Appl. Phys. Lett.*, vol. 92, p. 153508, Apr. 2008.
 - [96] C. L. Hinkle, A. M. Sonnet, E. M. Vogel, S. McDonnell, G. J. Hughes, M. Milojevic, B. Lee, F. S. Aguirre-Tostado, K. J. Choi, H. C. Kim, J. Kim, and R. M. Wallace, "GaAs interfacial self-cleaning by atomic layer deposition," *Appl. Phys. Lett.*, vol. 92, p. 071901, Feb. 2008.
 - [97] C. L. Hinkle, M. Milojevic, B. Brennan, A. M. Sonnet, F. S. Aguirre-Tostado, G. J. Hughes, E. M. Vogel, and R. M. Wallace, "Detection of Ga suboxides and their impact on III-V passivation and Fermi-level pinning," *Appl. Phys. Lett.*, vol. 94, p. 162101, Apr. 2009.

Bibliography

- [98] R. M. Wallace, P. C. McIntyre, J. Kim, and Y. Nishi, "Atomic Layer Deposition of Dielectrics on Ge and III–V Materials for Ultrahigh Performance Transistors," *MRS Bull.*, vol. 34, p. 493, July 2009.
- [99] E. O'Connor, S. Monaghan, R. D. Long, A. O'Mahony, I. M. Povey, K. Cherkaoui, M. E. Pemble, G. Brammertz, M. Heyns, S. B. Newcomb, V. V. Afanas'ev, and P. K. Hurley, "Temperature and frequency dependent electrical characterization of $\text{HfO}_2/\text{In}_x\text{Ga}_{1-x}\text{As}$ interfaces using capacitance-voltage and conductance methods," *Appl. Phys. Lett.*, vol. 94, p. 102902, Mar. 2009.
- [100] Y. C. Chang, C. Merckling, J. Penaud, C. Y. Lu, W.-E. Wang, J. Dekoster, M. Meuris, M. Caymax, M. Heyns, J. Kwo, and M. Hong, "Effective reduction of interfacial traps in $\text{Al}_2\text{O}_3/\text{GaAs}$ (001) gate stacks using surface engineering and thermal annealing," *Appl. Phys. Lett.*, vol. 97, p. 112901, Sept. 2010.
- [101] C. Hinkle, E. Vogel, P. Ye, and R. Wallace, "Interfacial chemistry of oxides on $\text{In}_x\text{Ga}_{(1-x)}\text{As}$ and implications for MOSFET applications," *Curr. Opin. Solid St. M.*, vol. 15, p. 188, Oct. 2011.
- [102] W. Cabrera, B. Brennan, H. Dong, T. P. O'Regan, I. M. Povey, S. Monaghan, E. O'Connor, P. K. Hurley, R. M. Wallace, and Y. J. Chabal, "Diffusion of $\text{In}_{0.53}\text{Ga}_{0.47}\text{As}$ elements through hafnium oxide during post deposition annealing," *Appl. Phys. Lett.*, vol. 104, p. 011601, Jan. 2014.
- [103] G. Brammertz, H.-C. Lin, K. Martens, D. Mercier, S. Sioncke, A. Delabie, W. E. Wang, M. Caymax, M. Meuris, and M. Heyns, "Capacitance-voltage characterization of $\text{GaAs-Al}_2\text{O}_3$ interfaces," *Appl. Phys. Lett.*, vol. 93, p. 183504, Nov. 2008.
- [104] Y. C. Chang, W. H. Chang, C. Merckling, J. Kwo, and M. Hong, "Inversion-channel $\text{GaAs}(100)$ metal-oxide-semiconductor field-effect-transistors using molecular beam deposited Al_2O_3 as a gate dielectric on different reconstructed surfaces," *Appl. Phys. Lett.*, vol. 102, p. 093506, Mar. 2013.
- [105] W. Wang, C. Gong, B. Shan, R. M. Wallace, and K. Cho, "Sulfur passivation effect on HfO_2/GaAs interface: A first-principles study," *Appl. Phys. Lett.*, vol. 98, p. 232113, June 2011.
- [106] A. Stesmans, S. Nguyen, and V. V. Afanas'ev, " As_{ga}^+ antisites identified by electron spin resonance as a main interface defect system in thermal $\text{GaAs}/\text{native oxide}$ structures," *Appl. Phys. Lett.*, vol. 103, p. 162111, Oct. 2013.
- [107] M. J. Hale, S. I. Yi, J. Z. Sexton, A. C. Kummel, and M. Passlack, "Erratum: Scanning tunneling microscopy and spectroscopy of gallium oxide deposition and oxidation on $\text{GaAs}(001)\text{-c}(2\times 8)/(2\times 4)$ [j. chem. phys. 119, 6719 (2003)]," *J Chem. Phys.*, vol. 127, no. 4, p. 049902, 2007.
- [108] J. Robertson, "Model of interface states at III-V oxide interfaces," *Appl. Phys. Lett.*, vol. 94, p. 152104, Apr. 2009.
- [109] H.-P. Komsa and A. Pasquarello, "Dangling bond charge transition levels in AlAs , GaAs , and InAs ," *Applied Physics Letters*, vol. 97, p. 191901, Nov. 2010.

-
- [110] W. Wang, K. Xiong, R. M. Wallace, and K. Cho, "First-principles study of initial growth of Ga_xO layer on GaAs- β 2(2 \times 4) surface and interface passivation by F," *J. Appl. Phys.*, vol. 110, p. 103714, Nov. 2011.
- [111] J. Robertson and L. Lin, "Bonding principles of passivation mechanism at III-V-oxide interfaces," *Appl. Phys. Lett.*, vol. 99, p. 222906, Nov. 2011.
- [112] J. Robertson and L. Lin, "Bonding principles of passivation mechanism at III-V-oxide interfaces," *Appl. Phys. Lett.*, vol. 99, p. 222906, Nov. 2011.
- [113] G. Miceli and A. Pasquarello, "Accurate determination of charge transition levels of the As-As dimer defect at GaAs/oxide interfaces through hybrid functionals," *Appl. Phys. Lett.*, vol. 103, p. 041602, July 2013.
- [114] Y. Guo, L. Lin, and J. Robertson, "Nitrogen passivation at GaAs:Al₂O₃ interfaces," *Appl. Phys. Lett.*, vol. 102, p. 091606, Mar. 2013.
- [115] G. Miceli and A. Pasquarello, "Defect levels at GaAs/Al₂O₃ interfaces: As-As dimer vs. Ga dangling bond," *Appl. Surf. Sci.*, vol. 291, p. 16, Feb. 2014.
- [116] J. Robertson, Y. Guo, and L. Lin, "Defect state passivation at III-V oxide interfaces for complementary metal-oxide-semiconductor devices," *J. Appl. Phys.*, vol. 117, p. 112806, Mar. 2015.
- [117] H.-P. Komsa and A. Pasquarello, "Identification of defect levels at as/oxide interfaces through hybrid functionals," *Microelectron. Eng.*, vol. 88, p. 1436, July 2011.
- [118] G. Miceli and A. Pasquarello, "First principles study of As 2p core-level shifts at GaAs/Al₂O₃ interfaces," *Appl. Phys. Lett.*, vol. 102, p. 201607, May 2013.
- [119] V. Djara, T. P. O'Regan, K. Cherkaoui, M. Schmidt, S. Monaghan, E. O'Connor, I. M. Povey, D. O'Connell, M. E. Pemble, and P. K. Hurley, "Electrically active interface defects in the In_{0.53}Ga_{0.47}As MOS system," *Microelectron. Eng.*, vol. 109, p. 182, Sept. 2013.
- [120] E. O'Connor, S. Monaghan, K. Cherkaoui, I. M. Povey, and P. K. Hurley, "Analysis of the minority carrier response of n-type and p-type Au/Ni/Al₂O₃/In_{0.53}Ga_{0.47}As/InP capacitors following an optimized (NH₄)₂S treatment," *Appl. Phys. Lett.*, vol. 99, p. 212901, Nov. 2011.
- [121] I. Thayne, R. Hill, M. Holland, X. Li, H. Zhou, D. Macintyre, S. Thoms, K. Kalna, C. Stanley, A. Asenov, R. Droopad, and M. Passlack, "Review of current status of III-V MOSFETs," *ECS Trans.*, vol. 19, p. 275, May 2009.
- [122] G. Brammertz, H.-C. Lin, M. Caymax, M. Meuris, M. Heyns, and M. Passlack, "On the interface state density at In_{0.53}Ga_{0.47}As/oxide interfaces," *Appl. Phys. Lett.*, vol. 95, p. 202109, Nov. 2009.
- [123] H.-P. Komsa and A. Pasquarello, "Comparison of vacancy and antisite defects in GaAs and InGaAs through hybrid functionals," *J. Phys.: Condens. Matter*, vol. 24, p. 045801, Feb. 2012.

Bibliography

- [124] L. Lin and J. Robertson, "Defect states at III-V semiconductor oxide interfaces," *Appl. Phys. Lett.*, vol. 98, p. 082903, Feb. 2011.
- [125] V. N. Brudnyi, S. N. Grinyaev, and N. G. Kolin, "The Fermi Level Pinning in Semiconductors (Interphase Boundaries, Clusters, and Radiation Modification)," *Russ. Phys. J.*, vol. 46, p. 594, June 2003.
- [126] T. R. Paudel, A. Zakutayev, S. Lany, M. d'Avezac, and A. Zunger, "Doping rules and doping prototypes in A_2BO_4 spinel oxides," *Adv. Func. Mater.*, vol. 21, no. 23, p. 4493, 2011.
- [127] W. Walukiewicz, "Mechanism of schottky barrier formation: The role of amphoteric native defects," *J. Vac. Sci. Technol. B*, vol. 5, no. 4, p. 1062, 1987.
- [128] W. Walukiewicz, "Mechanism of Fermi-level stabilization in semiconductors," *Phys. Rev. B*, vol. 37, p. 4760, Mar. 1988.
- [129] G. A. Baraff and M. Schlüter, "Electronic structure, total energies, and abundances of the elementary point defects in GaAs," *Phys. Rev. Lett.*, vol. 55, no. 12, p. 1327, 1985.
- [130] G. A. Baraff and M. Schlüter, "Binding and formation energies of native defect pairs in GaAs," *Phys. Rev. B*, vol. 33, no. 10, p. 7346, 1986.
- [131] P. A. Schultz and O. A. von Lilienfeld, "Simple intrinsic defects in gallium arsenide," *Model. Simul. Mater. Sci. Eng.*, vol. 17, p. 084007, Dec. 2009.
- [132] A. Zangwill, *Physics at Surfaces*. Cambridge: Cambridge University Press, 1988.
- [133] W. H. Schottky *Physik Zeits.*, no. 41, p. 570, 1940.
- [134] J. Bardeen, "Surface states and rectification at a metal semi-conductor contact," *Phys. Rev.*, vol. 71, p. 717, May 1947.
- [135] V. Heine, "Theory of surface states," *Phys. Rev.*, vol. 138, p. A1689, Jun 1965.
- [136] J. Tersoff, "Theory of semiconductor heterojunctions: The role of quantum dipoles," *Phys. Rev. B*, vol. 30, p. 4874, Oct 1984.
- [137] J. Robertson, "Band offsets, schottky barrier heights, and their effects on electronic devices," *J. Vac. Sci. Technol. A*, vol. 31, no. 5, p. 050821, 2013.
- [138] P. Hohenberg and W. Kohn, "Inhomogeneous electron gas," *Phys. Rev.*, vol. 136, p. B864, Nov 1964.
- [139] W. Kohn and L. J. Sham, "Self-consistent equations including exchange and correlation effects," *Phys. Rev.*, vol. 140, p. A1133, Nov 1965.
- [140] J. P. Perdew, K. Burke, and M. Ernzerhof, "Generalized gradient approximation made simple," *Phys. Rev. Lett.*, vol. 77, p. 3865, Oct. 1996.
- [141] C. G. Van de Walle and J. Neugebauer, "First-principles calculations for defects and impurities: Applications to III-nitrides," *J. Appl. Phys.*, vol. 95, p. 3851, Apr. 2004.

-
- [142] C. G. Van de Walle and A. Janotti, "Advances in electronic structure methods for defects and impurities in solids," *Phys. Stat. Sol. B*, vol. 248, no. 1, p. 19, 2011.
- [143] P. Mori-Sánchez, A. J. Cohen, and W. Yang, "Localization and delocalization errors in density functional theory and implications for band-gap prediction," *Phys. Rev. Lett.*, vol. 100, p. 146401, Apr 2008.
- [144] T. M. Henderson, J. Paier, and G. E. Scuseria, "Accurate treatment of solids with the HSE screened hybrid," *Phys. Stat. Sol. B*, vol. 248, no. 4, p. 767, 2011.
- [145] A. D. Becke, "A new mixing of Hartree-Fock and local density-functional theories," *J. Chem. Phys.*, vol. 98, p. 1372, Jan. 1993.
- [146] J. P. Perdew, M. Ernzerhof, and K. Burke, "Rationale for mixing exact exchange with density functional approximations," *J. Chem. Phys.*, vol. 105, p. 9982, Dec. 1996.
- [147] J. Heyd, G. E. Scuseria, and M. Ernzerhof, "Hybrid functionals based on a screened coulomb potential," *J. Chem. Phys.*, vol. 118, p. 8207, May 2003.
- [148] J. Heyd, G. E. Scuseria, and M. Ernzerhof, "Erratum: "Hybrid functionals based on a screened coulomb potential" [*J. Chem. Phys.* **118**, 8207 (2003)]," *J. Chem. Phys.*, vol. 124, p. 219906, June 2006.
- [149] A. Alkauskas, P. Broqvist, and A. Pasquarello, "Defect levels through hybrid density functionals: Insights and applications," *Phys. Status Solidi B*, vol. 248, p. 775, 2011.
- [150] A. Alkauskas, P. Broqvist, and A. Pasquarello, "Defect energy levels in density functional calculations: Alignment and band gap problem," *Phys. Rev. Lett.*, vol. 101, p. 046405, July 2008.
- [151] A. Alkauskas and A. Pasquarello, "Band-edge problem in the theoretical determination of defect energy levels: The O vacancy in ZnO as a benchmark case," *Phys. Rev. B*, vol. 84, p. 125206, 2011.
- [152] H.-P. Komsa, T. T. Rantala, and A. Pasquarello, "Finite-size supercell correction schemes for charged defect calculations," *Phys. Rev. B*, vol. 86, p. 045112, July 2012.
- [153] M. M. Richard, *Electronic Structure basic Theory and Practical Methods*. Cambridge University Press, 2004.
- [154] P. Giannozzi, S. Baroni, N. Bonini, M. Calandra, R. Car, C. Cavazzoni, D. Ceresoli, G. L. Chiarotti, M. Cococcioni, I. Dabo, A. Dal Corso, S. de Gironcoli, S. Fabris, G. Fratesi, R. Gebauer, U. Gerstmann, C. Gougoussis, A. Kokalj, M. Lazzeri, L. Martin-Samos, N. Marzari, F. Mauri, R. Mazzarello, S. Paolini, A. Pasquarello, L. Paulatto, C. Sbraccia, S. Scandolo, G. Sciauzero, A. P. Seitsonen, A. Smogunov, P. Umari, and R. M. Wentzcovitch, "QUANTUM ESPRESSO: a modular and open-source software project for quantum simulations of materials," *J. Phys: Condens. Matter*, vol. 21, p. 395502, Sept. 2009.
- [155] H. J. C. Berendsen, J. P. M. Postma, W. F. van Gunsteren, A. DiNola, and J. R. Haak, "Molecular dynamics with coupling to an external bath," *J. Chem. Phys.*, vol. 81, no. 8, p. 3684, 1984.

Bibliography

- [156] H. Jónsson, G. Mills, and K. W. Jacobsen, *Classical and Quantum Dynamics in Condensed Phase Systems*. World Scientific, Singapore, 1998.
- [157] G. Henkelman, B. P. Uberuaga, and H. Jónsson, “A climbing image nudged elastic band method for finding saddle points and minimum energy paths,” *J. Chem. Phys.*, vol. 113, p. 9901, Dec. 2000.
- [158] H.-P. Komsa, P. Broqvist, and A. Pasquarello, “Alignment of defect levels and band edges through hybrid functionals: Effect of screening in the exchange term,” *Phys. Rev. B*, vol. 81, p. 205118, 2010.
- [159] P. Broqvist, A. Alkauskas, and A. Pasquarello, “Hybrid-functional calculations with plane-wave basis sets: Effect of singularity correction on total energies, energy eigenvalues, and defect energy levels,” *Phys. Rev. B*, vol. 80, p. 085114, Aug. 2009.
- [160] H.-P. Komsa and A. Pasquarello, “Assessing the accuracy of hybrid functionals in the determination of defect levels: Application to the As antisite in GaAs,” *Phys. Rev. B*, vol. 84, p. 075207, 2011.
- [161] P. Broqvist, J. F. Binder, and A. Pasquarello, “Band offsets at the Ge/GeO₂ interface through hybrid density functionals,” *Appl. Phys. Lett.*, vol. 94, p. 141911, Apr. 2009.
- [162] M. A. L. Marques, J. Vidal, M. J. T. Oliveira, L. Reining, and S. Botti, “Density-based mixing parameter for hybrid functionals,” *Phys. Rev. B*, vol. 83, p. 035119, Jan 2011.
- [163] G. Pacchioni, F. Frigoli, D. Ricci, and J. A. Weil, “Theoretical description of hole localization in a quartz α center: The importance of exact electron exchange,” *Phys. Rev. B*, vol. 63, p. 054102, Dec 2000.
- [164] J. Lægsgaard and K. Stokbro, “Hole trapping at α impurities in silica: A challenge for density functional theories,” *Phys. Rev. Lett.*, vol. 86, p. 2834, Mar 2001.
- [165] A. Carvalho, A. Alkauskas, A. Pasquarello, A. K. Tagantsev, and N. Setter, “A hybrid density functional study of lithium in ZnO: Stability, ionization levels, and diffusion,” *Phys. Rev. B*, vol. 80, p. 195205, Nov 2009.
- [166] J. L. Lyons, A. Janotti, and C. G. Van de Walle, “Shallow versus deep nature of Mg acceptors in nitride semiconductors,” *Phys. Rev. Lett.*, vol. 108, p. 156403, Apr 2012.
- [167] P. Rudolph and M. Jurisch, “Bulk growth of GaAs an overview,” *J. Cryst. Growth*, vol. 198, p. 325, Mar. 1999.
- [168] M. Jurisch, F. Börner, T. Biünger, S. Eichler, T. Flade, U. Kretzer, A. Kiöhler, J. Stenzenberger, and B. Weinert, “LEC- and VGF-growth of SI GaAs single crystals—recent developments and current issues,” *J. Cryst. Growth*, vol. 275, p. 283, Feb. 2005.
- [169] S. Geller, “Crystal Structure of β -Ga₂O₃,” *J. Chem. Phys.*, vol. 33, p. 676, Sept. 1960.
- [170] C. Freysoldt, J. Neugebauer, and C. G. Van de Walle, “Fully ab initio finite-size corrections for charged-defect supercell calculations,” *Phys. Rev. Lett.*, vol. 102, p. 016402, Jan. 2009.

-
- [171] H.-P. Komsa and A. Pasquarello, "Finite-size supercell correction for charged defects at surfaces and interfaces," *Phys. Rev. Lett.*, vol. 110, p. 095505, Feb 2013.
- [172] D. Colleoni and A. Pasquarello, "Amphoteric defects in GaAs leading to Fermi-level pinning: A hybrid functional study," *Microelectron. Eng.*, vol. 109, p. 50, Sept. 2013.
- [173] J. Neugebauer and C. G. Van de Walle, "Theory of point defects and complexes in GaN," *Mat. Res. Soc. Symp. Proc.*, vol. 395, p. 645, 1996.
- [174] S. Lany and A. Zunger, "Assessment of correction methods for the band-gap problem and for finite-size effects in supercell defect calculations: Case studies for ZnO and GaAs," *Phys. Rev. B*, vol. 78, p. 235104, Dec 2008.
- [175] H.-P. Komsa, T. Rantala, and A. Pasquarello, "Comparison between various finite-size supercell correction schemes for charged defect calculations," *Physica B*, vol. 407, p. 3063, Aug. 2012.
- [176] M. Kaminska, E. R. Weber, Z. Liliental-Weber, R. Leon, and U. Rek, "Stoichiometry-related defects in GaAs grown by molecular-beam epitaxy at low temperatures," *J. Vac. Sci. Technol. B*, vol. 7, p. 710, July 1989.
- [177] X. Liu, A. Prasad, W. M. Chen, A. Kurpiewski, A. Stoschek, Z. Liliental-Weber, and E. R. Weber, "Mechanism responsible for the semi-insulating properties of low-temperature-grown GaAs," *Appl. Phys. Lett.*, vol. 65, no. 23, p. 3002, 1994.
- [178] K. Krambrock, M. Linde, J. M. Spaeth, D. C. Look, D. Bliss, and W. Walukiewicz, "Arsenic antisite-related defects in low-temperature MBE grown GaAs," *Semicond. Sci. Tech.*, vol. 7, p. 1037, Aug. 1992.
- [179] D. Colleoni and A. Pasquarello, "The O_{As} defect in GaAs: A hybrid density functional study," *Appl. Surf. Sci.*, vol. 291, p. 6, 2014.
- [180] D. Colleoni and A. Pasquarello, "Assignment of fermi-level pinning and optical transitions to the $(As_{Ga})_2-O_{As}$ center in oxygen-doped GaAs," *Appl. Phys. Lett.*, vol. 103, no. 14, p. 142108, 2013.
- [181] S. Adachi, "GaAs, AlAs, and $Al_xGa_{1-x}As$: Material parameters for use in research and device applications," *J. Appl. Phys.*, vol. 58, p. R1, Aug. 1985.
- [182] J. Coutinho, R. Jones, P. R. Briddon, and S. Öberg, "Oxygen and dioxygen centers in Si and Ge: Density-functional calculations," *Phys. Rev. B*, vol. 62, p. 10824, Oct. 2000.
- [183] J. F. Binder and A. Pasquarello, "Minimum energy path and atomistic mechanism of the elementary step in oxygen diffusion in silicon: A density-functional study," *Phys. Rev. B*, vol. 89, p. 245306, June 2014.
- [184] N. Marzari, A. A. Mostofi, J. R. Yates, I. Souza, and D. Vanderbilt, "Maximally localized wannier functions: Theory and applications," *Rev. Mod. Phys.*, vol. 84, p. 1419, Oct. 2012.
- [185] D. Colleoni, G. Miceli, and A. Pasquarello, "Origin of fermi-level pinning at GaAs surfaces and interfaces," *J. Phys.: Condens. Matter*, vol. 26, p. 492202, Dec. 2014.

Bibliography

- [186] G. Hollinger, R. Skheyta-Kabbani, and M. Gendry, "Oxides on GaAs and InAs surfaces: An x-ray-photoelectron-spectroscopy study of reference compounds and thin oxide layers," *Phys. Rev. B*, vol. 49, p. 11159, Apr. 1994.
- [187] A. J. Bard, R. Parsons, and J. Jordan, *Standard Potentials in Aqueous Solution*. CRC Press, Aug. 1985.
- [188] J. A. Stroscio, R. M. Feenstra, and A. P. Fein, "Structure of oxygen adsorbed on the GaAs(110) surface studied using scanning tunneling microscopy," *Phys. Rev. B*, vol. 36, no. 14, p. 7718, 1987.
- [189] W. Wang, C. Hinkle, E. Vogel, K. Cho, and R. Wallace, "Is interfacial chemistry correlated to gap states for high-k/III–V interfaces?," *Microelectron. Eng.*, vol. 88, p. 1061, July 2011.
- [190] M. M. Frank, G. D. Wilk, D. Starodub, T. Gustafsson, E. Garfunkel, Y. J. Chabal, J. Grazul, and D. A. Muller, "HfO₂ and Al₂O₃ gate dielectrics on GaAs grown by atomic layer deposition," *Appl. Phys. Lett.*, vol. 86, p. 152904, Apr. 2005.
- [191] P. Broqvist and A. Pasquarello, "First principles investigation of defects at interfaces between silicon and amorphous high- κ oxides," *Microelectron. Eng.*, vol. 84, p. 2022, Sept. 2007.
- [192] M. Marezio and J. P. Remeika, "Bond Lengths in the α -Ga₂O₃ Structure and the High-Pressure Phase of Ga_{2-x}Fe_xO₃," *J. Chem. Phys.*, vol. 46, p. 1862, Mar. 1967.
- [193] O. E. Tereshchenko, A. V. Bakulin, S. E. Kulkova, and S. V. Eremeev, "Backward Reconstructions on GaAs(001) Surface Induced by Atomic Hydrogen Reactions: Surfactant-Assisted Low-Temperature Surface Ordering," *J. Phys. Chem. C*, vol. 117, p. 9723, May 2013.
- [194] J. J. Kolodziej, M. Goryl, J. Konior, M. Reichling, and M. Szymonski, "Direct real-space imaging of the $c(2\times 8)/(2\times 4)$ GaAs (001) surface structure," *Phys. Rev. B*, vol. 76, p. 245314, Dec. 2007.
- [195] P. Dahinden, P. Broqvist, and A. Pasquarello, "Charge transition levels of nitrogen dangling bonds at Si/SiO₂ interfaces: A first-principles study," *Phys. Rev. B*, vol. 81, p. 085331, Feb. 2010.
- [196] J. F. Binder, P. Broqvist, and A. Pasquarello, "Electron density of states at Ge/oxide interfaces due to formation," *Microelectron. Eng.*, vol. 88, p. 391, Apr. 2011.
- [197] J. R. Weber, A. Janotti, and C. G. Van de Walle, "Native defects in Al₂O₃ and their impact on III-V/Al₂O₃ metal-oxide-semiconductor-based devices," *J. Appl. Phys.*, vol. 109, p. 033715, Feb. 2011.
- [198] C. G. Van de Walle and R. M. Martin, "Theoretical calculations of heterojunction discontinuities in the Si/Ge system," *Phys. Rev. B*, vol. 34, p. 5621, Oct. 1986.
- [199] A. Baldereschi, S. Baroni, and R. Resta, "Band Offsets in Lattice-Matched Heterojunctions: A Model and First-Principles Calculations for GaAs/AlAs," *Phys. Rev. Lett.*, vol. 61, p. 734, Aug. 1988.

-
- [200] B. Willis and J. Carlile, C, *Experimental Neutron Scattering*. Oxford University Press, 2009.
- [201] G. I. Csonka, J. P. Perdew, A. Ruzsinszky, P. H. T. Philipsen, S. Lebègue, J. Paier, O. A. Vydrov, and J. G. Ángyán, “Assessing the performance of recent density functionals for bulk solids,” *Phys. Rev. B*, vol. 79, p. 155107, Apr. 2009.
- [202] G. Gutiérrez and B. Johansson, “Molecular dynamics study of structural properties of amorphous Al_2O_3 ,” *Phys. Rev. B*, vol. 65, p. 104202, Feb. 2002.
- [203] R. Manaila, A. Dévényi, and E. Candet, “Structural order in amorphous aluminas,” *Thin Solid Films*, vol. 116, p. 289, June 1984.
- [204] J. Lewis, D. Schwarzenbach, and H. D. Flack, “Electric field gradients and charge density in corundum, $\alpha\text{-Al}_2\text{O}_3$,” *Acta Crystallogr. Sect. A*, vol. 38, p. 733, Sept. 1982.
- [205] B. Ollivier, R. Retoux, P. Lacorre, D. Massiot, and G. Férey, “Crystal structure of κ -alumina: an X-ray powder diffraction, TEM and NMR study,” *J. Mater. Chem.*, vol. 7, p. 1049, Jan. 1997.
- [206] R. H. French, “Electronic Band Structure of Al_2O_3 , with Comparison to AlON and AlN ,” *J. Am. Ceram. Soc.*, vol. 73, no. 3, p. 477, 1990.
- [207] V. V. Afanas’ev, M. Houssa, A. Stesmans, C. Merckling, T. Schram, and J. A. Kittl, “Influence of Al_2O_3 crystallization on band offsets at interfaces with Si and TiN_x ,” *Appl. Phys. Lett.*, vol. 99, p. 072103, Aug. 2011.
- [208] S. Toyoda, T. Shinohara, H. Kumigashira, M. Oshima, and Y. Kato, “Significant increase in conduction band discontinuity due to solid phase epitaxy of Al_2O_3 gate insulator films on GaN semiconductor,” *Appl. Phys. Lett.*, vol. 101, p. 231607, Dec. 2012.
- [209] K. Shiraishi, “A New Slab Model Approach for Electronic Structure Calculation of Polar Semiconductor Surface,” *J. Phys. Soc. Jpn.*, vol. 59, p. 3455, Oct. 1990.
- [210] A. K. Harman, S. Ninomiya, and S. Adachi, “Optical constants of sapphire ($\alpha\text{-Al}_2\text{O}_3$) single crystals,” *J. Appl. Phys.*, vol. 76, p. 8032, Dec. 1994.
- [211] D. J. Chadi and K. J. Chang, “Metastability of the Isolated Arsenic-Antisite Defect in GaAs,” *Phys. Rev. Lett.*, vol. 60, p. 2187, May 1988.
- [212] E. Pehlke and M. Scheffler, “Evidence for site-sensitive screening of core holes at the Si and Ge (001) surface,” *Phys. Rev. Lett.*, vol. 71, p. 2338, Oct 1993.
- [213] H.-Y. Chou, V. V. Afanas’ev, M. Houssa, A. Stesmans, L. Dong, and P. D. Ye, “Electron band alignment at the interface of (100)InSb with atomic-layer deposited Al_2O_3 ,” *Appl. Phys. Lett.*, vol. 101, p. 082114, Aug. 2012.

List of Acronyms

CMOS	complementary meta-oxide-semiconductor
MOSFET	metal-oxide-semiconductor field-effect-transistor
VBM	valence band maximum
CBM	conduction band minumum
SI	semi-insulating
ESR	electron spin resonance
MCDA	magnetic circular dichroism absorption
ENDOR	electron-nuclear double-resonance
LVM	local vibrational mode
DB	dangling bond
RHEED	reflection high energy electron diffraction
LEED	low energy electron diffraction
STM	scanning tunneling microscopy
MBE	molecular beam epitaxy
ALD	atomic layer deposition
TMA	trimethylaluminum
XPS	x-ray photoemission spectroscopy
D_{it}	density of interfacial states
MIGS	metal-induced gap states
MD	molecular dynamics
NEB	nudged-elastic band
DFT	density functional theory

Chapter 7. List of Acronyms

XC exchange-correlation

LDA local density approximation

GGA generalized gradient approximation

PBE Perdew Burke Ernzerhof

HF Hartree-Fock

HSE Heyd Scuseria Ernzerhof

MEP minimum energy path

TS transition state

PA potential alignment

FNV Freysoldt Neugebauer Van de Walle

WF Wannier function

CN coordination number

VBO valence band offset

IPE internal photoemission

Acknowledgements

During these four years of doctoral studies I tried to show my gratitude to those who helped me throughout. In any case, this white page gives me the opportunity to thank them once more with a few insufficient words.

It might seem obvious that a student thanks his own thesis supervisor, but I truly want to thank Monsieur le Professeur Alfredo Pasquarello. Not only for the passion, the competence, the time, and the patience he dedicated to me and my work during these four years but also for the trust and the respect he demonstrated towards me. I feel lucky to have worked with him. I thank Doctor Giacomo Miceli for having helped me at work, for all the discussions about many different subjects and for having grown up with me.

During my stay at EPFL I met many friends with whom I enjoyed the sun and the snow, the joy and the sadness. Thanks to Gabriel, Gabriele, Chen, Hugo, Fernando, Gloria, Momchill, Naunidh, Diego, Joseph, Pier, Francesco, Eduardo, and Julia. Many thanks also to Noemi and Tanya for their help and their support. I also want to thank Francesco, Flavia, and Silvia for the smiles they always addressed me. All of you deserve a special thank but because of the little time I have, just accept my "Thank you!".

I thank my family for the support they gave me, and I hope this adventure gave them some gratification to repay them for the tears they cried the moment I started walking my way.

Finally, I thank Elisa. For having followed me, stayed with me, chosen me, and loved me every day.

Lausanne, 17 December 2015

Davide Colleoni

Davide Colleoni

PERSONAL INFORMATION

Birth date :	7 th of May 1987
Place of birth:	Merate, Italy
Nationality :	Italian

EDUCATION

PhD :	École Polytechnique Fédérale de Lausanne (EPFL) Doctoral School in Physics Supervisor: Prof. Alfredo Pasquarello	November 2015
MS:	University of Milano Bicocca, Material Science Graduated 110/110 Cum Laude Supervisor: Prof. Marco Bernasconi	October 2011
BS:	University of Milano Bicocca, Material Science Graduated 110/110 Cum Laude Supervisor: Prof. Marco Bernasconi	October 2009

List of Publications:

- S. Caravati, D. Colleoni, R. Mazzarello, T.D. Kühne, M. Krack, M. Bernasconi, M. Parrinello,
"First-principles study of nitrogen doping in cubic and amorphous $\text{Ge}_2\text{Sb}_2\text{Te}_5$ ",
J. Phys.: Condens. Matter **23**, 265801 (2011).
- D. Colleoni and A. Pasquarello,
"Amphoteric defects in GaAs leading to Fermi-level pinning: A hybrid functional study",
Microelectron. Eng. **109**, 50 (2013).
- D. Colleoni and A. Pasquarello,
"Assignment of Fermi-level pinning and optical transitions to the $(\text{As}_{\text{Ga}})_2\text{-O}_{\text{As}}$ center in
oxygen-doped GaAs",
Appl. Phys. Lett. **103**, 142108 (2013).
- D. Colleoni and A. Pasquarello,
"The O_{Ga} defect in GaAs: A hybrid density functional study",
Appl. Surf. Sci. **291**, 6 (2014).
- D. Colleoni, G. Miceli, and A. Pasquarello,
"Origin of Fermi-level pinning at GaAs surfaces and interfaces",
J. Phys.: Condens. Matter **26**, 492202 (2014).
- D. Colleoni, G. Miceli, and A. Pasquarello,
"Fermi-level pinning through defects at GaAs/oxide interfaces: A density functional study",
Phys. Rev. B **92**, 125304 (2015).
- D. Colleoni, G. Miceli, and A. Pasquarello,
"Arsenic related defect states resonant with the semiconductor conduction band at the
 $\text{In}_{0.53}\text{Ga}_{0.47}\text{As}$ /oxide interface: A density functional study",
Microelectron. Eng. **147**, 260 (2015).
- D. Colleoni and A. Pasquarello,
"Interfacial Ga-As suboxide: Structural and electronic properties",
Appl. Phys. Lett. **107**, 031605 (2015).
- D. Colleoni, G. Miceli, and A. Pasquarello,
"Band alignment and chemical bonding at the GaAs/ Al_2O_3 interface: A hybrid functional
study",
Appl. Phys. Lett. **107**, 211601 (2015).
- D. Colleoni and A. Pasquarello,
"Oxygen defects in GaAs: A hybrid functional study",
Submitted to *Phys. Rev. B*

